Mémoire

Auteur : Lallemand, Diego
Promoteur(s) : Martin, John
Faculté : Faculté des Sciences
Diplôme : Master en sciences physiques, à finalité approfondie
Année académique : 2024-2025
URI/URL : http://hdl.handle.net/2268.2/22980

Faculty of Science
Department of Physics

Noisy quantum metrology with spins

Diego LALLEMAND

Supervisor
Prof. John MARTIN

Reading Committee
Prof. Ngoc Duy NGUYEN
Prof. Peter SCHLAGHECK
Dr. Eric OPSOMER

In fulfilment of the requirements for
the degree of Master of Science in Physics

Academic Year 2024-2025

Acknowledgements

First, I would like to thank my thesis advisor, John Martin, for the time he spent giving me advice and ideas to improve this master's thesis. Second, I want to thank the evaluation committee, Ngoc Duy Nguyen, Peter Schlagheck and Eric Opsomer for the interest they gave in my master's thesis and the time they spent reading it. Third, I would like to thank Eduardo Serrano Ensástiga for his valuable advice and assistance with the calculations and derivations of the results, and with whom I had the opportunity to engage in interesting discussions.

Moreover, I would like to thank my near and dear, family and friends, for the endless support without which I would not have come so far. In particular, I wish to thank Thibault Wachtelaer, Liam Brennenraedts, and Sylvain Noël for the time we spent working together and for the enriching discussions we shared about our respective topics.

Contents

Introduction

The main goal of physics is to explain the laws of nature, which requires observations and therefore measurements of our environment. These observations will eventually lead to the validation or invalidation of theories. This statement reminds us how metrology, the branch of science dedicated to measurement, is at the core of physics. This is why physicists are interested in developing ever more precise measurement protocols. These improvements were at the heart of crucial discoveries such as the determination of the speed of light and the observation of its invariance between different observers [1], the detection of gravitational waves [2], measurement of the Lamb shift of the hydrogen atom [3] and the hyperfine splitting in light hydrogen-like atoms [4].

The development of quantum physics at the beginning of the twentieth century encouraged physicists to be even more precise with their measurements. The discovery of lasers in the 1960s marked a pivotal moment in the evolution of metrology and experimental physics. Lasers provided an unprecedented source of coherent light, revolutionising precision measurements across various fields, from spectroscopy to timekeeping. Their applications paved the way for technologies such as optical clocks and interferometers, drastically enhancing measurement accuracy [5]. Before lasers, advances in precision measurement were often tied to mechanical or electrical systems. The advent of radio-frequency atomic clocks in the mid-twentieth century, for example, was a significant breakthrough that set new standards in time measurement. These innovations created the foundation on which modern metrology is built. Later in the century, experimentalists made major technological developments and successfully created large coherent quantum systems while being able to manipulate individual quantum objects. Driven by these recent improvements, theoreticians of the late 20th century developed new theories to better understand the concept of measurement. This played an important role in the development of quantum information, of which quantum metrology is a part. This field of study has already proven its worth and has applications notably in gravitational wave detection [2, 6], quantum sensing [7, 8], timekeeping [9], quantum magnetometry [10], biomedical [11] and fundamental physics [12].

The aim of an experiment is to infer some values of an unknown parameter from an ensemble of statistical data. Since measurements are usually imperfect, the obtained value is not the true value, but is affected by a certain statistical error and systematic error. Systematic errors, which consistently bias measurement results in a reproducible manner (*e.g.*, due to miscalibrated instruments or environmental influences), are notoriously difficult to eliminate entirely. Given their persistent nature and the fact that they often require separate treatment or correction techniques, we do not consider them explicitly in this work. Instead, we focus on random and intrinsic sources of error. In experimental physics, measurement uncertainty can arise from several origins: instrumental errors, related to the finite precision, resolution, or stability of the measuring apparatus; procedural errors, resulting from imperfections in the experimental protocol or control over external variables; and most fundamentally, intrinsic physical uncertainties, which are inherent to the system being measured. In the context of

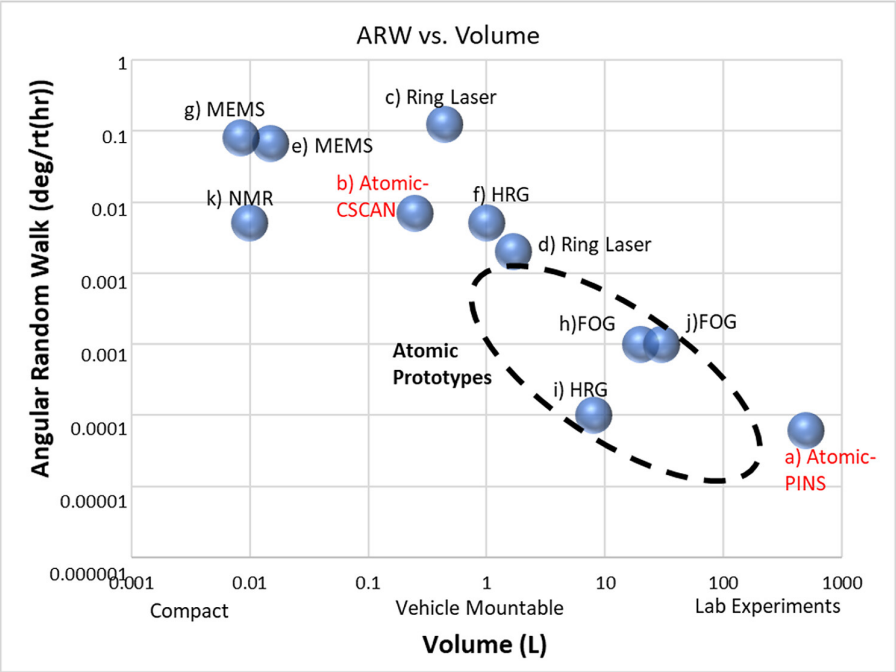

Figure 1: (Taken from Ref. [15]). Gyroscope precision vs system size. Detailed caption and references are provided in [15].

quantum mechanics, this last category plays a central role: due to the probabilistic structure of quantum theory and the constraints imposed by the uncertainty principle, certain measurement errors are fundamentally unavoidable and must be accounted for within the theoretical framework itself. However, we should not consider the fluctuation of the physical system as an error but as an indeterminacy. From this we can define two types of limit:

(i) The *Standard Quantum Limit* (SQL), also known as the shot-noise limit, is the fundamental limit that a classical measurement device can achieve.

(ii) The *Heisenberg Limit* (HL) is the ultimate precision bound achievable in a quantum measurement. Quantum metrology aims to reach this limit by exploiting quantum features, such as entanglement, in a system of N particles or photons.

In practical terms, the maximum achievable precision, corresponding to the Heisenberg limit, scales as $1/N$, surpassing the classical limit (the standard quantum limit), which scales as $1/\sqrt{N}$.

Nowadays, quantum metrology has numerous applications. For example, sub-shot noise[1] rotation measurements can lead to advances in high-precision sensing and monitoring of rotational vibrations [13]. Furthermore, when combined with rotational optomechanical systems [14], they enable the development of highly precise quantum gyroscopes. Figure 1 presents the precision of a gyroscope versus its size [15].

Here, we will present an example that demonstrates the importance of the discipline in detecting a small rotation about an *a priori* known axis. We consider a unitary rotation of a quantum state on the Bloch sphere around an axis $\mathbf{n}$ that is orthogonal to the mean spin direction $\mathbf{s}$ (see Fig. 2). Pezzè *et al.* showed that the phase sensitivity is [16]

$$\Delta\theta = \frac{\xi_{\mathrm{R}}}{\sqrt{\nu N}}, \tag{1}$$

[1] This means that the precision surpasses the SQL.

where the spin-squeezing parameter ξ_{R} is defined as

$$\xi_{\mathrm{R}}^2 = \frac{N(\Delta J_\perp)^2}{\langle J_{\mathbf{s}}\rangle^2}, \tag{2}$$

with $\perp$ denoting the direction orthogonal to both $\mathbf{s}$ and $\mathbf{n}$. This parameter, introduced by Wineland *et al.* [17, 18], quantifies spin squeezing in a metrological context. When $\xi_{\mathrm{R}}^2 < 1$, the state is said to be (metrologically) spin-squeezed along the $\perp$ direction. Such states can surpass the standard quantum limit, achieving $\Delta\theta < 1/\sqrt{\nu N}$, where ν is the number of time we repeat the experiment. This condition implies that the spin fluctuations orthogonal to the rotation axis must be smaller than the projection noise of uncorrelated atoms [16], *i.e.*,

$$(\Delta J_\perp)^2 < \frac{N}{4}, \tag{3}$$

and the spin component $\langle J_{\mathbf{s}}\rangle$ must be sufficiently large. Figure 2 shows the Husimi distribution and the spin probability distribution aligned with the y-axis for two states. Figure 2a shows a spin coherent state pointing in the x direction, and Fig. 2b shows a spin-squeezed state pointing in that same direction. In a parameter estimation protocol, where the parameter is the rotation angle, the key is to distinguish the initial state from the rotated one. It is easy to see that the squeezed state performs significantly better than the coherent state. One can distinguish the squeezed state before and after rotation for a much smaller angle compared to the coherent state. Later, we will quantify this difference using a figure of merit known as the **Quantum Fisher Information**. This quantity applies not only in the context of a rotation but in a much more general framework.

Experiments were conducted to demonstrate the feasibility and advantages of slightly different systems [19, 20]. Yang et al. successfully created a Schrödinger-cat state—a quantum superposition of opposite nuclear-spin projections ($m_z = 5/2$ and $m_z = -5/2$)—using spin-5/2 nuclei of ^{173}Yb trapped in an optical lattice, achieving a long coherence time of $1.4 \pm 1 \times 10^3$ s. The first step in the measurement protocol involves preparing either a Schrödinger-cat state, $|\psi_\pm\rangle = \frac{1}{\sqrt{2}}(|J, J\rangle + e^{i\phi}\,|J, -J\rangle)$, where $|J, m_z\rangle$ are the common eigenstates of J_z and $\mathbf{J}^2$ (with $J_z\,|J, m_z\rangle = m_z\,|J, m_z\rangle$ and $\mathbf{J}^2\,|J, m_z\rangle = J(J+1)\,|J, m_z\rangle$), or a coherent spin state (illustrated in the upper and lower parts of Fig. 3a, respectively). The state then evolves for an interrogation time τ. A subsequent $\pi/2$ pulse enables the measurement of the population difference between the $m_z = 5/2$ and $m_z = -5/2$ levels, from which the magnetic field is inferred. Figure 3a illustrates the protocol. The authors demonstrated that, for external magnetic field measurements, the cat state achieves a sensitivity close to the Heisenberg limit, offering a 15 ± 2 dB improvement over the coherent spin state $|\vartheta, \varphi, N\rangle$ (defined in Sec. 3.3.1). Experimental results that corroborate the feasibility of the protocol, are presented in Fig. 3b.

This manuscript is structured as follows. In Chapter 1, we introduce the fundamental concepts of classical parameter estimation theory, including the Cramér-Rao bound and the Fisher Information. Then in Chapter 2 we transition to the quantum domain, presenting the quantum analogs of classical estimation concepts, with a focus on the quantum Cramér-Rao bound and the Quantum Fisher Information (QFI). Chapter 3 explores the principles of quantum metrology, defining the Standard Quantum Limit and the Heisenberg Limit, and discussing various quantum-enhanced measurement strategies. Finally, in Chapter 4 we address quantum metrology in the presence of noise, particularly depolarizing and axis-misspecification channels, and investigate the use of ancilla-assisted strategies to preserve metrological advantage. The appendices provide additional mathematical details and supporting material relevant to the main text.

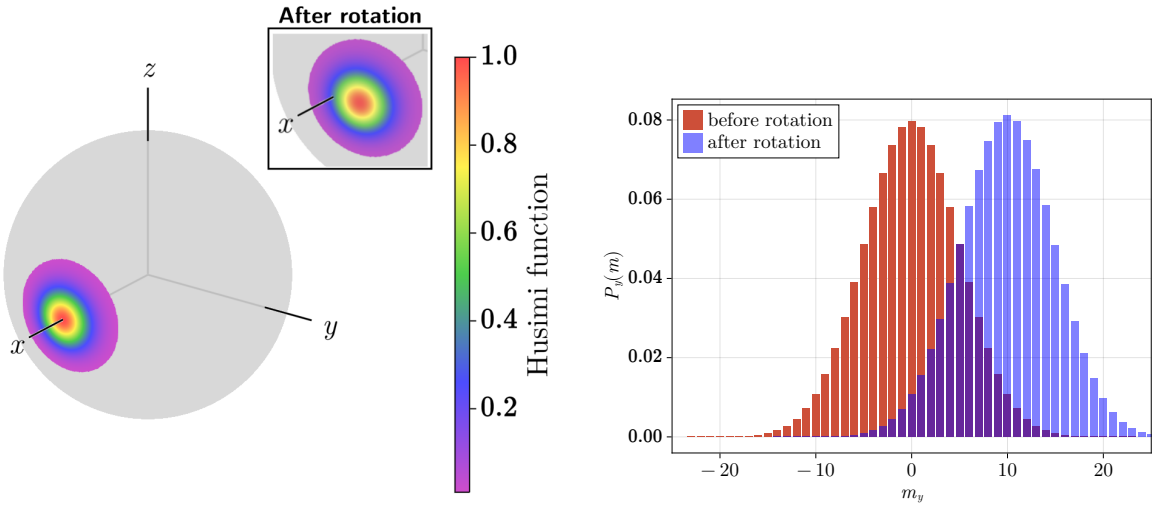

(a) Coherent spin state $|\pi/2, 0, N\rangle$ pointing in the $\mathbf{s} = (\sin\vartheta\cos\varphi, \sin\vartheta\sin\varphi, \cos\vartheta)$ direction(here $\mathbf{s} = \hat{x}$, with $\hat{x}$ the x-axis direction).

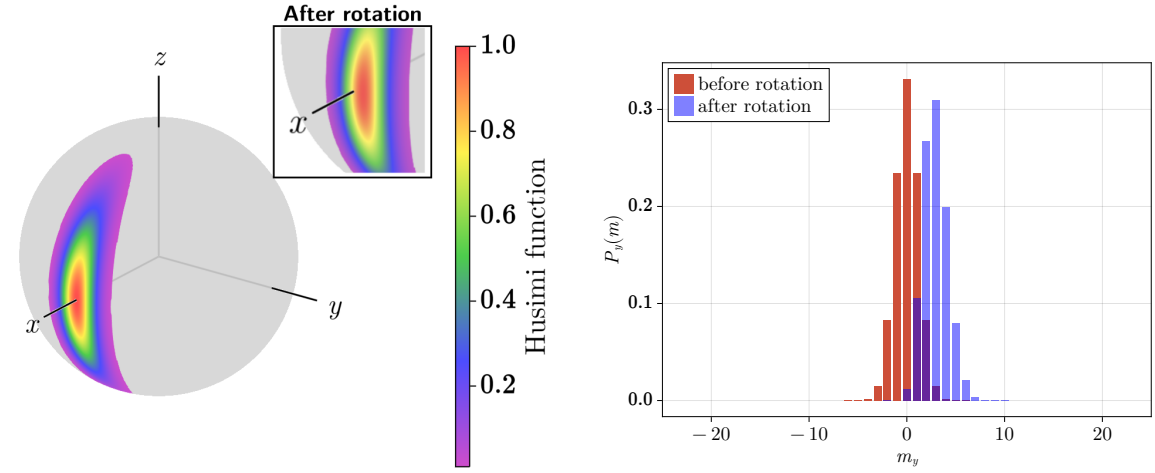

(b) Squeezed spin state. $\xi_R^2 = 0.1$, $J_\perp = J_y$ since $J_\mathbf{s} = J_x$ and $J_\mathbf{n} = J_z$.

Figure 2: **Left**: Husimi distribution of (a) a coherent spin state and (b) a squeezed spin state. The values of the Husimi function lower than 0.01 are displayed in gray. **Right**: Spin probability distribution $P_y(m) = |\langle m_y|\psi\rangle|^2$ along the y direction (red histograms) with $|m_y\rangle$ the common eigenvectors of the angular momentum operators J_y and $\mathbf{J}^2$,with $J_y|m_y\rangle = m_y|m_y\rangle$ and $\mathbf{J}^2|m_y\rangle = J(J+1)|m_y\rangle$. The blue histograms is $P_y(m) = |\langle m_y|e^{-i\theta J_z}|\psi\rangle|^2$ obtained after a rotation of the state. Here $N = 100$, $\theta = 2/\sqrt{N}$ in (a) and $\theta = 2\xi_R/\sqrt{N}$ in (b).

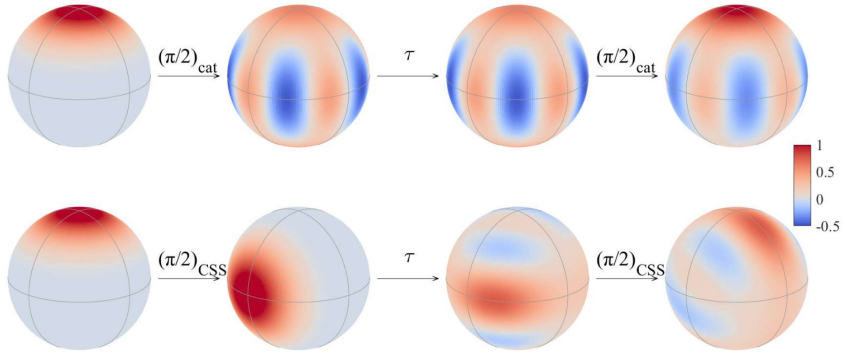

(a)

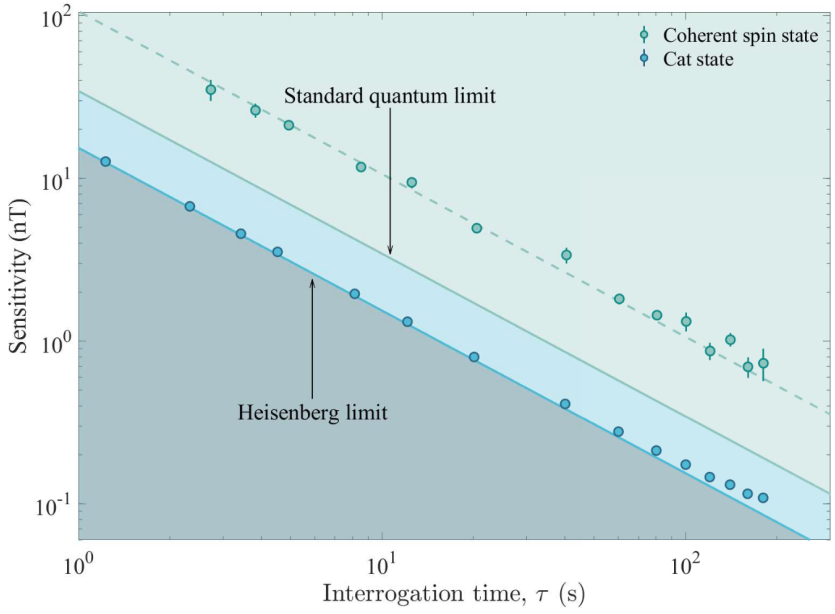

(b)

Figure 3: (Taken from Ref. [19]). **(a)** Ramsey interferometry protocol with spin-J Rydberg atoms ($J = 5/2$). States are represented by their Wigner distribution plotted on the sphere. Top: the initial state is a Schrödinger-cat state $|\psi_{\pm J}\rangle = 1/\sqrt{2}(|J, J\rangle + e^{i\phi}\,|J, -J\rangle)$. Bottom: the initial state is a coherent-spin state $|\theta, \phi\rangle = e^{-i\phi J_z} e^{-i\theta J_y}\,|J, J\rangle$ with $J_{x,y,z}$ the angular momentum operators. **(b)** Sensitivity to a magnetic field. Blue points shows the magnetic sensitivity of the cat state as a function of τ; the green points are for the coherent spin state. Heisenberg limit and Standard quantum limit are displayed for comparison.

Chapter 1

Classical parameter estimation theory

1.1 The problem of parameter estimation

The core issue in classical parameter estimation is as follows: we examine a known random process that depends on one or more unknown parameters. By repeating the process, we acquire a set of data, and from it we try to infer the value of the unknown parameters.

Since the problem involves random processes, one way to formalise parameter estimation theory is by using probability theory. The treatment of probabilities is based on the axiomatic approach developed by A. N. Kolmogorov. As this paper does not focus directly on this theory, we will not explore it in detail. Interested readers can refer to the iconic book 'Foundations of the Theory of Probability' by A. Kolmogorov [21].

The following sections will introduce some important definitions. The majority of the concepts and definitions in this chapter are derived from the book 'Statistical Inference' by Casella and Berger (2002) [22].

1.1.1 Parametric families

A random process is represented by a random variable X. An *observation* is the observed value of X when the random process is executed. If the outcome of the process is a real number, we have a scalar random variable; when the random process has multiple real outcomes, we have a multivariate random variable. Since we will only deal with real random variables, we will omit the term "real" and will not specify whether X is scalar or multivariate unless required.

When the set of possible outcomes of the process is countable, we say that the random variable X is discrete. We denote the probability that X takes the value x_i as $\mu(x_i)$ or $\mu(X = x_i)$, indicating that the random variable X follows the distribution μ. In contrast, when the set of possible outcomes of the process is uncountable, the random variable X is considered continuous. Naturally, we introduce the probability density $\mu(x)$ along with its normalization condition

$$\sum_i \mu(x_i) = 1 \quad \text{or} \int \mathrm{d}x\, \mu(x) = 1. \tag{1.1}$$

We will not specify whether a random variable is continuous or discrete. For simplicity, we will use the notation for continuous random variables, and we will use the notation $X \sim \mu$ to say that a random variable is distributed according to μ.

We will now present the framework of the classical parameter estimation theory. Starting with a random variable X and a parametric family of distribution $\{\mu_\theta\}_{\theta\in\Theta}$. This means that we

know X follows a probability density μ_θ, but the value of θ remains unknown to us. Crucially, we assume that the parameter θ is a deterministic parameter[1].

1.1.2 *n*-samples

The parameter is often estimated by performing the process several times, collecting all the outcomes, and then using this data to infer a value for θ. This situation is best described using *n-samples*. Formally, an *n-sample* is a multivariate random variable $X^{(n)}$ composed of n times the original random variable X,

$$X^{(n)} \overset{\text{def}}{=} (X_1, X_2, \cdots, X_n) \equiv \{X_i\} \quad \text{with} \quad X_i \sim \mu_\theta. \tag{1.2}$$

It is important to not confuse the n-sample with the data; strictly speaking, the data is the realization of the n-sample and not the n-sample itself. Since the X_i's are independent we can write the joint distribution $\mu_\theta^{(n)}$ of the n-sample as

$$\mu_\theta^{(n)}\left(X_1 = x_1, \cdots, X_N = x_n\right) = \prod_{i=1}^{n} \mu_\theta(X_i = x_i). \tag{1.3}$$

1.1.3 Estimators

Now that we have defined the concepts of probability distribution and n-sample, we can formulate the question that parameter estimation theory seeks to address: *knowing the form of a probability distribution and having a realisation of an n-sample of it, what can we say about the value of* θ [24]?

Although more precise, this question is still somewhat vague, and we need to clarify the objectives of the estimation. The first key constraint is that our estimated value must be realistic. For example, suppose that we are estimating a temperature in Kelvin. If after performing the process n times, we obtain a negative value from the data, it would clearly be a poor estimate. Therefore, our first requirement is that the estimated value of θ should be within the parameter space Θ. This requirement essentially defines the concept of an estimator, which we will now formalise.

We define an *estimator* of the parameter $\theta \in \Theta$ as a function $\hat{\theta}_{\text{est}}$ of the n-sample of X, where the realisations of X take values in $\mathcal{A}$. Schematically, we have

$$(X_1, X_2, \ldots, X_n) \xrightarrow{\hat{\theta}_{\text{est}}} \hat{\theta}_{\text{est}}(X_1, X_2, \ldots, X_n) \xrightarrow{\text{realization}} \hat{\theta}_{\text{est}}(x_1, x_2, \ldots, x_n) \in \Theta\,. \tag{1.4}$$

It is sufficient to remember that an estimator is a function mapping the n-sample to the parameter space. Since the n-sample is a random variable and the estimator is a function of the n-sample, the estimator is also a random variable. Importantly, this implies that we can define the mean or variance of an estimator.

Risk function

Now that we have defined what an estimator is, we need a way to compare estimators and determine whether they are good or bad. For this purpose, we define the cost function $c(\hat{\theta}_{\text{est}}(\{x_i\}), \theta)$, where $\hat{\theta}_{\text{est}}(\{x_i\})$ is the value of the estimator when the realisation of the n-sample is $\{X_i = x_i\}$, as a positive function equal to 0 when the estimate matches the actual value of the parameter

[1] The case where θ is considered as a random parameter itself is treated by Bayesian parameter estimation [23].

$c(\theta, \theta) = 0$. The risk function is then defined as the expectation value of the cost function $r(\hat{\theta}_{\text{est}}(\{x_i\}), \theta) \overset{\text{def}}{=} \mathbb{E}\left[c(\hat{\theta}_{\text{est}}(\{x_i\}), \theta)\right]$. An estimator is said to be optimal if it minimises the risk function.

The most common cost function used is the squared difference between the estimate and the parameter, this indeed leads to the risk function called Mean Square Error (MSE) and thus is defined by [22, 25, 24]

$$\text{MSE}[\hat{\theta}_{\text{est}}] \overset{\text{def}}{=} \mathbb{E}\left[(\hat{\theta}_{\text{est}} - \theta)^2\right] . \tag{1.5}$$

Bias of estimators

A reasonable condition to impose on estimators is the unbiasedness condition. The bias $b(\hat{\theta}_{\text{est}})$ of an estimator is defined as

$$b(\hat{\theta}_{\text{est}}) \overset{\text{def}}{=} \mathbb{E}\left[\hat{\theta}_{\text{est}}\right] - \theta . \tag{1.6}$$

An estimator is considered unbiased if its bias is zero for all parameters values, $b(\hat{\theta}_{\text{est}}) = 0$, which means that the expected value of the estimator is equal to the true value of the parameter, $\mathbb{E}\left[\hat{\theta}_{\text{est}}\right] = \theta$. When the unbiasedness condition is satisfied, the frequentist interpretation of probability guarantees that, by repeating the estimation process many times, the results will converge to the true value of the parameter.

Variance of estimators

The variance measures the average deviation of a random variable from its expected value, and for unbiased estimators, this corresponds to the average deviation from the true value of the parameter. It is defined as

$$\text{Var}[\hat{\theta}_{\text{est}}] \overset{\text{def}}{=} \mathbb{E}\left[(\hat{\theta}_{\text{est}} - \mathbb{E}[\theta])^2\right] . \tag{1.7}$$

From this, we can write a general formula for the MSE in terms of the variance and bias

$$\text{MSE}[\hat{\theta}_{\text{est}}] = \text{Var}[\hat{\theta}_{\text{est}}] + b(\hat{\theta}_{\text{est}})^2 . \tag{1.8}$$

Since $b(\hat{\theta}_{\text{est}}) = 0$ for unbiased estimators, the MSE is equal to the variance for those estimators.

Maximum likelihood estimator

An important estimator is the maximum likelihood estimator. We start with the n-sample $\{X_i\}$ and a specific realisation of it $\{x_i\}$. Given this realisation, we can ask the following question: *What is the most likely value of θ such that the result is $\{x_i\}$?* Intuitively, the answer is the value that maximizes the likelihood $l(\theta; x)$ defined as

$$l(\theta; x) \overset{\text{def}}{=} \mu_\theta(x). \tag{1.9}$$

As you can see, the likelihood is equal to the probability distribution evaluated at x. We introduce this new notation to clarify the roles of θ and X. The notation $\mu_\theta(X)$ highlights the connection to the random variable X. When we write $\mu_\theta(X = x)$, it is meant to represent the probability of observing x as the outcome. The notation $l(\theta; x)$ is used to highlight the dependence on θ. The interpretation being that we already observed x, which is therefore considered fixed, and ask ourselves how *likely* it was that the parameter had the value θ.

From a chronological perspective, probability refers to a statement made before the experiment, while likelihood refers to a statement made after the experiment has been conducted and the value x has been observed. For practical reasons, we introduce the log-likelihood L as

$$L(\theta; x) \overset{\text{def}}{=} \ln\left(l(\theta; x)\right) . \tag{1.10}$$

As we can see, the log-likelihood may diverge when the likelihood approaches zero. However, this corresponds to a probability of zero for the observed value x of the random variable X, which is not possible—by definition, the observed outcome must have a non-zero probability. Since the logarithm is a monotonic function, the maximum of the likelihood is also the maximum of the logarithmic likelihood. From this we define the *maximum likelihood estimator* (MLE) $\hat{\theta}_{\text{mle}}$ of θ as the value that maximizes the log-likelihood

$$\hat{\theta}_{\text{mle}} : \mathcal{B}(\mathbb{R}^n) \to \Theta,\ x \to \underset{\theta\in\Theta}{\text{argmax}}\, L(\theta; x) . \tag{1.11}$$

Intuitively, this selects the parameter values that make the data most probable. Since we will use an n-sample $X^{(n)}$ in the estimation procedure, the maximum likelihood estimator becomes $\hat{\theta}_{\text{mle}} = \text{argmax}_{\theta\in\Theta}\, L(\theta; \{x_i\})$, where the total log-likelihood is

$$L(\theta; \{x_i\}) = \sum_i \ln\left(\mu_\theta(X_i = x_i)\right) . \tag{1.12}$$

1.2 Lower bound for the variance

In the previous section, we discussed two important properties of estimators: bias and mean squared error (MSE), which the latter equals the variance for unbiased estimators. These properties are related to the efficiency of estimators. Ideally, we aim for estimators that minimise the variance. However, the existence of such an estimator is not guaranteed, as the same estimator may not minimise the variance for different values of the parameter.

An alternative approach is to minimise the variance locally, which would provide a limit to assess the quality of an estimator. However, calculating such a "local variance" is generally difficult. Instead, we will derive a lower bound for the variance. To do this, we will first explain the Cramér-Rao theorem and then present its proof.

1.2.1 Cramér-Rao theorem

Theorem 1.1. *Let θ be an unknown deterministic parameter that is to be estimated by observation of a random variable X distributed according to a family of probability distribution μ_θ. Let us suppose that we can interchange derivative and limits, which constitutes the regularity condition. The variance of an unbiased estimator $\hat{\theta}_{\text{est}}$ of θ (i.e. $\mathbb{E}\left[\hat{\theta}_{\text{est}}\right] = \theta$) is then bounded by the inverse of the Fisher information $\mathrm{J}(\mu_\theta; \theta)$,*

$$\text{Var}[\hat{\theta}_{\text{est}}] \geq \frac{1}{\mathrm{J}(\mu_\theta; \theta)} , \tag{1.13}$$

where $\mathrm{J}(\mu_\theta; \theta) = \mathbb{E}\left[\left(\frac{\partial \ln(\mu_\theta(x))}{\partial\theta}\right)^2\right]$.

An estimator is said to be *efficient* if it saturates the bound. This theorem leads to a corollary if we are no longer interested in estimating θ but instead in estimating a function $g(\theta)$ of θ.

Corollary 1.1. *Let us assume that the condition of Theorem 1.1 is fulfilled and suppose that $g(\theta)$ is a smooth function of θ. Then the variance of $\hat{g}_{est}$, an unbiased estimator of $g(\theta)$, is bounded as*

$$\mathrm{Var}[\hat{g}_{est}] \geq \frac{\left(\frac{\partial g(\theta)}{\partial \theta}\right)^2}{\mathrm{J}(\mu_\theta;\theta)} \,. \tag{1.14}$$

1.2.2 Proof of the Cramér-Rao theorem

The proof is largely inspired by the work of H. Cramér and C. R. Rao [26]. Let us consider a general case where want to estimate not the parameter θ directly but a function of it, $g(\theta)$. This is done by an estimator $\hat{g}_{\mathrm{est}}$. By definition $\theta \in \Theta$, and so $g(\theta)$ is defined as $g : \Theta \to \mathcal{G}, \theta \mapsto g(\theta)$. The proof relies on the Cauchy-Schwarz inequality [27] and is straightforward to derive. We start by investigating the following equation

$$\mathbb{E}\left[\frac{\partial \ln(\mu_\theta(x))}{\partial \theta}\right] = \int \mathrm{d}x \frac{\partial \mu_\theta(x)}{\partial \theta} \,, \tag{1.15}$$

Since we suppose the regularity condition to hold, we can interchange the derivative and the integral

$$\mathbb{E}\left[\frac{\partial \ln(\mu_\theta(x))}{\partial \theta}\right] = \frac{\partial}{\partial \theta}\int \mathrm{d}x \; \mu_\theta(x) \,. \tag{1.16}$$

This is of course equal to zero because of the definition of a probability distribution and thus we obtain

$$\mathbb{E}\left[\frac{\partial \ln(\mu_\theta(x))}{\partial \theta}\right] = 0 \,, \tag{1.17}$$

which is a consequence of the regularity condition.

Next, we examine the second requirement in the theorem. By differentiating both sides of the unbiasedness condition $\int \mathrm{d}x \, \mu_\theta(x) \, \hat{g}_{\mathrm{est}} = g(\theta)$ with respect to θ and interchanging the derivative and the integral, we obtain

$$\frac{\partial g(\theta)}{\partial \theta} = \frac{\partial}{\partial \theta}\int \mathrm{d}x \, \mu_\theta(x) \, \hat{g}_{\mathrm{est}} = \int \mathrm{d}x \, \mu_\theta(x) \frac{\partial \ln(\mu_\theta(x))}{\partial \theta} \hat{g}_{est} \,. \tag{1.18}$$

Remember that the estimator $\hat{g}_{\mathrm{est}}$ does not depend on the value of θ; only its expected value does. This dependence arises from the probability distribution, not from the estimator itself. Multiplying both sides of Eq. (1.17) by $g(\theta)$, we get

$$\int \mathrm{d}x \, \mu_\theta(x) \frac{\partial \ln(\mu_\theta(x))}{\partial \theta} g(\theta) = 0 \,. \tag{1.19}$$

By subtracting Eq. (1.19) from Eq. (1.18), we finally obtain

$$\frac{\partial g(\theta)}{\partial \theta} = \int \mathrm{d}x \, \mu_\theta(x) \frac{\partial \ln(\mu_\theta(x))}{\partial \theta} (\hat{g}_{\mathrm{est}} - g(\theta)) \,. \tag{1.20}$$

Now that we have all the ingredients, the last step is the application of the Cauchy-Schwarz inequality. In order to use it, we must define a scalar product $\langle \cdot, \cdot \rangle_{\mu_\theta}$ with respect to μ_θ. For two real functions $a(x)$ and $b(x)$ and a probability distribution $\mu_\theta(x)$, we define the scalar product between a and b as

$$\langle a(x), b(x) \rangle_{\mu_\theta} \stackrel{\mathrm{def}}{=} \int \mathrm{d}x \, a(x) \, b(x) \mu_\theta(x) \,. \tag{1.21}$$

With this definition, we can rewrite the Eq. (1.20) as

$$\frac{\partial g(\theta)}{\partial \theta} = \left\langle \frac{\partial \ln(\mu_\theta(x))}{\partial \theta}, \hat{g}_{\text{est}} - g(\theta) \right\rangle_{\mu_\theta} . \tag{1.22}$$

We can now apply the inequality to obtain

$$\left\langle \frac{\partial \ln(\mu_\theta(x))}{\partial \theta}, \hat{g}_{\text{est}} - g(\theta) \right\rangle_{\mu_\theta}^2 \leq \left\langle \frac{\partial \ln(\mu_\theta(x))}{\partial \theta}, \frac{\partial \ln(\mu_\theta(x))}{\partial \theta} \right\rangle_{\mu_\theta} \langle \hat{g}_{\text{est}} - g(\theta), \hat{g}_{\text{est}} - g(\theta) \rangle_{\mu_\theta} . \tag{1.23}$$

Finally, we can write

$$\int \mathrm{d}x\, \mu_\theta(x)(\hat{g}_{\text{est}} - g(\theta))^2 \geq \frac{\left(\frac{\partial g(\theta)}{\partial \theta}\right)^2}{\int \mathrm{d}x\, \mu_\theta(x) \left(\frac{\partial \ln(\mu_\theta(x))}{\partial \theta}\right)^2} . \tag{1.24}$$

Since the definition of the variance of an estimator is $\mathrm{Var}[\hat{g}_{\text{est}}] = \int \mathrm{d}x\, \mu_\theta(x)(\hat{g}_{\text{est}} - g(\theta))^2$, we obtain the Cramér-Rao bound

$$\mathrm{Var}[\hat{g}_{\text{est}}] \geq \frac{\left(\frac{\partial g(\theta)}{\partial \theta}\right)^2}{\mathrm{J}(\mu_\theta; \theta)}, \tag{1.25}$$

with $\mathrm{J}(\mu_\theta; \theta) = \int \mathrm{d}x\, \mu_\theta(x) \left(\frac{\partial \ln(\mu_\theta(x))}{\partial \theta}\right)^2$.

The original Cramér-Rao bound Eq. (1.1) is then obtained by taking $g(\theta) = \theta$.

1.3 Fisher Information

The Fisher information, denoted by J, is a key quantity in the Cramér-Rao theorem. The reciprocal of J sets the lower bound for the variance of unbiased estimators. A larger J leads to a smaller lower bound, implying that more information can be extracted from the probability distribution. This gives J the role of quantifying the amount of information about θ contained in μ_θ. From this perspective, J can also be viewed as a measure of the sensitivity of μ_θ with respect to θ.

1.3.1 Additivity of the FI

In practice, we often use repeated observations of the random process to estimate θ, which is represented by an n-sample $X^{(n)}$. Let's adapt the bound for this specific case. From Eq. (1.3), we get

$$\ln\left(\mu_\theta^{(n)}(\{x_i\})\right) = \sum_{i=1}^{n} \ln \mu_\theta(x_i) . \tag{1.26}$$

Thus the Fisher information for the n-sample is

$$\mathrm{J}(\mu_\theta^{(n)}; \theta) = \int \mathrm{d}x_1 \mu_\theta(x_1) \cdots \int \mathrm{d}x_n \mu_\theta(x_n) \left(\sum_{i,j} \frac{\partial \ln(\mu_\theta(x_i))}{\partial \theta} \frac{\partial \ln(\mu_\theta(x_j))}{\partial \theta} \right) . \tag{1.27}$$

We can separate diagonal and off-diagonal terms of the last equation and use the normalization condition of each distribution $\int \mathrm{d}x_i \mu_\theta(x_i) = 1 \ \ \forall i$, we thus obtain

$$\mathrm{J}(\mu_\theta^{(n)};\theta) = \underbrace{n \int \mathrm{d}x \mu_\theta(x) \left(\frac{\partial \ln(\mu_\theta(x))}{\partial \theta} \right)^2}_{\text{diagonal terms}} + \underbrace{n(n-1) \left(\int \mathrm{d}x \mu_\theta(x) \frac{\partial \ln(\mu_\theta(x))}{\partial \theta} \right)^2}_{\text{off-diagonal terms}} . \tag{1.28}$$

From this we can adapt the regularity condition Eq. (1.17) for an n-sample, $\mathbb{E}\left[\ln(\mu_\theta^{(n)})\right] = 0$ which gives us

$$n \int \mathrm{d}x \mu_\theta(x) \frac{\partial \ln(\mu_\theta(x))}{\partial \theta} = 0 . \tag{1.29}$$

This leads to vanishing off-diagonal terms in Eq. (1.28) and finally we get

$$\mathrm{J}(\mu_\theta^{(n)};\theta) = n\mathrm{J}(\mu_\theta;\theta) . \tag{1.30}$$

This is the additivity of the Fisher information. With this property we can express the Cramér-Rao bound for n-sample as follows

$$\mathrm{Var}[\hat{\theta}_{\mathrm{est}}] \geq \frac{1}{n\,\mathrm{J}(\mu_\theta;\theta)} . \tag{1.31}$$

This expression has significant implications in quantum metrology, as it establishes the standard scaling achieved through repeated experiments.

1.4 Multi-parameter estimation

Sometimes, we aim to estimate the values of multiple parameters simultaneously. In this case, some adjustments are necessary to the previous discussion. In multiparameter estimation (also known as vector parameter estimation), one seeks to estimate a vector parameter $\boldsymbol{\theta} \overset{\mathrm{def}}{=} \{\theta_i\}$. The corresponding Cramér-Rao bound corresponds to the following inequality involving the covariance matrix [28]

$$\mathrm{Cov}[\hat{\boldsymbol{\theta}}_{\mathrm{est}}] \geq \boldsymbol{J}(\mu_{\boldsymbol{\theta}};\boldsymbol{\theta})^{-1} , \tag{1.32}$$

where the elements of $\boldsymbol{J}(\mu_{\boldsymbol{\theta}};\boldsymbol{\theta})^{-1}$ are defined as

$$(\boldsymbol{J}(\mu_{\boldsymbol{\theta}};\boldsymbol{\theta}))_{ij} \overset{\mathrm{def}}{=} \mathbb{E}\left[\frac{\partial \ln(\mu_\theta)}{\partial \theta_i} \frac{\partial \ln(\mu_\theta)}{\partial \theta_j} \right] . \tag{1.33}$$

The inequality (which we use in the sense that if $A \geq B$, then $A - B$ is a positive semidefinite matrix) in Eq. (1.32) expresses the classical Cramér-Rao bound, setting a lower bound on the covariance matrix of any unbiased estimator. When the Fisher information matrix is diagonal, it implies that the estimation of each parameter is independent of the others, meaning that the presence or uncertainty of other parameters does not influence the precision of estimating a given one. In contrast, off-diagonal elements indicate coupling between parameters, which can degrade estimation precision due to parameter crosstalk. On the other hand, the elements of the covariance matrix are

$$\left(\mathrm{Cov}[\hat{\boldsymbol{\theta}}_{\mathrm{est}}]\right)_{ij} \overset{\mathrm{def}}{=} \mathrm{Cov}[\hat{\theta}_i, \hat{\theta}_j] = \mathbb{E}\left[(\hat{\theta}_i - \mathbb{E}[\hat{\theta}_i])(\hat{\theta}_j - \mathbb{E}[\hat{\theta}_j]) \right] \tag{1.34}$$

$$= \mathbb{E}\left[(\hat{\theta}_i - \theta_i)(\hat{\theta}_j - \theta_j) \right] . \tag{1.35}$$

We directly see that the last term is equal to the mean squared error. Thus, the covariance matrix is the same as the mean squared error matrix. Note that this is only true for unbiased estimator.

Under a change of parameter $\boldsymbol{g}(\boldsymbol{\theta})$, the inverse of Fisher information matrix is given, as we would expect, by

$$\boldsymbol{J}(\mu_{\boldsymbol{\theta}}; \boldsymbol{g}(\boldsymbol{\theta}))^{-1} = \mathbf{Jac}\left[\boldsymbol{g}(\boldsymbol{\theta}); \{\theta_i\}\right] \cdot \boldsymbol{J}(\mu_{\boldsymbol{\theta}}; \boldsymbol{\theta})^{-1} \cdot \mathbf{Jac}\left[\boldsymbol{g}(\boldsymbol{\theta}); \{\theta_i\}\right]^{\intercal} \ , \tag{1.36}$$

where $\mathbf{Jac}\left[\boldsymbol{g}(\boldsymbol{\theta}); \{\theta_i\}\right]$ is the Jacobian of the transformation with elements $\left(\mathbf{Jac}\left[\boldsymbol{g}(\boldsymbol{\theta}); \{\theta_i\}\right]\right)_{ij} \stackrel{\text{def}}{=} \frac{\partial g_i(\boldsymbol{\theta})}{\partial \theta_j}$. When the Fisher information matrix is diagonal, estimating a parameter θ_i is not influenced by the uncertainty surrounding other parameters; in this case, multiparameter estimation is essentially equivalent to conducting multiple independent single-parameter estimations. Although we can locally define a set of coordinates that makes the Fisher information matrix diagonal, it is generally not feasible to establish a global set of coordinates that maintains this diagonal form.

Chapter 2

Quantum parameter estimation theory

This chapter aims to present the fundamental principles of quantum parameter estimation theory (abbreviated as QPE), with the main objective of providing a physical understanding of parameter estimation theory, adapting the Cramér-Rao bound to a quantum version, and defining quantum Fisher information.

The idea behind QPE is to estimate a parameter encoded in a quantum system. We want to obtain information on the parameter by making some measurements. The kind of measurement used in quantum mechanics is described by POVMs which stands for *Positive Operator Valued Measure*. A POVM is a set $\{M_\xi\}$ of positive operators M_ξ with the condition $\sum_\xi M_\xi = \mathbb{1}$, where $\mathbb{1}$ is the identity operator. The probability $p(\xi)$ of obtaining the measurement outcome ξ when measuring a quantum system in a state described by its density matrix ρ is

$$p(\xi) = \mathrm{Tr}[M_\xi \rho] \,, \tag{2.1}$$

with $\mathrm{Tr}\,[\cdot]$ the trace operation. For more information on POVMs, see Appendix A. From here, we can express the main question of QPE : *given a parametric family of states* $\{\rho_\theta\}$*, what can we say about the value of the parameter* θ*?* [24].

A starting point for answering this question is to present the quantum version of the Cramér-Rao theorem.

2.1 Quantum Cramér-Rao bound

2.1.1 Quantum Cramér-Rao theorem

Theorem 2.1. *Let* $\{\rho_\theta\}$ *be a family of quantum states that depends on a scalar parameter* $\theta \in \Theta$*. The variance* $\mathrm{Var}[\hat{\theta}_{\mathrm{est}}]$ *of a locally unbiased estimator* $\hat{\theta}_{\mathrm{est}}$ *at* $\theta = \theta_0$*,*

$$\mathbb{E}\left[\hat{\theta}_{\mathrm{est}}\right]\Big|_{\theta_0} = \theta_0, \qquad \frac{\partial}{\partial\theta}\mathbb{E}\left[\hat{\theta}_{\mathrm{est}}\right] = 1 \,, \tag{2.2}$$

is bound by the inverse of the Quantum Fisher Information (QFI) $I(\rho_\theta\,;\,\theta)$*,*

$$\mathrm{Var}[\hat{\theta}_{\mathrm{est}}] \geq \frac{1}{I(\rho_\theta\,;\,\theta)} \quad \text{with} \quad I(\rho_\theta\,;\,\theta) \overset{\mathrm{def}}{=} \mathrm{Tr}\left[L^2_{\rho_\theta}\rho_\theta\right] , \tag{2.3}$$

where L_{ρ_θ} *is the symmetric logarithmic derivative (SLD) defined implicitly through*

$$\frac{\partial\rho_\theta}{\partial\theta} = \frac{L_{\rho_\theta}\rho_\theta + \rho_\theta L_{\rho_\theta}}{2} \,. \tag{2.4}$$

In addition to Theorem 2.1, we can derive another theorem which consists in expressing the QFI as the maximal FI over all possible POVMs [29].

Theorem 2.2. *The QFI is equal to*

$$I(\rho_\theta\,;\,\theta) = \max_{\{M_\xi\}\in\text{POVMs}} \mathrm{J}(p_\theta(\xi)\,;\,\theta) \tag{2.5}$$

with

$$\mathrm{J}(p_\theta\,;\,\theta) = \int \mathrm{d}\xi\; p_\theta(\xi) \left(\frac{\partial \ln(p_\theta(\xi))}{\partial\theta}\right)^2 = \int \mathrm{d}\xi\; \frac{1}{\mathrm{Tr}\left[\rho_\theta M_\xi\right]} \mathrm{Tr}\left[\frac{\partial\rho_\theta}{\partial\theta} M_\xi\right]^2 . \tag{2.6}$$

2.1.2 Proof of the quantum Cramér-Rao theorem

The section is largely inspired by the work of J. Fraisse [24], which provides a physical interpretation of the proof[1].

Let us define a family of probability distributions $p_\theta(\xi)$ using the state ρ_θ and a POVM $\{M_\xi\}$ as $p_\theta(\xi) = \mathrm{Tr}[\rho_\theta M_\xi]$. Based on this, we can express the corresponding FI from Theorem 1.1 as follows

$$\mathrm{J}(p_\theta;\theta) = \int \mathrm{d}\xi\; \frac{1}{\mathrm{Tr}[\rho_\theta M_\xi]} \mathrm{Tr}\left[\frac{\partial\rho_\theta}{\partial\theta} M_\xi\right]^2 . \tag{2.7}$$

In this case, we have a probability distribution defined through POVMs, which can take different values and, consequently, yield a different Fisher information, thus different bounds. The idea is to find the most tight bound (which is the most informative). In order to find the most informative bound, we need to maximise the FI over all POVMs.

We start by introducing again the symmetric logarithmic derivative (SLD) L_{ρ_θ} with its implicit definition

$$\frac{\partial\rho_\theta}{\partial\theta} = \frac{L_{\rho_\theta}\rho_\theta + \rho_\theta L_{\rho_\theta}}{2} . \tag{2.8}$$

We know that ρ_θ is Hermitian (as well as its derivative with respect to θ). Consequently, we have $\rho_\theta L_{\rho_\theta}^\dagger + L_{\rho_\theta}^\dagger\rho_\theta = L_{\rho_\theta}\rho_\theta + \rho_\theta L_{\rho_\theta}$ or equivalently, $[L_{\rho_\theta} - L_{\rho_\theta}^\dagger, \rho_\theta] = 0$. To fulfill this condition, we require either that both operators in the commutator share the same eigenvectors, or that the SLD is Hermitian $L_{\rho_\theta} = L_{\rho_\theta}^\dagger$. We focus on the latter case. Substituting Eq. (2.8) into Eq. (2.7) yields

$$\mathrm{J}(p_\theta;\theta) = \int \mathrm{d}\xi\; \frac{1}{\mathrm{Tr}\left[\rho_\theta M_\xi\right]} \mathrm{Tr}\left[\left(L_{\rho_\theta}\rho_\theta + \rho_\theta L_{\rho_\theta}\right) M_\xi/2\right]^2 . \tag{2.9}$$

Let us now build some useful inequalities. The first uses $\Re(x)^2 \leq |x|^2$, where $\Re(\cdot)$ denotes the real part and the equality is reached when $\Im(x) = 0$, with $\Im(\cdot)$ the imaginary part. Considering the linearity, the cyclic property of the trace and the useful formula $\mathrm{Tr}\left[ABC\right]^* = \mathrm{Tr}\left[C^\dagger B^\dagger A^\dagger\right]$, we can write

$$\begin{aligned}
\mathrm{Tr}\left[\left(L_{\rho_\theta}\rho_\theta + \rho_\theta L_{\rho_\theta}\right) M_\xi/2\right] &= \mathrm{Tr}\left[L_{\rho_\theta}\rho_\theta M_\xi/2\right] + \mathrm{Tr}\left[\rho_\theta L_{\rho_\theta} M_\xi/2\right] \\
&= \mathrm{Tr}\left[L_{\rho_\theta}\rho_\theta M_\xi/2\right] + \mathrm{Tr}\left[L_{\rho_\theta}\rho_\theta M_\xi/2\right]^* \\
&= \Re\left(\mathrm{Tr}\left[L_{\rho_\theta}\rho_\theta M_\xi\right]\right) \\
\Rightarrow \mathrm{Tr}\left[\left(L_{\rho_\theta}\rho_\theta + \rho_\theta L_{\rho_\theta}\right) M_\xi/2\right]^2 &\leq \left|\mathrm{Tr}\left[L_{\rho_\theta}\rho_\theta M_\xi\right]\right|^2 .
\end{aligned} \tag{2.10}$$

[1] J. Fraisse also presents a more mathematical proof for the quantum CR theorem. The readers interested can find it in [24].

From the Cauchy-Schwarz inequality we know that

$$\left|\mathrm{Tr}\left[A^\dagger B\right]\right|^2 \leq \mathrm{Tr}\left[A^\dagger A\right]\mathrm{Tr}\left[B^\dagger B\right] \ . \tag{2.11}$$

Since the density operator and the POVM elements are positive and Hermitian operators we can decompose them into $\rho_\theta = \rho_\theta^{1/2}\rho_\theta^{1/2}$ and $M_\xi = M_\xi^{1/2}M_\xi^{1/2}$. Once again using the cyclic property of the trace, we can write the following equality

$$\frac{\left|\mathrm{Tr}\left[L_{\rho_\theta}\rho_\theta M_\xi\right]\right|^2}{\mathrm{Tr}\left[\rho_\theta M_\xi\right]} = \frac{\left|\mathrm{Tr}\left[\rho_\theta M_\xi L_{\rho_\theta}\right]\right|^2}{\mathrm{Tr}\left[\rho_\theta M_\xi\right]} = \left|\mathrm{Tr}\left[\frac{\rho_\theta^{1/2}M_\xi^{1/2}}{\sqrt{\mathrm{Tr}\left[\rho_\theta M_\xi\right]}}M_\xi^{1/2}L_{\rho_\theta}\rho_\theta^{1/2}\right]\right|^2 \ . \tag{2.12}$$

The last step is possible because of the hermiticity of $\rho_\theta^{1/2}$ and $M_\xi^{1/2}$. We can now identify $A = \frac{\rho_\theta^{1/2}M_\xi^{1/2}}{\sqrt{\mathrm{Tr}\left[\rho_\theta M_\xi\right]}}$ and $B = M_\xi^{1/2}L_{\rho_\theta}\rho_\theta^{1/2}$ and use the CS inequality (2.11) to obtain

$$\frac{\left|\mathrm{Tr}\left[L_{\rho_\theta}\rho_\theta M_\xi\right]\right|^2}{\mathrm{Tr}\left[\rho_\theta M_\xi\right]} \leq \frac{\mathrm{Tr}\left[\rho_\theta M_\xi\right]}{\mathrm{Tr}\left[\rho_\theta M_\xi\right]}\mathrm{Tr}\left[M_\xi L_{\rho_\theta}\rho_\theta L_{\rho_\theta}\right] = \mathrm{Tr}\left[M_\xi L_{\rho_\theta}\rho_\theta L_{\rho_\theta}\right] \ . \tag{2.13}$$

We can now combine the inequalities Eq. (2.10) and Eq. (2.13) with Eq. (2.9) and thus get

$$\begin{aligned}
\mathrm{J}(p_\theta;\theta) &= \int \mathrm{d}\xi \, \frac{1}{\mathrm{Tr}\left[\rho_\theta M_\xi\right]}\mathrm{Tr}\left[\left(L_{\rho_\theta}\rho_\theta + \rho_\theta L_{\rho_\theta}\right)M_\xi/2\right]^2 \\
&\leq \int \mathrm{d}\xi \, \frac{1}{\mathrm{Tr}\left[\rho_\theta M_\xi\right]}\left|\mathrm{Tr}\left[L_{\rho_\theta}\rho_\theta M_\xi\right]\right|^2 \\
&\leq \int \mathrm{d}\xi \ \mathrm{Tr}\left[M_\xi L_{\rho_\theta}\rho_\theta L_{\rho_\theta}\right] \ .
\end{aligned} \tag{2.14}$$

Finally, we can invert the order of the trace and the integral and use the property of POVMs $\int \mathrm{d}\xi M_\xi = \mathbb{1}$ to obtain

$$\int \mathrm{d}\xi \, \mathrm{Tr}\left[M_\xi L_{\rho_\theta}\rho_\theta L_{\rho_\theta}\right] = \mathrm{Tr}\left[\int \mathrm{d}\xi M_\xi L_{\rho_\theta}\rho_\theta L_{\rho_\theta}\right] = \mathrm{Tr}\left[\rho_\theta L_{\rho_\theta}^2\right] \ . \tag{2.15}$$

From the last equation, we see that the Fisher information is bounded by the Quantum Fisher information (QFI), $I(\rho_\theta\,;\,\theta) = \mathrm{Tr}\left[\rho_\theta L_{\rho_\theta}^2\right]$, as

$$\mathrm{J}(p_\theta;\theta) \leq I(\rho_\theta\,;\,\theta) \ . \tag{2.16}$$

We can now use the Cramér-Rao theorem (Theorem 1.1) to find a lower bound to the variance of an unbiased estimator $\hat{\theta}_{\mathrm{est}}$. This bound can be saturated, and the proof is given in Appendix B. If the inequality is saturated, we say that the bound is tight.

2.2 Quantum Fisher Information

In this section, we will provide useful and more convenient ways to express and compute the QFI, to construct the Table 2.1 that summarises the most used expressions of the QFI. We add the expression of the QFI, used in Theorem 2.1 as the first occurrence of the table. We will also provide a geometrical interpretation using the Bures distance.

#	QFI	Expression
1	Expectation value of (SLD)^2	$\mathrm{Tr}\left[\rho_\theta L_{\rho_\theta}^2\right]$
2	Eigenspace expansion form	$\sum_{i=1}^{r} \frac{1}{p_i}\left(\partial_\theta p_i\right)^2 + \sum_{i=1}^{r} 4p_i \left\langle \partial_\theta \psi_i \middle| \partial_\theta \psi_j \right\rangle - \sum_{i,j=1}^{r} \frac{8p_i p_j}{p_i + p_j} \left\lvert \left\langle \psi_i \middle| \partial_\theta \psi_j \right\rangle \right\rvert^2$
3	Integral form	$2\int_0^\infty \mathrm{d}s\, \mathrm{Tr}\left[(\partial_\theta \rho_\theta) e^{-\rho_\theta s} (\partial_\theta \rho_\theta) e^{-\rho_\theta s}\right]$
4	Bures distance form	$4\frac{D_B^2(\rho_\theta\,,\,\rho_{\theta+\mathrm{d}\theta})}{\mathrm{d}\theta^2} = 8\frac{\left(1-\sqrt{\mathcal{F}(\rho_\theta,\rho_{\theta+\mathrm{d}\theta})}\right)}{\mathrm{d}\theta^2}$
5	Pure states form	$4\left(\left\langle \partial_\theta \psi_\theta \middle| \partial_\theta \psi_\theta \right\rangle - \left\lvert \left\langle \psi_\theta \middle| \partial_\theta \psi_\theta \right\rangle \right\rvert^2\right)$
6	Variance of $\partial_\theta H(\theta)$	$4\,\mathrm{Var}[\partial_\theta H(\theta), \lvert\psi_0\rangle]$

Table 2.1: Non-exhaustive list of commonly used forms of the QFI. (1) Form used in the Theorem 2.1 with L_{ρ_θ} the SLD and ρ_θ the parametrized probe state. (2) QFI expressed as a function of the eigenvalues p_i and corresponding eigenvectors $|\psi_i\rangle$ of ρ_θ. (3) Integral form of the QFI, where the SLD is the formal solution of the Lyapunov equation [30]. (4) Geometrical form of the QFI using the Bures distance between the states ρ_θ and $\rho_{\theta+\mathrm{d}\theta}$. (5) Pure states form of the QFI. Identical to the eigenspace expansion form with $\rho_\theta = |\psi_\theta\rangle\langle\psi_\theta|$. (6) QFI expressed as the variance of the derivative of the Hamiltonian $H(\theta) = \theta G$, where G is the generator [24].

2.2.1 General case

Eigenspace expansion

Theorem 2.1 provides a bound to the variance of an estimator related to the Quantum Fisher information. This quantity is defined via the SLD. To have a better-suited form of the QFI, we will here derive a more convenient form of it.

We first need to consider that ρ_θ could not have a full rank. The mathematical considerations are provided here by J. Liu (and co-authors)[31] and E. Serrano-Ensástiga (and co-authors) [32].

Let $\{\rho_\theta\}$ be a family of density operators dependent on θ that live in a Hilbert space of dimension N. The spectral decomposition of a density operator is

$$\rho_\theta = \sum_{i=1}^{r} p_i \left|\psi_i\right\rangle \left\langle\psi_i\right| \ , \tag{2.17}$$

where r is the rank of ρ_θ, i.e., the dimension of the support of ρ_θ ($r = \dim\left[\mathrm{supp}(\rho_\theta)\right]$). $\{p_i, |\psi_i\rangle\}$ are the eigenvalues and eigenvectors of the density operator.

For a given state ρ_θ, the corresponding QFI is

$$I(\rho_\theta\,;\,\theta) = \mathrm{Tr}\left[\rho_\theta L^2\right] \quad \text{with} \quad \frac{\partial \rho_\theta}{\partial \theta} = \frac{1}{2}(L_{\rho_\theta}\rho_\theta + \rho_\theta L_{\rho_\theta}) \ . \tag{2.18}$$

We can express the second part of the above equation in the eigenbasis of ρ_θ as

$$\left(\partial_\theta \rho_\theta\right)_{ij} = \frac{1}{2}\left(p_i + p_j\right) L_{ij} \ , \tag{2.19}$$

with $L_{ij} \overset{\mathrm{def}}{=} \langle\psi_i|L_{\rho_\theta}|\psi_j\rangle$ and $\left(\partial_\theta \rho_\theta\right)_{ij} \overset{\mathrm{def}}{=} \langle\psi_i|\frac{\partial\rho_\theta}{\partial\theta}|\psi_j\rangle$. We can find that L_{ij} is defined for $i, j > r$ and thus can be arbitrarily chosen. However, we will show that in practice, the calculation of

the QFI does not involve L_{ij} with $i, j > r$, and thus one can fix $L_{ij} = 0$ for $i, j > r$ as a matter of convenience.

We can insert Eq. (2.17) and use the closure relation $\sum_{j=1}^{N} |\psi_j\rangle \langle\psi_j| = \mathbb{1}$ (with $\mathbb{1}$ the identity operator) in Eq.(2.18) to obtain

$$I(\rho_\theta\,;\,\theta) = \sum_{i=1}^{r}\sum_{j=1}^{N} p_i L_{ij} L_{ji}\ . \tag{2.20}$$

Since $\sum_{i=1}^{r} p_i = 1$, we got that $p_i > 0$ for $i \leq r$. With this, Eq. (2.19) can be rewritten as

$$L_{ij} = \frac{2\,(\partial_\theta \rho_\theta)_{ij}}{p_i + p_j}\ . \tag{2.21}$$

Utilizing the above relation, Eq. (2.20) can be written as

$$I(\rho_\theta\,;\,\theta) = \sum_{i=1}^{r}\sum_{j=1}^{N} \frac{4p_i}{p_i + p_j} \left|(\partial_\theta \rho_\theta)_{ij}\right|^2\ , \tag{2.22}$$

where the Hermiticity of $\partial_\theta \rho_\theta$ was used. Next, we can use the spectral decomposition and thus find

$$\begin{aligned}
(\partial_\theta \rho_\theta)_{ij} &= \langle\psi_i|\partial_\theta \rho_\theta|\psi_j\rangle \\
&= \langle\psi_i|\partial_\theta \left(\sum_{k=1}^{r} p_k\, |\psi_k\rangle \langle\psi_k|\right)|\psi_j\rangle \\
&= \langle\psi_i| \sum_{k=1}^{r} \left(\partial_\theta p_k\, |\psi_k\rangle \langle\psi_k| + p_k\, |\partial_\theta \psi_k\rangle \langle\psi_k| + p_k\, |\psi_k\rangle \langle\partial_\theta \psi_k|\right)|\psi_j\rangle \\
&= \partial_\theta p_i \delta_{ij} + p_i \langle\partial_\theta \psi_i|\psi_j\rangle + p_j \langle\psi_i|\partial_\theta \psi_j\rangle \\
&= \partial_\theta p_i \delta_{ij} + (p_j - p_i) \langle\psi_i|\partial_\theta \psi_j\rangle\ ,
\end{aligned} \tag{2.23}$$

where we have used $\langle\partial_\theta \psi_i|\psi_j\rangle = -\langle\psi_i|\partial_\theta \psi_j\rangle$. Also, we see that for i and j such that $1 \leq i \leq r$ and $r < j \leq N$, $(\partial_\theta \rho_\theta)_{ij} = -p_i \langle\psi_i|\partial_\theta \psi_j\rangle$. Substituting Eq. (2.23) in Eq. (2.22), we found

$$I(\rho_\theta\,;\,\theta) = \sum_{i=1}^{r} \frac{1}{p_i} (\partial_\theta p_i)^2 + \sum_{i=1}^{r}\sum_{j=1}^{N} \frac{4p_i\,(p_i - p_j)^2}{(p_i + p_j)^2} \left|\langle\psi_i|\partial_\theta \psi_j\rangle\right|^2\ . \tag{2.24}$$

The above expression can be rewritten, using $\sum_{j=1}^{N} = \sum_{j=1}^{r} + \sum_{j=r+1}^{N}$, as

$$I(\rho_\theta\,;\,\theta) = \sum_{i=1}^{r} \frac{1}{p_i} (\partial_\theta p_i)^2 + I_1 + I_2\ , \tag{2.25}$$

with I_1 and I_2 defined with

$$I_1 = \sum_{i,j=1}^{r} \frac{4p_i (p_i - p_j)^2}{(p_i + p_j)^2} \left|\langle\psi_i|\partial_\theta \psi_j\rangle\right|^2\ , \tag{2.26}$$

$$I_2 = \sum_{i=1}^{r}\sum_{j=r+1}^{N} 4p_i \left|\langle\psi_i|\partial_\theta \psi_j\rangle\right|^2\ . \tag{2.27}$$

From the closure relation, we can found $\sum_{k=r+1}^{N} |\psi_k\rangle \langle\psi_k| = \mathbb{1} - \sum_{k=1}^{r} |\psi_k\rangle \langle\psi_k|$ and insert it in the expression of I_2 to obtain

$$I_2 = \sum_{i=1}^{r} 4p_i \langle\partial_\theta\psi_i|\partial_\theta\psi_i\rangle - \sum_{i,j=1}^{r} 4p_i |\langle\psi_j|\partial_\theta\psi_i\rangle|^2 \ . \tag{2.28}$$

We can now put everything together and rewrite the QFI as

$$I(\rho_\theta\,;\,\theta) = \sum_{i=1}^{r} \frac{1}{p_i} (\partial_\theta p_i)^2 + \sum_{i=1}^{r} 4p_i \langle\partial_\theta\psi_i|\partial_\theta\psi_j\rangle - \sum_{i,j=1}^{r} \frac{8p_ip_j}{p_i+p_j} |\langle\psi_i|\partial_\theta\psi_j\rangle|^2 \ . \tag{2.29}$$

If one can access to the eigenvalues and eigenvectors of the density matrix, this expression become a very easy way to compute the QFI and can therefore be added in the Table 2.1.

From this equation, we see that all the information contained in ρ_θ does not depend on the eigenvalues and eigenvectors out of the support of ρ_θ. Moreover, it is natural to treat the first term of the above equation as the classical contribution of QFI. Then the second and third terms should be treated as the quantum contribution. So the QFI can be separate in two part, namely,

$$I(\rho_\theta\,;\,\theta) = I_c + I_q \ , \tag{2.30}$$

where the classical contribution is

$$I_c = \sum_{i=1}^{r} \frac{1}{p_i} (\partial_\theta p_i)^2 \tag{2.31}$$

and the quantum contribution reads

$$I_q = \sum_{i=1}^{r} 4p_i \langle\partial_\theta\psi_i|\partial_\theta\psi_j\rangle - \sum_{i,j=1}^{r} \frac{8p_ip_j}{p_i+p_j} |\langle\psi_i|\partial_\theta\psi_j\rangle|^2 \ . \tag{2.32}$$

Lyapunov representation

The Eq. (2.29) is quite elegant and useful because of its simplicity. But sometimes one does not have the possibility to diagonalize the density operator ρ_θ, as for example when the density operator lives in an infinite dimension space. Lyapunov representation is another method to obtain the SLD. It has been shown to be a very clever way of computing the SLD mainly when the eigenvalues and eigenvectors of the density operator are difficult to obtain [30, 33]. In this section, we will briefly derive the method of Liu *et. al* in [34].

In order to solve Eq. (2.4), which is a special form of Lyapunov equation [35], we start by constructing the useful function

$$f(s) = e^{-\rho_\theta s} L_{\rho_\theta} e^{-\rho_\theta s} \ , \tag{2.33}$$

which satisfies $f(0) = L_{\rho_\theta}$. Immediately, we see that $\partial_s f(s) = -2e^{-\rho_\theta s}(\partial_\theta\rho_\theta)\, e^{-\rho_\theta s}$. By integrating both sides, we obtain

$$f(\infty) - f(0) = -2\int_0^\infty \mathrm{d}s\ e^{-\rho_\theta s}(\partial_\theta\rho_\theta)\, e^{-\rho_\theta s} \ . \tag{2.34}$$

When the rank of ρ_θ is equal to the dimension of the space, $e^{-\rho_\theta s} \to 0$ as $s \to \infty$. This implies that $f(\infty) = 0$ and thus the SLD can be written as

$$L_{\rho_\theta} = 2\int_0^\infty \mathrm{d}s\ e^{-\rho_\theta s}(\partial_\theta\rho_\theta)\, e^{-\rho_\theta s} \ . \tag{2.35}$$

This equation has the advantage to be basis-independent. As for the eigenspace expansion, this representation is not easy to calculate but it might be very useful in some scenarios.

One assumption to obtain Eq. (2.35) was that ρ_θ is a full-rank operator. Unfortunately, this is not true in general. For example, when the density matrix is of rank r and the dimension of the space is N, $e^{-\rho_\theta s} \to \mathrm{diag}\,(0_r, \mathbb{1}_{N-r})$ as $s \to \infty$, with 0_r the r–dimensional zero matrix and $\mathbb{1}_{N-r}$ the $(N-r)$–dimensional identity matrix. Using the hermiticity of L_{ρ_θ}, we can separate the SLD operator into four blocks as

$$L_{\rho_\theta} = \begin{pmatrix} A_r & B_{N-r,r} \\ B_{N-r,r}^\dagger & C_{N-r} \end{pmatrix}. \tag{2.36}$$

One can see that $f(\infty) = \mathrm{diag}\,(0_r, C_{N-r})$. On the right-hand side of Eq. (2.34) we see that, in the eigenbasis of ρ_θ, $e^{-\rho_\theta s}$ is block diagonal. Moreover, the matrix elements $(\partial_\theta \rho_\theta)_{ij}$ vanish for $i, j > r$ [36]. After integration, the matrix element keeps vanishing for $i, j \in [N-r, N]$, which means that C_{N-r} is not involved in Eq. (2.34). Therefore, Eq. (2.35) is still valid, even if ρ_θ is not full-rank.

Thus, we can insert Eq. (2.35) in the QFI equation and get

$$I(\rho_\theta\,;\,\theta) = 2\int_0^\infty \mathrm{d}s\,\mathrm{Tr}\left[\partial_\theta\rho_\theta e^{-\rho_\theta s}\partial_\theta\rho_\theta e^{-\rho_\theta s}\right], \tag{2.37}$$

where we see clearly that this expression is basis independent. Since this is a very useful expression of the QFI, we will add it to Table 2.1.

2.2.2 Pure states case

As a special case, we derive the QFI for a pure state $|\psi_\theta\rangle$, which may depend on the parameter θ. We can compute the corresponding QFI using Eq. (2.29). We know that a pure state is a rank-1 state and that the corresponding probability is $p_1 = 1$. We directly see the first term in Eq. (2.29) vanishes because it corresponds to the classical contribution to the QFI and therefore arises from the classical mixing of a mixed state. The last two terms, corresponding to the quantum contribution, can be easily calculated, and one finds the following expression of the QFI

$$I(|\psi_\theta\rangle\,;\,\theta) = 4\left(\langle\partial_\theta\psi_\theta|\partial_\theta\psi_\theta\rangle - |\langle\psi_\theta|\partial_\theta\psi_\theta\rangle|^2\right). \tag{2.38}$$

We can also add this expression into the Table 2.1.

2.2.3 Additivity of the QFI

Theorem 2.3 (Additivity of the QFI)**.** *Suppose that we have two families of states* $\{\rho_{1,\theta}\}$ *and* $\{\rho_{2,\theta}\}$*. Then, we have*

$$I(\rho_{1,\theta}\otimes\rho_{2,\theta}\,;\,\theta) = I(\rho_{1,\theta}\,;\,\theta) + I(\rho_{2,\theta}\,;\,\theta). \tag{2.39}$$

A proof can be found in [37]. The additivity of the QFI implies that if we take N copies of a state ρ_θ, resulting in the state $\rho_\theta^{\otimes N}$, the corresponding QFI is

$$I(\rho_\theta^{\otimes N}\,;\,\theta) = NI(\rho_\theta\,;\,\theta). \tag{2.40}$$

2.2.4 Convexity of the QFI

Theorem 2.4 (Convexity of the QFI)**.** *Let* $\{\rho_{1,\theta}\}$ *and* $\{\rho_{2,\theta}\}$ *be two families of quantum states parametrized by* θ*. Then, for* $0 \leq \lambda \leq 1$ *we have*

$$I(\lambda\rho_{1,\theta} + (1-\lambda)\rho_{2,\theta}); \theta) \leq \lambda I(\rho_{1,\theta}) + (1-\lambda) I(\rho_{2,\theta}; \theta). \tag{2.41}$$

A. Fujiwara gives a proof of the following theorem in [38]. Intuitively, one understands that a mixture of states can only decrease or at best maintain the QFI. At first glance, it seems natural to think that mixed states are therefore not desirable in an estimation protocol.

2.2.5 A geometrical interpretation of the QFI

If we want to give a geometrical interpretation of the QFI, we need to develop a geometric framework for describing the space of quantum states. We first want to define a distance between two states. Let us introduce the Bures metric, defined as the infinitesimal distance between density matrices [39],

$$\mathrm{d}s^2(\rho, \rho + \mathrm{d}\rho) = \frac{1}{2} \operatorname{Tr}\left[\mathrm{d}\rho G\right], \tag{2.42}$$

where G is implicitly determined by a particular form of the continuous Lyapunov equation, $\mathrm{d}\rho = G\rho + \rho G$. The Bures distance is defined as the finite version of the Bures metric and can be expressed as [40]

$$D_B^2(\rho_1, \rho_2) = 2\left(1 - \sqrt{\mathcal{F}(\rho_1, \rho_2)}\right), \tag{2.43}$$

where $\mathcal{F}(\rho_1, \rho_2) = \operatorname{Tr}\left[\sqrt{\sqrt{\rho_1}\rho_2\sqrt{\rho_1}}\right]^2$ is the fidelity between ρ_1 and ρ_2 [41]. If we consider pure states only, the Bures distance reduces to the Fubini-Study metric [39]. We can show that the Bures distance is, up to second order terms in t, equal to

$$D_B^2(\rho, \rho + \mathrm{d}\rho) = \frac{1}{2} \sum_{i,k} \frac{|\mathrm{d}\rho_{ik}|^2}{p_i + p_k}, \tag{2.44}$$

with $\mathrm{d}\rho_{ik} = \langle\psi_i|\mathrm{d}\rho|\psi_j\rangle$, where $|\psi_j\rangle$ is a eigenvector of ρ associated with the probability p_j, and $\mathrm{d}\rho$ is the tangent vector. Equation (2.44) is the closed expression for the Bures metric. The proof of this result is derived in the Appendix C.

If we consider the case where ρ_θ is explicitly parametrized by the estimation parameter θ, the tangent vector $\mathrm{d}\rho$ is equal to $\mathrm{d}\theta\frac{\mathrm{d}\rho_\theta}{\mathrm{d}\theta}$. We thus obtain

$$D_B^2(\rho, \rho + \mathrm{d}\rho) = D_B^2(\rho_\theta, \rho_{\theta+\mathrm{d}\theta}) \tag{2.45}$$

and, consequently, $\mathrm{d}\rho_{ik} = \mathrm{d}\theta \langle\psi_I|\frac{\mathrm{d}\rho_\theta}{\mathrm{d}\theta}|\psi_k\rangle$, which gives

$$D_B^2(\rho_\theta, \rho_{\theta+\mathrm{d}\theta}) = \sum_{i,k} \frac{p_k}{(p_k + p_i)^2} \left|\mathrm{d}\theta \langle\psi_i|\frac{\mathrm{d}\rho_\theta}{\mathrm{d}\theta}|\psi_k\rangle\right|^2, \tag{2.46}$$

which is, up to a prefactor, the same expression as Eq. (2.22). Eventually, we found that that the QFI is equal to four times the Bures distance

$$I(\rho_\theta\,;\,\theta) = 4\frac{D_B^2(\rho_\theta, \rho_{\theta+\mathrm{d}\theta})}{\mathrm{d}\theta^2} = 8\frac{\left(1 - \sqrt{\mathcal{F}(\rho_\theta, \rho_{\theta+\mathrm{d}\theta})}\right)}{\mathrm{d}\theta^2}, \tag{2.47}$$

where we used Eq. (2.43) for the last equality.

Intuitively, the larger the distance between the states ρ_θ and $\rho_{\theta+\mathrm{d}\theta}$ for a given variation $\mathrm{d}\theta$, the more sensitive the system is to variations in the parameter θ, and then, the higher QFI. Since this provides an intuitive geometric interpretation of the QFI, we include it in Table 2.1.

2.3 Quantum multi-parameter estimation

As in Section 1.4, sometimes we are interested in estimating not a single parameter, but rather multiple parameters at the same time. Its corresponding quantum version of the multi-parameter estimation is the following.

We consider a quantum state $\rho_{\boldsymbol{\theta}}$ parametrised by a vector parameter $\boldsymbol{\theta} = \{\theta_i\}$. The goal is to estimate the vector parameter with $\hat{\boldsymbol{\theta}}_{\text{est}}$. Therefore, the quantum version of the Cramér-Rao theorem can be expressed as

$$\text{Cov}[\rho_{\boldsymbol{\theta}}, \hat{\boldsymbol{\theta}}_{\text{est}}] \geq m^{-1}\mathbf{I}^{-1}(\rho_{\boldsymbol{\theta}}, \boldsymbol{\theta}) \ , \tag{2.48}$$

with m the number of copies of the state, $\mathbf{I}(\rho_{\boldsymbol{\theta}}, \boldsymbol{\theta})$ the Quantum Fisher Information matrix (QFIM) defined by its components [42]

$$(\mathbf{I}(\rho_{\boldsymbol{\theta}}, \boldsymbol{\theta}))_{\mu,\nu} = \text{Tr}\left[L_\mu \partial_\nu \rho_{\boldsymbol{\theta}}\right] \ . \tag{2.49}$$

The inequality in Eq.(2.48) should be understood as stating that $\text{Cov}[\rho_{\boldsymbol{\theta}}, \hat{\boldsymbol{\theta}}\text{est}] - m^{-1}\mathbf{I}^{-1}(\rho\boldsymbol{\theta}, \boldsymbol{\theta})$ is a positive semi-definite matrix. The same interpretation applies for the Fisher information matrix in Sec.1.4. We can derive a more convenient expression of the QFIM using the same derivation as in Section 2.2.1 and obtain

$$(\mathbf{I}(\rho_{\boldsymbol{\theta}}, \boldsymbol{\theta}))_{\mu,\nu} = 2\sum_{i,j=1}^{d} \frac{\text{Re}\left(\langle\lambda_i|\partial_\mu\rho_{\boldsymbol{\theta}}|\lambda_j\rangle\,\langle\lambda_j|\partial_\nu\rho_{\boldsymbol{\theta}}|\lambda_i\rangle\right)}{\lambda_i + \lambda_j} \ . \tag{2.50}$$

The last equation still work if $\rho_{\boldsymbol{\theta}}$ is not full-rank if we restrict the summation indices to indices for which $\lambda_i + \lambda_j > 0$.

For a practical example of a multi-parameter estimation, see Sec. 3.3.3.

Chapter 3

Quantum Metrology

In Chapter 1, we introduced parameter estimation theory. Then, in Chapter 2, we applied the theory to the quantum world. This led us to the definition of the celebrated Quantum Fisher Information, the quantity that enables us to calculate how much useful information can be extracted from a probe state ρ_θ related to the parameter θ to be estimated. In this chapter, we will provide more details about the protocols and resources used in quantum metrology. Then, we will briefly introduce a more detailed definition of the Standard Quantum Limit and the Heisenberg Limit. We will conclude by presenting well-known quantum metrology protocols and quantum-enhanced measurement schemes.

3.1 Protocols and resources

3.1.1 Protocols

As we saw in the previous chapter, we can quantify how much information a state can carry about an unknown parameter. The QFI is the quantity that lets us compare one state to another and give a quantitative argument on which gives the best estimate of a parameter. Intuitively, for a parameter θ and two states ρ_θ and ρ'_θ, the one with the highest QFI must be chosen in a protocol to achieve the highest precision. However, if we stop our analysis here, we miss half of the interpretation of the QFI. Indeed, it not only depends on the state itself, but also on its evolution. As shown in row 6 of Table 2.1, the QFI also depends on the generator of the dynamics (here the Hamiltonian) on which the evolution of the state depends.

A general quantum parameter estimation protocol is illustrated in Fig. 3.1 and can be divided into four steps:

(i) Prepare the initial probe state ρ.

(ii) Encode the parameter in the state through some quantum evolution.

(iii) Measure (via POVM $\{M_\xi\}$).

(iv) Estimate the unknown parameter.

This is a very general scheme and needs refinements. First, we can distinguish two clearly distinct cases. As we saw in the two previous chapters, an estimation procedure requires an m-sample. Therefore, we must repeat the experiment several times, which allows us to consider a significant modification of the protocol shown in Fig. 3.1. Here we develop two manners for obtaining m-samples.

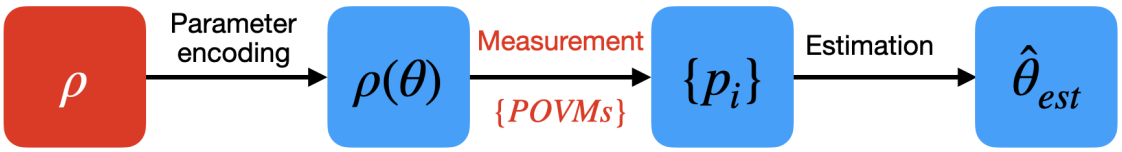

Figure 3.1: Diagram of a general quantum parameter estimation protocol. The red box with the initial state indicates that this is where we generally act to improve the precision of a protocol. We could also act on the measurement by choosing what to measure, *i.e.*, choosing the set of POVMs

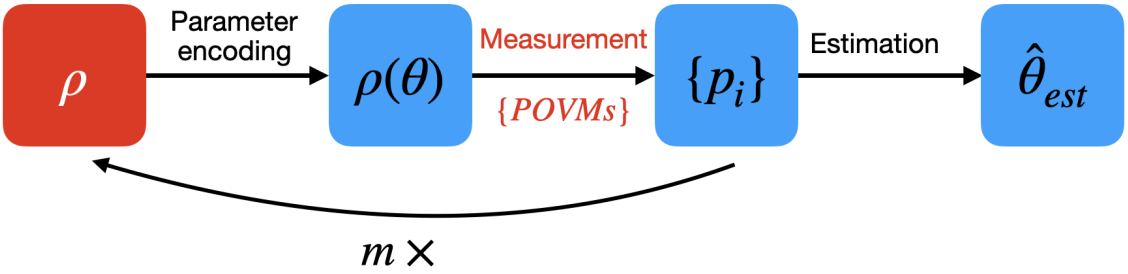

Figure 3.2: Diagram of m repetitions of the basic protocol shown in Fig. 3.1.

An obvious way to achieve a large number of samples is to repeat the procedure m times. This is equivalent to adding a step (iii') between the measurement and the estimation

(iii') Repeat steps (i), (ii) and (iii) m times.

This leads to Fig. 3.2, a modified version of Fig. 3.1. This seems obvious, but this is possible only if the parameter stays the same between two repetitions.

For example, if we try to estimate the value of a magnetic field using a fixed protocol with a duration of τ, the field must remain constant for a duration of at least m times τ. Maximizing the number of repetitions may seem like the most straightforward way to improve the parameter estimate. However, this is not necessarily true, as it does not take into account the quantum behaviour of our system. Instead of using a single system in a state ρ, we should consider a collection of N copies of the system in a global state ρ_N. Consequently, one iteration of the protocol would produce N measurement results, corresponding to the N subsystems being measured. When combined with m repetitions of the protocol, this leads to the procedure illustrated in Fig. 3.3. The collection of systems can be prepared in a separable or an entangled global state ρ_N. The number of repetitions should also be taken into account. In this context, it is also important to consider the possibility of collective measurements. Instead of performing independent measurements on each of the N subsystems, one can perform a joint measurement on the entire N-partite system. Such collective measurements can exploit quantum correlations between the subsystems and, in some cases, enhance parameter estimation precision beyond the achievable one with local measurements. This is particularly relevant when the global state ρ_N is entangled, as collective strategies may allow us to approach or even saturate the quantum Cramér-Rao bound.

3.1.2 Resources

If we want to compare quantum metrology protocols, we need to define the resources involved. The first resource is the **number of probes** N. We count only the number of probes used

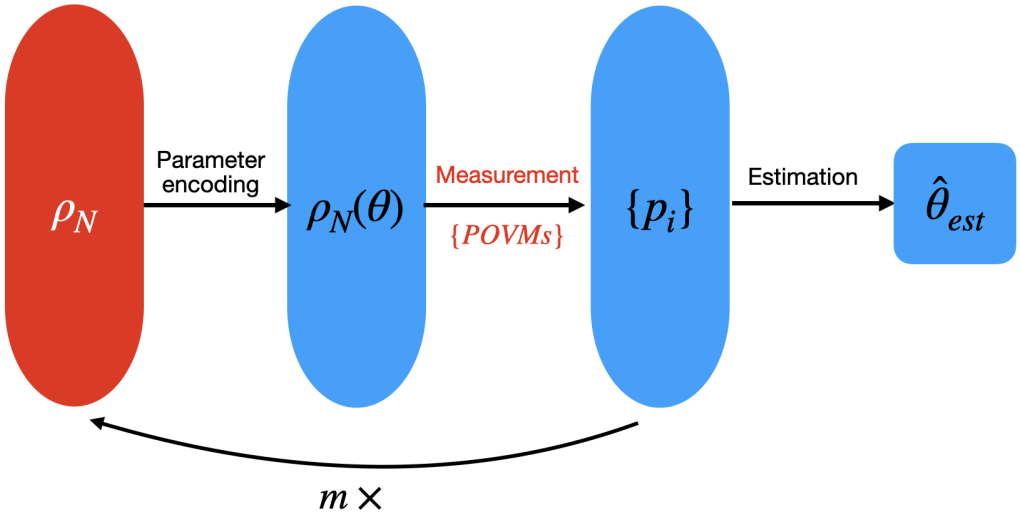

Figure 3.3: Diagram of the final protocol using the quantum behaviour of the system. The input is a collection of states ρ_N (possibly entangled) on which the parameter θ is encoded. A measurement is then performed using POVMs, and this procedure is repeated m times to obtain the estimator $\hat{\theta}_{est}$.

in a single iteration of the protocol. If the system under consideration consists of subsystems, we count the number of subsystems. For a collection of qubits, the number of probes is equal to the number of qubits. Since a spin-j system can be described as a system of $2j$ qubits, the number of probes in such a system is $N = 2j$. The second resource is **time** t. This is the time required to perform one iteration of the protocol. We consider only the evolution time, excluding the time needed for state preparation and post-processing.

3.2 Definition of the SQL and HL

In the section, we will try to define precisely what we mean by the Standard Quantum Limit and the Heisenberg Limit. We follow the presentation of Ref. [24]. In general, SQL and HL are closely linked to how sensitivity scales with a given resource. The key question is which resource should be used to establish a general formalism. A natural choice is the number of probes N, *i.e.*, the number of subsystems. The associated Hilbert space is $\mathcal{H} = \bigotimes_{i=1}^{N} \mathcal{H}_i$. We then consider the Hamiltonian $H(\theta)$ that acts separately on each subsystem

$$H(\theta) = \sum_{i=1}^{N} h_i(\theta) \ , \tag{3.1}$$

where h_i is an abuse of notation used both for the Hamiltonian of the ith particle living in the space $\mathcal{H}_i$, and for the Hamiltonian acting on the ith particle embedded in the full Hilbert space $\mathcal{H}$; the context will make it clear which one is meant. Therefore, the evolution operator is $U_H = e^{-itH(\theta)} = \bigotimes_{i=1}^{N} U_{h,i}$ with $U_{h,i} \stackrel{\text{def}}{=} e^{-ith_i(\theta)}$ where we set $\hbar = 1$.

In a broad sense, four distinct scenarios can be considered (see Fig. 3.4):

- A purely classical approach, where no quantum effects are employed—referred to as the *classical-classical* (CC) strategy;
- A *classical-quantum* (CQ) strategy, in which quantum effects are utilized solely during the measurement phase;

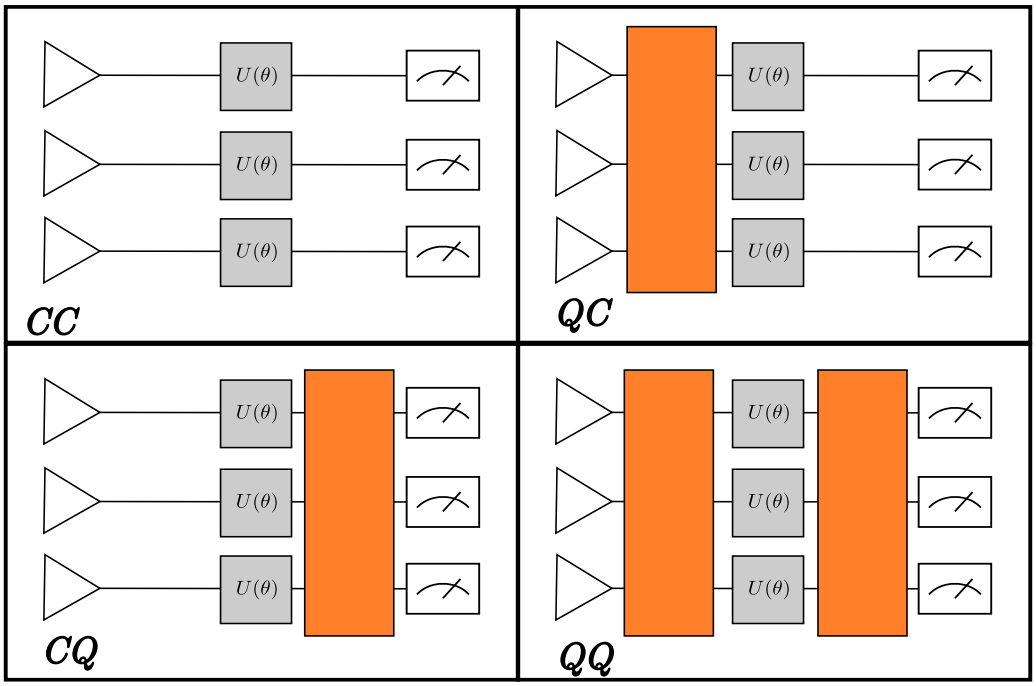

Figure 3.4: Different strategies for estimating a parameter θ using N probes and a unitary operation $U(\theta)$. Orange boxes indicate unitary evolutions involving multiple probes (capturing quantum effects), with input states represented by triangles and measurements by the symbols on the right. CC strategies use separable input states and separable measurements. CQ strategies use separable input states with general (possibly entangled) measurements. QC strategies involve general (possibly entangled) input states with separable measurements. QQ strategies use general input states and general measurement schemes.

- A *quantum-classical* (QC) strategy, where quantum resources are involved only during the state preparation phase;
- A fully quantum (QQ) protocol, where quantum effects are exploited in both state preparation and measurement phases.

Interestingly, Giovannetti *et al.* showed in [43] that the ultimate precision achievable by CC and CQ strategies is limited by the standard quantum limit (SQL), scaling as $1/\sqrt{N}$, while QC and QQ strategies can reach the Heisenberg limit (HL), scaling as $1/N$. This implies that quantum resources such as entanglement or squeezing are beneficial at the state preparation stage but offer no advantage when used solely at the measurement stage.

3.2.1 Standard Quantum Limit

In order to define the SQL, we consider a Hamiltonian of the form given by Eq. (3.1). Thus, we do not need to restrict the set of possible POVMs, which implies that we can use the QFI. We consider the pure initial state

$$|\psi\rangle = \bigotimes_{i=1}^{N} |\phi\rangle_i \,, \tag{3.2}$$

which evolution is given by

$$|\psi(t)\rangle = \bigotimes_{i=1}^{N} U_{h,i} \, |\phi\rangle_i \ . \tag{3.3}$$

Thanks to the additivity of the QFI, we can show that the QFI has the following form

$$I(|\psi(t)\rangle\,;\theta) = Nt^2\,4\mathrm{Var}[\mathscr{H}_i, |\phi\rangle], \tag{3.4}$$

with $\mathscr{H}_i \overset{\text{def}}{=} iU_{h,i}^\dagger(\partial_\theta U_{h,i})$ the local generator of the ith subsystem and considering that each subsystem is in the state $|\phi\rangle$. The derivation of this expression can be found in Appendix D. The most important result in Eq. (3.4) is the linear scaling of the QFI with the number of probes. This is what we call the **SQL scaling**, *i.e.*, $I(|\psi(t)\rangle\,;\theta) \propto N$.
We can now maximize the QFI over pure separable states. This is equivalent to maximizing $\mathrm{Var}[\mathscr{H}_i, |\phi\rangle]$ over all possible $|\phi\rangle$. Using Popoviciu's inequality [44], we know that the variance of a random variable X, lying between an upper bound b and a lower bound a, is upper bounded by $(b-a)^2/4$. Therefore, we obtain the inequality

$$\mathrm{Var}[\mathscr{H}_i, |\phi\rangle] \geq \frac{(h_{\max} - h_{\min})^2}{4}, \tag{3.5}$$

where $h_{\max}$ and $h_{\min}$ are the maximal and minimal eigenvalues of $\mathscr{H}_i$, associated with the eigenvectors $|h_{\max}\rangle$ and $|h_{\min}\rangle$, respectively.

To saturate this bound, we consider the superposition of the two extremal eigenvectors

$$|\phi(x)\rangle = \sqrt{x}\,|h_{\max}\rangle + \sqrt{1-x}\,|h_{\min}\rangle\,. \tag{3.6}$$

with $x \in [0,1]$. For this choice of $|\phi(x)\rangle$, the variance is given by

$$\mathrm{Var}[\mathscr{H}_i, |\phi(x)\rangle] = t^2 x(1-x)(h_{\max} - h_{\min})^2. \tag{3.7}$$

Equation (3.7) is maximized for $x = 1/2$. This leads to the corresponding QFI using the optimal separable input state $|\phi(1/2)\rangle^{\otimes N}$

$$I(U_H\,|\phi(1/2)\rangle^{\otimes N}\,;\theta) = Nt^2(h_{\max} - h_{\min})^2\,, \tag{3.8}$$

with $U_h = e^{-itH(\theta)}$ and $H(\theta) = \sum_{i=1}^N h_i(\theta)$.

This is referred to as the **SQL QFI**. We provide a plot of Eq. (3.8) in Fig. 3.5 in order to compare its scaling with the HL scaling.

3.2.2 Heisenberg Limit

The main difference with the SQL is that we do not impose the input state to be separable. Instead, we allow quantum correlations between the subsystems composing the initial state. We can maximize the QFI in the same way as for the SQL. We consider the local generator $\mathscr{H}$ with maximal and minimal eigenvalues $Nh_{\max}$ and $Nh_{\min}$, respectively, corresponding to the eigenvectors $|h_{\max}\rangle^{\otimes N}$ and $|h_{\min}\rangle^{\otimes N}$. We then consider the initial entangled state

$$|\varphi(x)\rangle = \sqrt{x}\,|h_{\max}\rangle^{\otimes N} + \sqrt{1-x}\,|h_{\min}\rangle^{\otimes N}\,. \tag{3.9}$$

Using the same arguments as for the SQL, this leads to the following expression for the QFI

$$I(U_H\,|\varphi(\pi/2)\rangle\,;\theta) = N^2t^2(h_{\max} - h_{\min})^2\,. \tag{3.10}$$

We observe in the last equation that $I(|\psi(t)\rangle\,;\theta) \propto N^2$. This is known as the **HL scaling**. As for the SQL, the QFI in Eq. (3.10) is referred to as the **HL QFI**.

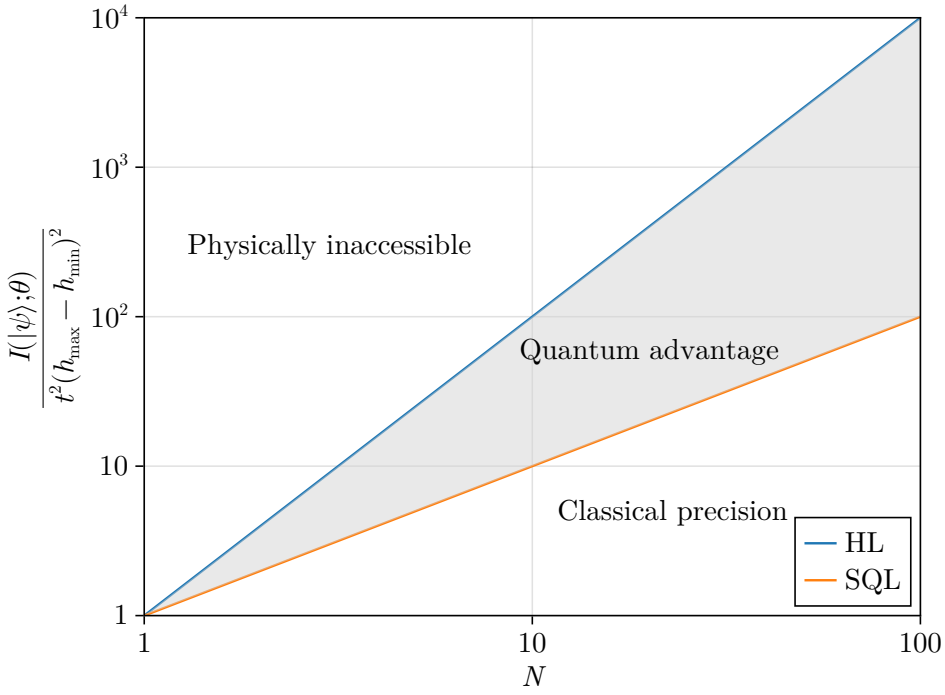

Figure 3.5: Representation of the SQL (orange solid line) and HL (blue solid line) as a function of the number of probes N. The states for the SQL and HL are, respectively, $|\psi\rangle = U_H \, |\phi(\pi/2)\rangle^{\otimes N}$ and $|\psi\rangle = U_h \, |\varphi(\pi/2)\rangle$.

3.3 Quantum enhanced measurements

In this section, we will review well-studied protocols for quantum-enhanced measurements. We will study the well-known case of the Mach-Zehnder interferometer, as well as the advantages of squeezing, and finally an example of a protocol for measuring multiple parameters of a magnetic field.

3.3.1 Mach-Zehnder interferometer

The first example is the Mach-Zehnder interferometer (MZI). As mentioned at the beginning of the section, we will only study the lossless MZI. The estimation of the optical phase generated by some external cause using an MZI is an important topic in multiple areas of research [45, 46, 47, 48, 49]. A schematic representation of the MZI is provided in Fig. 3.6a. It consists of two 50:50 beam splitters (BS), two mirrors, a phase-shifting element θ, and a detector. A laser source injects coherent light into the system, where the first beam splitter divides the incoming beam into two paths. One path travels through the phase shifting element, which introduces a phase difference θ, while the other path remains unchanged. Both beams are then reflected by mirrors and recombined in the second beam splitter. Depending on the relative phase difference, interference occurs, influencing the intensity at the output ports. The detector measures the resulting intensity, allowing precise phase estimation. Additionally, the presence of a vacuum port at the first beam splitter highlights the quantum nature of the system, as it introduces vacuum fluctuations that can affect measurement outcomes in certain quantum optics experiments. The protocol can be simulated by the circuit in Fig. 3.6b.

Here, we will focus on the estimation of a small phase shift $\theta \ll 1$. We consider a system involving N particles and assume that all their degrees of freedom are restricted to only two

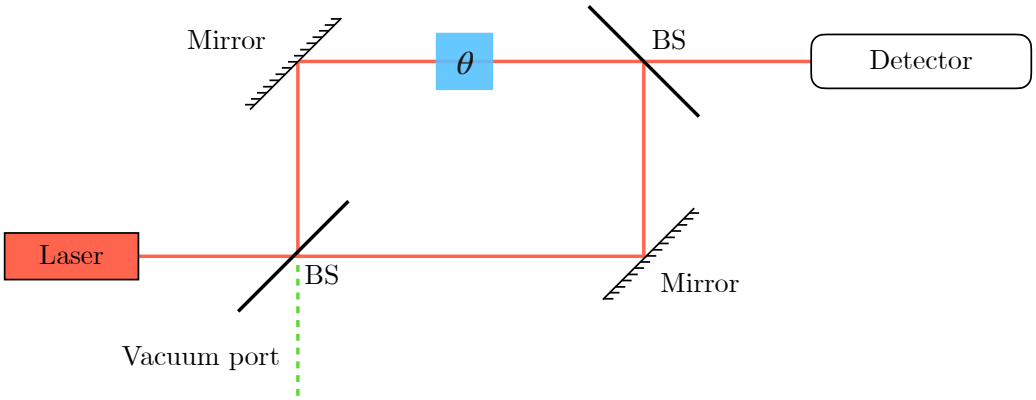

(a) Schematic representation of a lossless Mach-Zehnder interferometer. The BSs are 50:50 beam splitters.

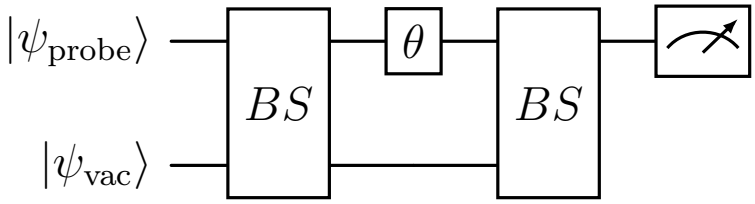

(b) Quantum circuit simulating a lossless MZI.

Figure 3.6: Comparison between the physical setup (top) and its quantum circuit representation (bottom) of a Mach-Zehnder interferometer.

modes, identified as $|a\rangle$ and $|b\rangle$. By defining mode $|a\rangle$ as spin-up and mode $|b\rangle$ as spin-down, each of the N particles can be described as an effective spin-1/2 particle, *i.e.*, a qubit. A pure qubit state can be expressed as

$$|\vartheta, \varphi\rangle = \cos(\vartheta/2)\,|a\rangle + e^{i\varphi/2}\sin(\vartheta/2)\,|b\rangle\,, \tag{3.11}$$

with $0 \leq \vartheta \leq \pi$ and $0 \leq \varphi \leq 2\pi$.

For an ensemble of N indistinguishable qubits, we introduce the total angular momentum operator $\mathbf{J} = (J_x, J_y, J_z)$, defined as

$$J_x = \frac{1}{2}\sum_{k=1}^{N}\sigma_x^{(k)}\,, \qquad J_y = \frac{1}{2}\sum_{k=1}^{N}\sigma_y^{(k)}\,, \qquad J_z = \frac{1}{2}\sum_{k=1}^{N}\sigma_z^{(k)}\,, \tag{3.12}$$

where $\sigma_i^{(k)}$ is the ith Pauli operator acting on the kth particle. Alternatively, the total angular momentum operator can be expressed as

$$J_x = \frac{a^\dagger b + b^\dagger a}{2}\,, \qquad J_y = \frac{a^\dagger b - b^\dagger a}{2i}\,, \qquad J_z = \frac{a^\dagger a - b^\dagger b}{2}, \tag{3.13}$$

where $a^\dagger$ and $b^\dagger$ are the creation operator for the mode $|a\rangle$ and $|b\rangle$, respectively.

Any rotation of a qubit (*i.e.*, any unitary transformation) is expressible as $e^{-i\theta\sigma_{\mathbf{n}}/2}$ where $\mathbf{n}$ is the rotation axis and θ the rotation angle. For an ensemble of N qubits and when each qubit undergoes the same rotation about the same axis by the same angle, the resulting collective

rotation transformation is given by

$$\bigotimes_{k=1}^{N} e^{-i\theta\sigma_{\mathbf{n}}^{(k)}/2} = e^{-i\theta J_{\mathbf{n}}} \ . \tag{3.14}$$

In this framework, the beam splitter and the phase-shifting element in Fig. 3.6b can be modeled using the unitary transformations $e^{-i(\pi/2)J_x}$ and $e^{-i\theta J_z}$. One can show that the circuit is equivalent to a single transformation $e^{-i\theta J_y}$. The goal is now to find a state that maximize the QFI for a small rotation angle θ around the y-axis.

Let us consider two different input states: A coherent state $|\vartheta, \varphi, N\rangle$ and a NOON state $|\mathrm{NOON}\rangle$. The coherent states are constructed as the tensor product of N pure qubit states all pointing in the same mean spin direction $\mathbf{s} = \{\sin\vartheta\cos\varphi, \sin\vartheta\sin\varphi, \cos\vartheta\}$ [16, 50]

$$|\vartheta, \varphi, N\rangle = \bigotimes_{k=1}^{N} |\vartheta, \varphi\rangle_k = \bigotimes_{k=1}^{N} \left[\cos\frac{\vartheta}{2}|a\rangle_k + e^{i\varphi}\sin\frac{\vartheta}{2}|b\rangle_k\right] \ . \tag{3.15}$$

The NOON state is given by [16]

$$|\mathrm{NOON}\rangle = \frac{(|0, 0, N\rangle + |\pi, 0, N\rangle)}{\sqrt{2}} \ . \tag{3.16}$$

This corresponds to a superposition of a state with all particles in mode a, and another with all particles in mode b. In order to compare the performance of the two states in an estimation protocol given by the MZI, we compute the Bures distance between the initial state $|\vartheta, \varphi, N\rangle$ and the rotated state $e^{-i\theta J_{\mathbf{n}}}|\vartheta, \varphi, N\rangle$, as is done in [16]. For our calculation, we will consider $J_{\mathbf{n}} = J_y$, corresponding to the total transformation of a MZI. The same calculation is performed for the NOON state. Using Eq. (2.43), we finally obtain

$$\begin{aligned} D_B^2\left(|\vartheta, \varphi, N\rangle, e^{-i\theta J_y}|\vartheta, \varphi, N\rangle\right) &= 2 - 2\cos^N(\theta/2) \\ &\approx \frac{N\theta^2}{4} + \mathcal{O}(\theta^4) \ , \end{aligned} \tag{3.17}$$

where the last equality is valid for small value of $\theta \ll 1$. With the NOON state, the Bures distance squared is then

$$\begin{aligned} D_B^2\left(|\mathrm{NOON}\rangle, e^{-i\theta J_y}|\mathrm{NOON}\rangle\right) &= 2 - 2\cos(N\theta/2) \\ &= \frac{N^2\theta^2}{4} + \mathcal{O}(\theta^4) \ , \end{aligned} \tag{3.18}$$

where, as for the coherent state, the last equality holds for $\theta \ll 1$. Using Eq. (2.47), we finally obtain

$$I(|\vartheta, \varphi, N\rangle \ ; \theta) = N, \tag{3.19}$$

$$I(|\mathrm{NOON}\rangle \ ; \theta) = N^2. \tag{3.20}$$

From Eq. (3.19), we directly conclude that the coherent state reaches the SQL scaling and the SQL QFI. On the other hand, from Eq. (3.20), we see that the NOON state is far more informative than the coherent state, as it reaches the HL QFI and scaling. Indeed, let us imagine a rotation about the y-axis of both states. The overlap between the initial state and the rotated state, which is directly related to the fidelity between these two states, appears to be much smaller for the NOON state than for the coherent state. Therefore, it is easy to understand that the smaller the overlap is, the better the information we can extract from it, and thus the greater the QFI is.

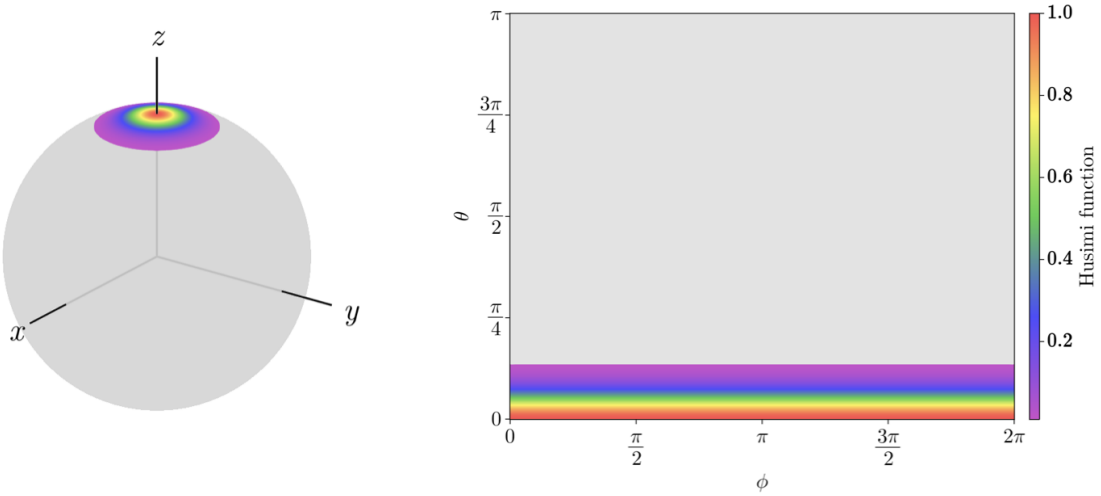

Figure 3.7: Husimi distribution of the coherent sate $|\vartheta, \varphi, N\rangle = |0, 0, 100\rangle$. The values of the Husimi function lower than 0.01 are displayed in gray.

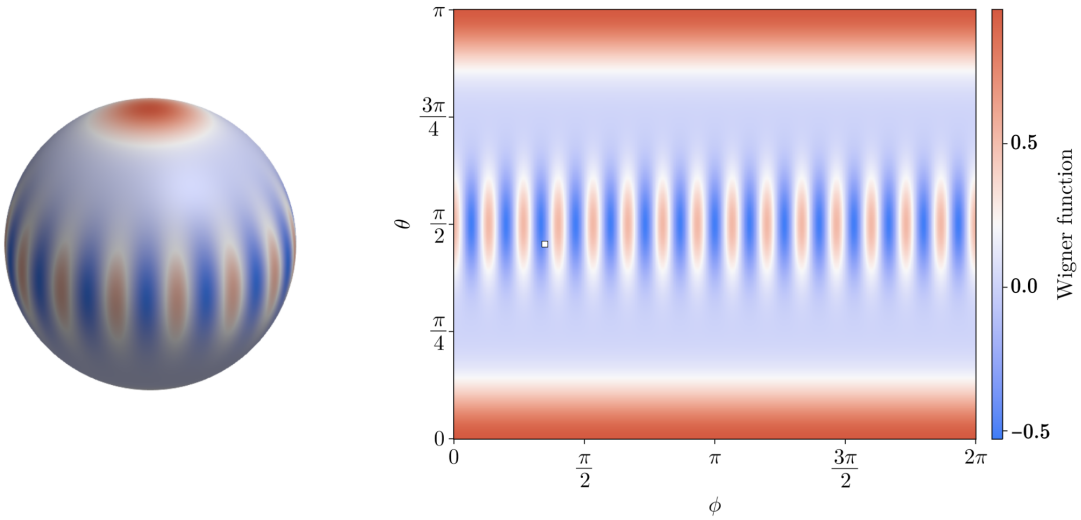

Figure 3.8: Wigner distribution of the state $|\text{NOON}\rangle$ for $N = 15$.

3.3.2 Spin squeezing

Another well-known example of a state that exceeds the SQL is a spin-squeezed state. This type of states exhibits reduced spin variance along a specific direction while increasing variance in the orthogonal direction. They are among the most effective states for demonstrating large-scale quantum entanglement and outperforming the SQL in interferometry.

We consider the unitary rotation of a state on the Bloch sphere about an axis $\mathbf{n}$ perpendicular to the mean spin direction $\mathbf{s}$. Pezzè *et al.* showed that the phase sensitivity of an interferometer is given by [16]

$$\Delta\theta = \frac{\xi_{\mathrm{R}}}{\sqrt{mN}} \,, \tag{3.21}$$

where

$$\xi_{\mathrm{R}}^2 = \frac{N(\Delta J_\perp)^2}{\langle J_{\mathbf{s}}\rangle^2} \,, \tag{3.22}$$

is the spin-squeezing parameter introduced by Wineland *et al.* [17, 18] and $\mathbf{s} = \frac{(\langle J_x\rangle,\langle J_y\rangle,\langle J_z\rangle)}{|\langle \mathbf{J}\rangle|}$ is the mean spin direction. In particular for a coherent state $\mathbf{s} = (\sin\vartheta\cos\phi, \sin\vartheta\sin\phi, \cos\vartheta)$. Here, $\perp$ denotes the orthogonal direction of both $\mathbf{s}$ and $\mathbf{n}$, and m is the number of repetitions. If $\xi_{\mathrm{R}}^2 < 1$, the state is said to be metrologically spin-squeezed along the $\perp$ axis [17, 18] and can be used to surpass the SQL (*i.e.*, $\Delta\theta < \frac{1}{\sqrt{mN}}$). An example of a spin-squeezed state as represented by its Husimi distribution is shown in Fig. 3.9.

Sørensen and Mølmer showed in [51] that $\xi_{\mathrm{R}} < 1$ is a sufficient condition for useful particle entanglement in metrology. They also demonstrated that the degree of spin squeezing is related to metrologically useful k-particle entanglement. Specifically, for a given spin length, smaller values of ξ_{R} can be achieved by increasing the entanglement depth k. One can show the following condition

$$\frac{N}{I(\rho,\theta)} \leq \xi_{\mathrm{R}}^2 \,. \tag{3.23}$$

Therefore, if a state is spin-squeezed with $\xi_{\mathrm{R}}^2 < 1$, it surpasses the SQL, satisfying $I(\rho,\theta) > N$. However, it is important to note that, while a spin-squeezed state is metrologically useful, not all metrologically useful states are spin-squeezed. For example, the NOON states discussed in the previous section are metrologically useful but are not spin-squeezed states.

3.3.3 Estimation of a magnetic field

The estimation of an unknown magnetic field is an important application of quantum metrology. Many physical systems have been used as quantum magnetometers [52, 53, 54, 55].

First, we consider a single probe state (without ancilla). We represent the magnetic field as a vector $\mathbf{B} = B(\cos\theta\cos\phi, \cos\theta\sin\phi, \sin\phi)$, where B is the amplitude, and θ and ϕ define the direction of the field. We are now in the context of estimating three unknown parameters: B, θ, and ϕ. Therefore we need to use multiparameter estimation theory; see Sec. 2.3. In the case where one angle is known, for example, ϕ, the estimation of the whole field becomes a two-parameter estimation problem. Let us consider a simple case where the probe is a single-spin system and the interaction is governed by the Hamiltonian [56]

$$H = -B\,\mathbf{n}_0 \cdot \boldsymbol{\sigma}, \tag{3.24}$$

with $\mathbf{n}_0 = (\cos\theta, 0, \sin\theta)$ and $\boldsymbol{\sigma} = (\sigma_x, \sigma_y, \sigma_z)$.

We need to specify what the resources are, and what the SQL and HL refer to. First, we will not consider the time cost of measurement and state preparation—this is equivalent to

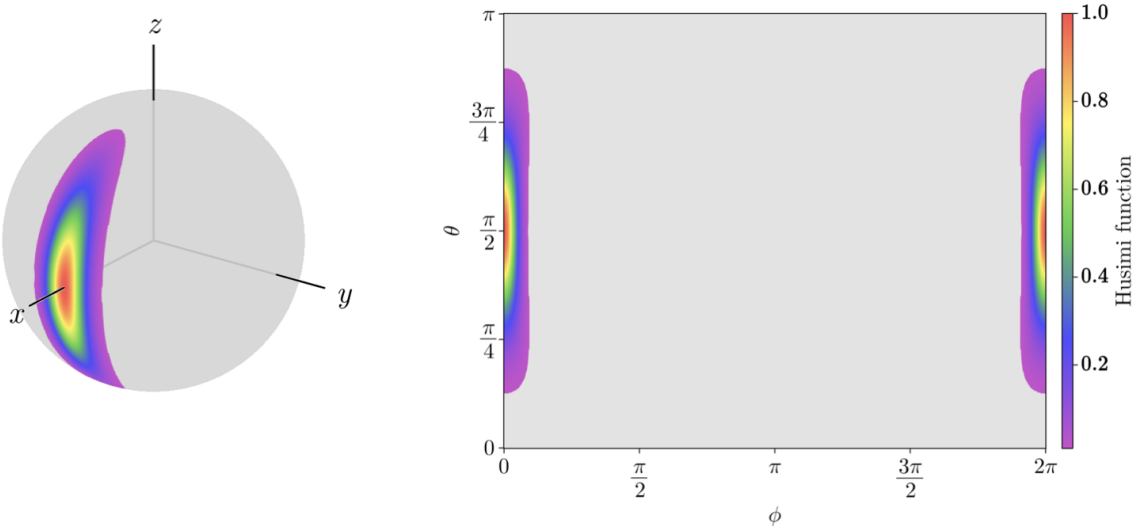

Figure 3.9: Husimi distribution of a squeezed spin state with $\xi_R^2 = 0.1$. The values of the Husimi function lower than 0.01 are displayed in gray.

assuming that both processes are instantaneous. Consequently, the only relevant time is the duration during which the probe state remains in the region where the magnetic field is present.

Second, in what follows, we consider a setup with one qubit acting as a probe and one qubit serving as an ancilla.

Third, the SQL and HL can be extracted from the Quantum Cramér-Rao Bound for a control-enhanced sequential scheme. The Heisenberg Limit (HL) is given by $4t^2$, and the Standard Quantum Limit (SQL) by $4t$, where t is the time the probe spends in the magnetic field. Mathematical details are provided in [56] and [57].

From this, we directly observe that the HL exhibits a scaling of $\propto t^2$, while the SQL scales as $\propto t$.

Now that we have defined the resources, the SQL, and the HL, we can continue the development. Using Eq. (2.49) and the two local generators $\mathcal{H}_B$ and $\mathcal{H}_\theta$ defined by

$$\mathcal{H}_B = t\,\mathbf{n}_0 \cdot \boldsymbol{\sigma}\ , \tag{3.25}$$

$$\mathcal{H}_\theta = -\frac{1}{2}\sin(Bt)\,\mathbf{n}_1 \cdot \boldsymbol{\sigma} \tag{3.26}$$

where $\mathbf{n}_1 = (\cos(Bt)\sin\theta, \sin(Bt), -\cos(B)\cos\theta)$, the quantum fisher information matrix $\mathbf{I}(\rho_{\boldsymbol{\theta}}; \boldsymbol{\theta})$, with $\boldsymbol{\theta} = (B, \theta, \phi)$ and $\rho_0 = |\psi_0\rangle\langle\psi_0|$, then reads

$$(\mathbf{I}(\rho_{\boldsymbol{\theta}}; \boldsymbol{\theta}))_{\theta,\theta} = \sin^2(Bt)\left[1 - (\mathbf{n}_1 \cdot \mathbf{r})^2\right]\ , \tag{3.27}$$

$$(\mathbf{I}(\rho_{\boldsymbol{\theta}}; \boldsymbol{\theta}))_{B,B} = 4t^2\left[1 - (\mathbf{n}_0 \cdot \mathbf{r})^2\right]\ , \tag{3.28}$$

$$(\mathbf{I}(\rho_{\boldsymbol{\theta}}); \boldsymbol{\theta}))_{B,\theta} = 2t\sin(Bt)(\mathbf{n}_0 \cdot \mathbf{r})(\mathrm{n}_1 \cdot \mathbf{r})\ , \tag{3.29}$$

where $\mathbf{r}$ is the Bloch vector of the probe state. Thus, the maximal value of the parts (θ, θ) and (B, B) of the QFIM can be reached when $\mathbf{r}_{\text{in}}$ is orthogonal to $\mathbf{n}_0$ and $\mathbf{n}_1$. However, due to the following corollary (Section 3.2.2 in [56]),

Corollary. *For a unitary process U with a pure probe state $|\psi_0\rangle$, the necessary and sufficient condition for the attainability of quantum multiparameter Cramér-Rao bound is*

$$\langle\psi_0|\,[\mathcal{H}_a, \mathcal{H}_b]\,|\psi_0\rangle = 0,\ \forall a, b\ . \tag{3.30}$$

with $\mathcal{H}_x = -iU^\dagger(\partial_x U)$ *and* $x = a, b$.

we have to check the value of $\langle\psi_0|\,[\mathcal{H}_\mathcal{B}, \mathcal{H}_\theta]\,|\psi_0\rangle$, where $|\psi_0\rangle$ is the probe state. Therefore we have

$$\langle\psi_0|\,[\mathcal{H}_\mathcal{B}, \mathcal{H}_\theta]\,|\psi_0\rangle = -\sin(Bt)(\mathbf{n}_0 \cdot \mathbf{n}_1) \cdot \boldsymbol{\sigma}, \tag{3.31}$$

which vanishes for $t = \frac{n\pi}{B}$ (with $n = 1, 2, 3, \dots$), allowing us to reach the QCRB. However, we see that Eq. (3.27) then also vanishes. Thus, when one angle is unknown, alternative probe states should be considered.

We can now increase the complexity by considering a system that includes ancilla. Here, we focus on a two-qubit system, where one qubit serves as the probe, while the second acts as an ancilla that does not interact with the field. The corresponding Hamiltonian is given by

$$H = -\mathbf{B} \cdot \boldsymbol{\sigma} \otimes \mathbb{1}. \tag{3.32}$$

The maximal QFIM in the basis $\{B, \theta, \phi\}$ is then [56]

$$\max I(\rho_{\boldsymbol{\theta}}; \boldsymbol{\theta}) = 4 \begin{pmatrix} t^2 & 0 & 0 \\ 0 & \sin^2(Bt) & 0 \\ 0 & 0 & \sin^2(Bt)\cos^2\theta \end{pmatrix}. \tag{3.33}$$

H. Yuan showed that it is possible to achieve this QFIM using any maximally entangled state and the Bell measurement as the optimal measurement [58]. Therefore, one can observe that all three parameters in $\boldsymbol{\theta}$ can be estimated simultaneously. Unfortunately, since the $(\mathbf{I})_{\theta\theta}$ and $(\mathbf{I})_{\phi\phi}$ components of the QFIM are proportional to $\sin^2(Bt)$, letting the system evolve for a longer time does not necessarily lead to better precision for these two parameters.

A strategy to overcome this issue is to introduce an additional control. When evolution is unitary and described by the evolution operator $U(\delta t) = e^{-iH(\mathbf{B})\delta t}$, H. Yuan has shown that performance is significantly improved by applying an reverse evolution operator as a control [58]. After each evolution over a period δt, a control operation is inserted to reverse the evolution as $U^\dagger(\delta t) = e^{iH(\mathbf{B})\delta t}$. The QFIM then takes the form

$$\max I(\rho_{\boldsymbol{\theta}}; \boldsymbol{\theta}) = 4N^2 \begin{pmatrix} (\delta t)^2 & 0 & 0 \\ 0 & \sin^2(B\delta t) & 0 \\ 0 & 0 & \sin^2(B\delta t)\cos^2\theta \end{pmatrix}, \tag{3.34}$$

with N being the number of injected control pulses ($N\delta t = t$). Of course, in practice, the control needs to be applied adaptively as $U^\dagger(\delta t) = e^{iH(\hat{\mathbf{B}})\delta t}$, where $\hat{\mathbf{B}}$ is the estimate of the magnetic field from the previous pulse. For large N and $\delta t \to 0$, the QFIM takes the form

$$\max I(\rho_{\boldsymbol{\theta}}; \boldsymbol{\theta}) = 4 \begin{pmatrix} t^2 & 0 & 0 \\ 0 & B^2t^2 & 0 \\ 0 & 0 & B^2t^2\cos^2\theta \end{pmatrix}, \tag{3.35}$$

which represents the best precision attainable for the simultaneous estimation of the three parameters, *i.e.*, the magnetic field. Experiments were conducted to demonstrate the efficacy and feasibility of the 'anti-evolution' scheme by Hou *et al.* [57]. Figure (3.10) presents experimental results with the ideal, non-adaptive, and adaptive control schemes. They demonstrate a precision close to the Heisenberg limit.

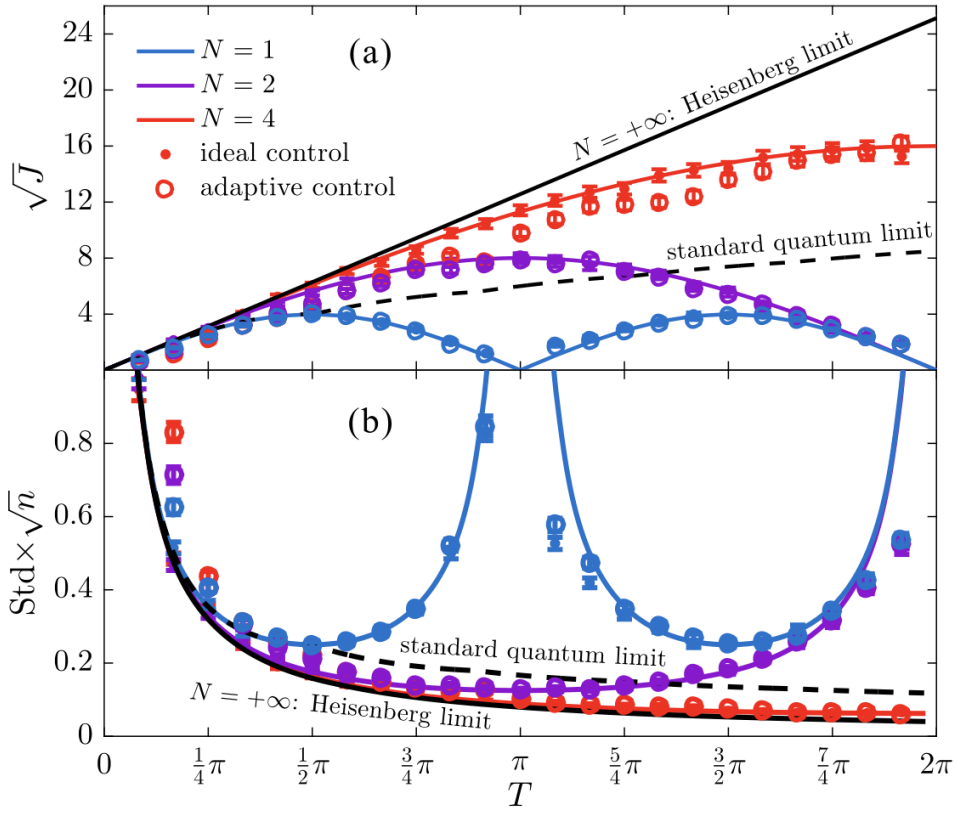

Figure 3.10: (Taken from Ref. [57]). a)Square root of the Quantum Fisher Information J. (b) Standard deviation. The performance is shown for adaptive controls with $N = 1, 2$, and 4, represented by blue, purple, and red, respectively. The experimental results (circles) closely match the optimal theoretical predictions (solid lines).

Chapter 4

Metrology in noisy channels

Metrology in noisy channels explores how the presence of environmental noise affects the precision that can be achieved by a measurement protocol. The first section will examine the characteristics of noisy channels, their impact on quantum states, and the limitations they impose on metrological tasks. The second section will focus on how ancilla-assisted strategies leverage quantum correlations to enhance parameter estimation, potentially restoring or surpassing the precision lost due to noise. The third section will analyse the influence of partial or complete ignorance of the rotation axis in a rotation angle estimation protocol.

In this chapter, we will need to compute the QFI numerically. To do so, we have developed a Julia code to compute the QFI either based on the spectral decomposition of the density matrix or on the Bures distance. This code can be found in the github repository `https://github.com/diegolall/qfish_jl/tree/main`.

4.1 Noisy channels

A quantum channel is a mathematical object that describes the evolution of states in an open quantum system, usually resulting from interaction with an environment. Unlike unitary evolution, which governs isolated quantum systems, quantum channels account for noise, decoherence, and dissipation. In the next section, we will give a brief explanation on how to describe the evolution of the system of interest when noise/decoherence is present. This is done by introducing a mathematical tool called a *quantum channel*.

4.1.1 Quantum channels

Physically, a quantum channel is a mathematical object that represents a transformation that the state of a quantum system can undergo (due, *e.g.*, to measurement, unitary evolution or dissipative evolution). The evolution of the density operator $\rho(t)$ over a time t will be described by the action of a superoperator $\mathcal{E}_t(\cdot)$ on the initial state $\rho(0)$, such that $\mathcal{E}_t(\rho(0)) = \rho(t)$. Formally, a quantum channel $\mathcal{E}$ is a linear application (commonly know as a *superoperator*) defined as [59]

$$\mathcal{E}(\cdot) : \mathcal{B}(\mathcal{H}) \to \mathcal{B}(\mathcal{H}), \quad \rho \mapsto \mathcal{E}(\rho) \tag{4.1}$$

that is completely positive and trace-preserving (CPT). Here, $\mathcal{B}(\mathcal{H})$ is the space of bounded linear operators on $\mathcal{H}$. For finite-dimensional Hilbert spaces, $\mathcal{L}(\mathcal{H}) = \mathcal{B}(\mathcal{H})$, with $\mathcal{L}(\mathcal{H})$ the space of linear operators on $\mathcal{H}$. A CPT channel has the following properties

- Linearity: $\mathcal{E}\big(\sum_k p_k \rho_k\big) = \sum_k p_k \mathcal{E}(\rho_k)$

- Positivity: $\mathcal{E}(\rho) \geq 0 \quad (\Rightarrow \mathcal{E}(\rho)^\dagger = \mathcal{E}(\rho)$ in finite-dimensional Hilbert spaces)
- Complete positivity: $(\mathcal{E} \otimes \mathbb{1})(\sigma) \geq 0 \quad$ for all density operators $\sigma \in \mathcal{L}(\mathcal{H} \otimes \mathcal{H}')$
- Trace preservation: $\mathrm{Tr}\left[\mathcal{E}(\rho)\right] = \mathrm{Tr}\left[\rho\right] = 1$

A quantum operation is called unital when it preserves the identity ($\mathcal{E}(\mathbb{1}) = \mathbb{1}$). Sometimes, quantum channels are called quantum maps. If they are completely positive and trace-preserving, we will abbreviate them as CPTM. Let us now review some well-known quantum channels.

One of the cornerstone of the theory of quantum channels is Kraus decomposition theorem.

Theorem 4.1. *A map $\mathcal{E}$ is a quantum operation if and only if it is the partial trace of a unitary evolution on a larger Hilbert space with an initial factorization or, equivalently, if it admits a Kraus decomposition*

$$\mathcal{E}(\rho) = \sum_{k=0}^{n-1} M_k \rho M_k^\dagger \,, \tag{4.2}$$

where $\{M_k : k = 0, \ldots, n-1\}$ is a set of operators (called Kraus operators, measurement operators, or superoperator generators) in a number $n \leq \dim(\mathcal{H})^2$ satisfying the closure relation

$$\sum_{k=0}^{n-1} M_k^\dagger M_k = \mathbb{1}. \tag{4.3}$$

Unitary evolution channel

As a first example, if the evolution is unitary and described by the evolution operator U_S, it is easy to check that the corresponding channel is

$$\mathcal{E}_{U_S}(\rho) = U_S \rho U_S^\dagger \,. \tag{4.4}$$

It is clear that this quantum map is a CPTM and there is only one Kraus operator U_S.

Projective measurement channel

Let us consider a projective measurement with its corresponding projection operator P. The postulates of quantum mechanics tell us that the state after measurement is

$$|\psi\rangle = \frac{P\,|\psi_0\rangle}{\|P\,|\psi_0\rangle\|} \,. \tag{4.5}$$

Straightforwardly, the quantum channel corresponding to a projective measurement is

$$\mathcal{E}(\rho) = \frac{P\rho P^\dagger}{\mathrm{Tr}\left[P\rho P^\dagger\right]} \,, \tag{4.6}$$

which is also a CPTM. Just as for the unitary evolution channel, there is only one Kraus operator, this time equal to $P/\sqrt{\mathrm{Tr}\left[P\rho P^\dagger\right]}$.

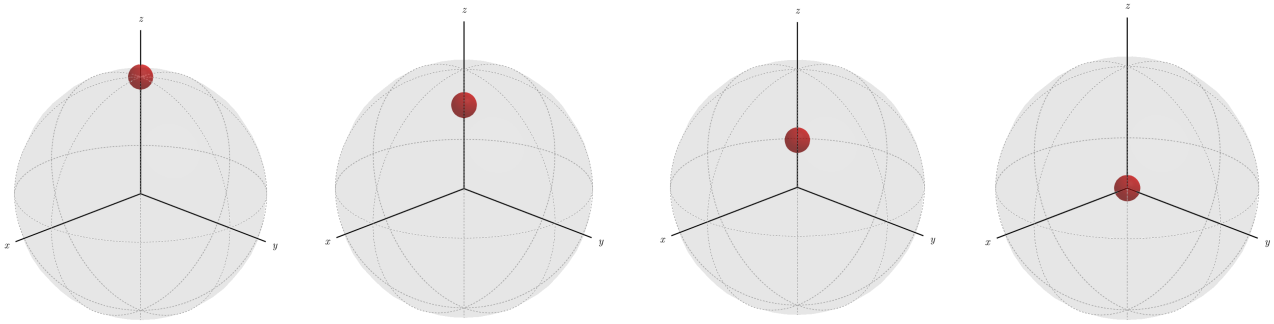

(a) (b) (c) (d)

Figure 4.1: Effects of the depolarizing channel visualized in the Bloch ball representation at (a) $p = 0$ (pure state), (b) $p = 0.3$ (mixed state), (c) $p = 0.6$ (mixed state), and (d) $p = 1$ (maximally mixed state).

Depolarizing channel

A quantum depolarizing channel is a model of noise in a quantum system. The channel depends on a single parameter p and maps the state ρ into a mixture of itself and the maximally mixed state $\frac{\mathbb{1}}{d}$, where d is the dimension of the Hilbert space. It is defined as

$$\mathcal{E}_{\text{depo}}(\rho\,; p) \stackrel{\text{def}}{=} (1-p)\rho + p\frac{\mathbb{1}}{d}\,. \tag{4.7}$$

This channel is known to be CPTM [60].

If the system is a single qubit, the corresponding Kraus operators are

$$M_0 = \sqrt{1-\frac{3p}{4}}\mathbb{1}, \quad M_1 = \sqrt{\frac{p}{4}}\sigma_x, \quad M_2 = \sqrt{\frac{p}{4}}\sigma_y, \quad M_3 = \sqrt{\frac{p}{4}}\sigma_z\,. \tag{4.8}$$

We can interpret geometrically this channel as a uniform contraction of the Bloch ball parametrized by p. As an illustration, Fig. 4.1 shows the Bloch ball representation, which states that any qubit density operator can be represented as

$$\rho = \frac{\mathbb{1} + \boldsymbol{\sigma}\cdot\mathbf{r}}{2} \tag{4.9}$$

with $\boldsymbol{\sigma} = (\sigma_x, \sigma_y, \sigma_z)$, $\mathbf{r} \in \mathbb{R}^3$ and $|\mathbf{r}| \leq 1$. Pure states are represented by a point onto the surface of the ball (*i.e*, the sphere) and mixed states by a point inside the ball. The maximally mixed state ($\mathbb{1}/2$) is represented by a point at the center of the ball (*i.e.*, the origin of the cartesian coordinates). Figure 4.2a shows the evolution of the state purity ($\text{Tr}\,[\rho^2]$) as a function of p.

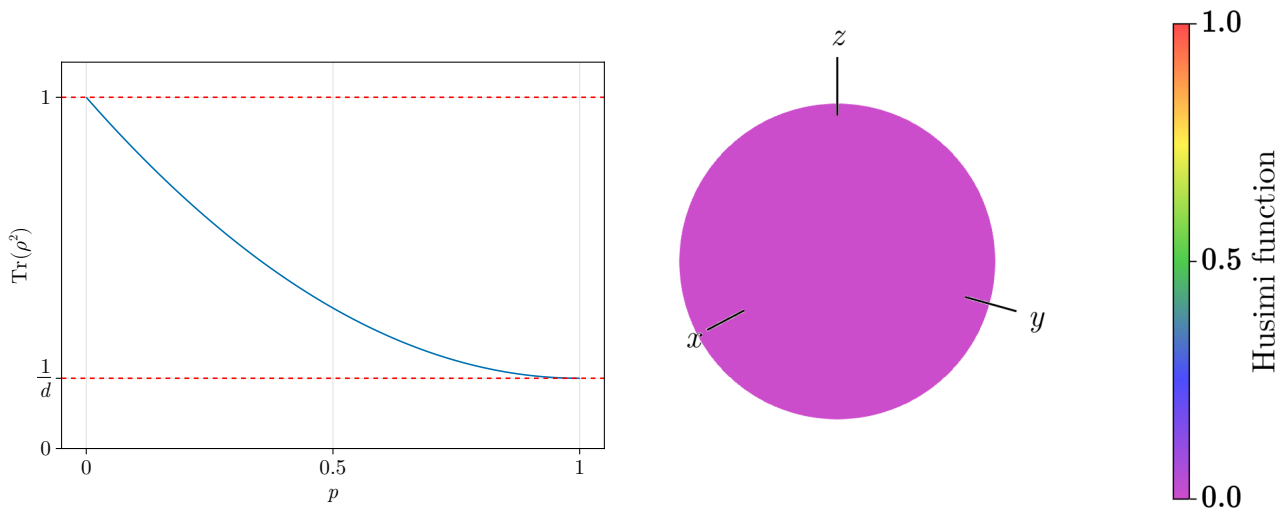

(a) (b)

Figure 4.2: (a) Evolution of the purity of a state after passing through a depolarizing channel of a quantum system with $d = 5$. Purity of 1 corresponds to a pure state, while a purity of $\frac{1}{d}$ corresponds to the maximally mixed state. (b) Husimi distribution of the maximally mixed state in a Hilbert space of dimension d.

Let us have a quick discussion about the maximally mixed state. In this chapter, our goal is to provide tools to counteract the noise introduced by noisy channels in a quantum measurement protocol. Our focus here is on estimating rotation angles. Naturally, this requires states that are sensitive to such rotations. Intuitively, states that possess certain symmetries along specific axes are poor candidates for measuring rotation angles about those same axes. Now, Fig. 4.2b shows the Husimi distribution of the maximally mixed state, which appears to be zero everywhere — indicating that the state is isotropic. This isotropy can also be seen from the fact that any unitary operation U leaves the maximally mixed state unchanged, *i.e.*, $U\frac{\mathbb{1}}{d}U^\dagger = \frac{\mathbb{1}}{d}$. This means that no information can be extracted in a measurement protocol that uses a maximally mixed state as a probe. In other words, the corresponding Quantum Fisher Information (QFI) will always be zero.

4.2 Ancilla assisted metrology

4.2.1 Fighting depolarization

In order to gain a better understanding of the effects of the depolarization channel on the QFI, we will first study the simplest protocol shown in Fig. 4.3. The input state goes through a depolarization channel, followed by a rotation about $\mathbf{n}$, and finally a measurement is performed. A more realistic scenario involves the depolarization channel applied over the whole process, including at the step where the rotation occurs. However, since both channels commutes $\mathcal{E}_{\text{depo}}(\mathcal{E}_{U_S}(\rho)) = \mathcal{E}_{U_S}(\mathcal{E}_{\text{depo}}(\rho))$, the realistic scenario is perfectly modeled by the one in Fig. 4.3.

Figure 4.4 shows the evolution of the QFI as a function of $1 - p$. To remain as general as possible, we compute the QFI for three families of well-known states, each one defined for any system size, *i.e.*, the number of qubits $N = 2j$ with j the spin number (we consider sizes from $N = 4$ to 20): coherent states described in Sec. 3.3.1, GHZ states, and anticoherent states. Each states lives in a d-dimensional Hilbert space with $d = 2j + 1$. A state $|\phi\rangle$ is an order-t

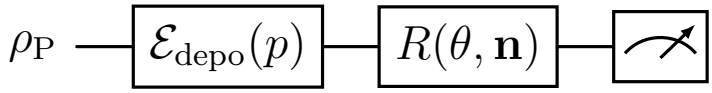

Figure 4.3: The input state ρ_{P} first undergoes depolarization via a depolarizing channel $\mathcal{E}_{\mathrm{depo}}(p)$, where p is the depolarization probability. The parameter θ is then encoded into the depolarized state via a rotation about an axis $\mathbf{n}$. The state is subsequently measured.

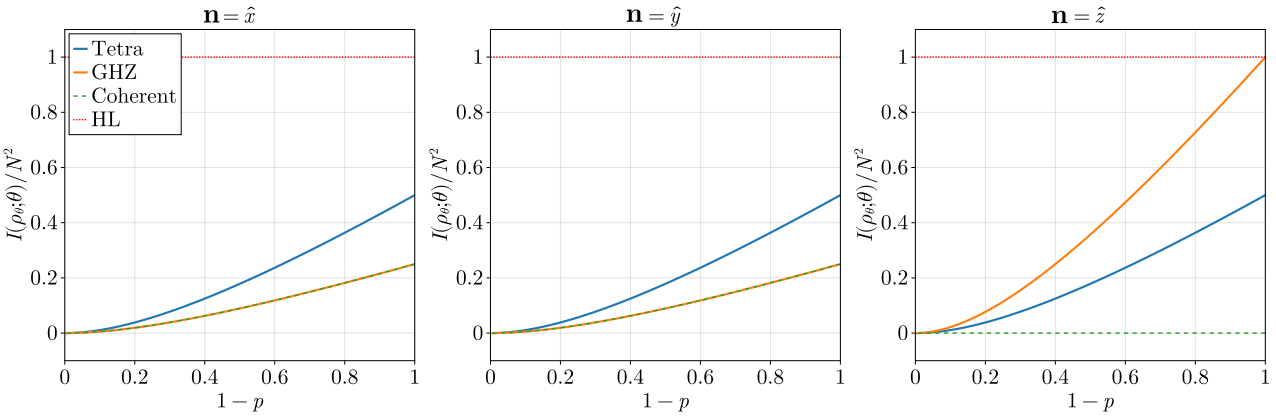

Figure 4.4: $I(\rho_\theta;\theta)/N^2$ versus p with p the depolarization probability, for $N = 4$ spin-1/2 particles, $\mathbf{n}$ the rotation axis and $\hat{i}$ is the direction of the i-axis ($i \in x, y, z$). The states considered are: the coherent state $|0, 0, 4\rangle$, the 2-AC state $|\psi^{\mathrm{tetra}}\rangle = \left(1, 0, i\sqrt{2}, 0, 1\right)/2$ and the GHZ state given by Eq. (3.16). The red dotted line represents the Heisenberg limit (HL).

anticoherent state if $\langle\phi|(\mathbf{J}\cdot\mathbf{n})^k|\phi\rangle$ is independent of $\mathbf{n}$ for all $k = 1, \ldots, t$ [61]. An example of an order-2 anticoherent state is the so-called tetrahedron[1] state, $|\psi^{\mathrm{tetra}}\rangle = \left(1, 0, i\sqrt{2}, 0, 1\right)/2$, where the coefficients of the vector indicate the coefficients in the $|j, m\rangle$ basis. Figure 4.5a shows the Husimi distribution and the Majorana stellar representation of $|\psi^{\mathrm{tetra}}\rangle$.

A first observation is that the QFI of each state decreases monotonically to 0 as $p \to 1$ (*i.e.*, $1 - p \to 0$). This is expected since $p = 1$ corresponds to the maximally mixed state, which is isotropic and, consequently, $I(\rho_\theta;\theta) = 0$. This behaviour can be shown mathematically using the expression of the channel and the convexity of the QFI. We have

$$\begin{aligned} I\big(\mathcal{E}\left(\rho_{\mathrm{P}}\right);\theta\big) &= I\left((1-p)\rho_{\mathrm{P}} + p\frac{\mathbb{1}}{d};\theta\right) \\ &\leq (1-p)I(\rho_{\mathrm{P}};\theta) + p\underbrace{I\left(\frac{\mathbb{1}}{d};\theta\right)}_{=0} \\ \implies I\big(\mathcal{E}\left(\rho_{\mathrm{P}}\right);\theta\big) &\leq (1-p)I(\rho_{\mathrm{P}};\theta)\,. \end{aligned} \tag{4.10}$$

The last equation shows that the dependence of the QFI on the depolarizing parameter is, at best, linear in $(1 - p)$. This is also observed in Fig. 4.4, where the behaviour appears to be sublinear. Simple calculations show that the dependence is not quadratic either. A more detailed calculation is needed to determine the exact functional dependence.

Consider the case of a pure input state $\rho = |\psi\rangle\langle\psi|$, where $|\psi\rangle$ will be either a GHZ, an anticoherent or a coherent state. The GHZ state is an entangled state of N subsystems (here

[1]The name of the state comes from the fact that the Majorana points of the state lie at the vertices of a regular tetrahedron. More details about the Majorana representation of spin states can be found in [39].

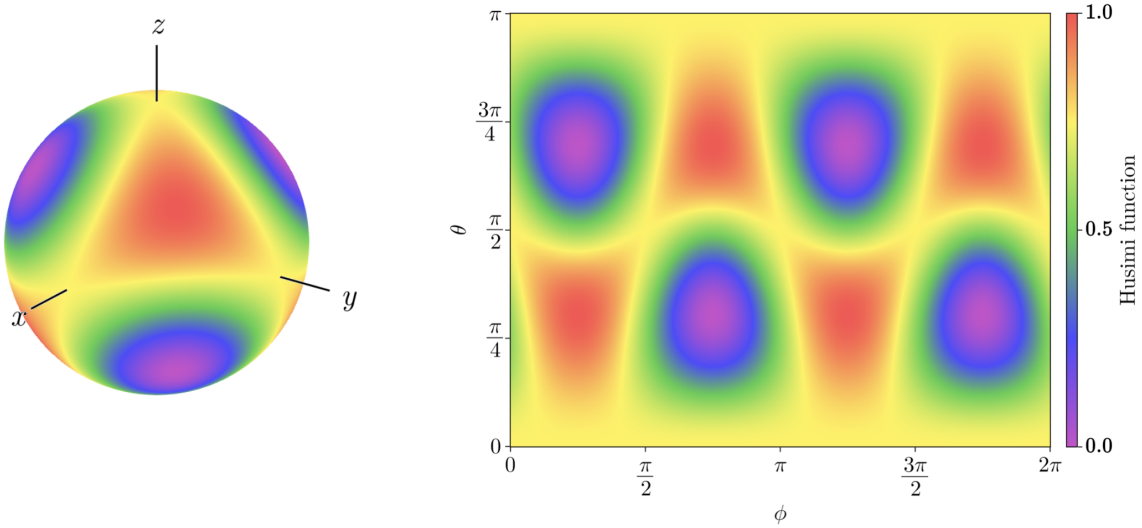

(a)

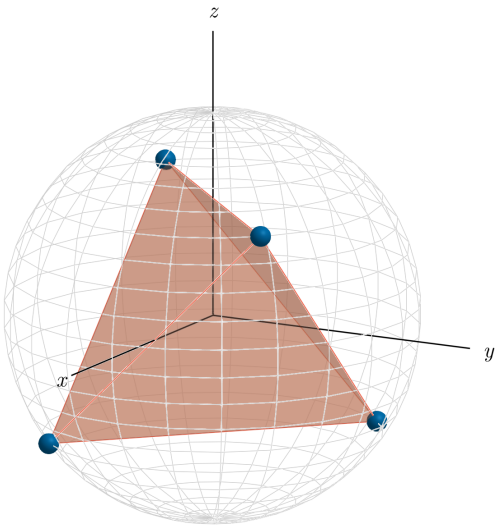

(b)

Figure 4.5: Representation of the tetrahedron state of a spin-2 system, $|\psi^{\text{tetra}}\rangle = \left(1, 0, i\sqrt{2}, 0, 1\right)/2$. (a) Husimi distribution of the tetrahedron state. (b) Majorana stellar representation of the tetrahedron state. The name of the state comes from the arrangement of its Majorana stars.

N	j	t	$\|\psi\rangle$	Name
4	2	1	$\|\psi^{\text{tetra}}\rangle = \left(1, 0, i\sqrt{2}, 0, 1\right)$	Tetrahedron
4	2	1	$\|\psi^{\text{tetra}'}\rangle = \left(1, 0, -i\sqrt{2}, 0, 1\right)$	Tetrahedron bis
5	5/2	1	$\|\psi^{5/2}\rangle = \left(\sqrt{3}, 0, 0, 0, \sqrt{5}, 0\right)$	/
6	3	1	$\|\psi^{\text{octa}}\rangle = \left(0, \sqrt{3/5}, 0, 0, 0, 0, \sqrt{2/5}\right)$	Octahedron
7	7/2	2	$\|\psi^{7/2}\rangle = \left(0, 0, \sqrt{7}, 0, 0, 0, 0, \sqrt{3}\right)$	/
10	5	1	$\|\psi_1^5\rangle = (1, 0, 0, 0, 0, 0, 0, 0, 0, 0, 1)$	/
10	5	2	$\|\psi_2^5\rangle = \left(0, 0, 0, \sqrt{5}, 0, 0, 0, 0, 0, 0, \sqrt{2}\right)$	/

Table 4.1: Non-exhaustive list of anticoherent states classified by the number of qubits N, their spin $j = N/2$, and the order of anticoherence t [61]. States should be normalized to represent valid physical states.

qubits) defined as

$$|\text{GHZ}\rangle \stackrel{\text{def}}{=} \frac{|0\rangle^{\otimes N} + |1\rangle^{\otimes N}}{\sqrt{2}} \,. \tag{4.11}$$

Table 4.1 presents some examples of anticoherent states of various orders t and number of qubits N. Unless otherwise stated, the state used in the simulations is the 4-qubit tetrahedron state $|\psi^{\text{tetra}}\rangle$. The definition implies that a t-anticoherent state $|\psi\rangle$ has no privileged direction in space up to order t, in contrast to spin coherent states which are maximally aligned along a specific direction.

The state first undergoes depolarization with probability p and we let

$$\rho_p \equiv \mathcal{E}(\rho) = (1-p)\rho + \frac{p}{d}\mathbb{1} \,, \tag{4.12}$$

where $\mathcal{E}$ is a depolarization channel and d is the dimension of the Hilbert space. The state then undergoes a rotation generated by $G \in \{J_x, J_y, J_z\}$; formally, the state becomes $\rho_p(\theta) = e^{-i\theta G}\rho_p e^{i\theta G}$. We can rewrite Eq. (2.22) as

$$\frac{I(\rho_p;\theta)}{Nt^2} = \sum_{i,j} \frac{2\left|\,\langle i|\partial_\theta \rho_p(\theta)|j\rangle\,\right|^2}{\lambda_i + \lambda_j} \,, \tag{4.13}$$

with $|i\rangle$ the ith eigenvector relative to the eigenvalue λ_i of ρ_p. We directly find the eigenvalues and eigenvectors of ρ_p

$$\lambda_1 = (1-p) + \frac{p}{d}, \quad \text{with eigenvector } |\psi\rangle \tag{4.14}$$

$$\lambda_i = \frac{p}{d}, \quad \text{with } |\phi_i\rangle \text{ for } i = 2, \ldots, d, \tag{4.15}$$

where $\{|\phi_i\rangle\}_{i=2}^d \perp |\psi\rangle$ is an orthogonal basis of the orthogonal complement of $|\psi\rangle$. We can expand $\partial_\theta \rho_p(\theta)$ as

$$\begin{aligned} \partial_\theta \rho_p(\theta) &= \partial_\theta \left(e^{-i\theta G}\rho_p e^{i\theta G}\right) \\ &= -iGe^{-i\theta G}\rho_p e^{i\theta G} + ie^{-i\theta G}\rho_p e^{i\theta G}G \,. \end{aligned} \tag{4.16}$$

The last expression is valid for any θ, especially for $\theta = 0$ which leads to

$$\begin{aligned}\partial_\theta \rho_p(\theta) &= -iG\rho_p + i\rho_p G \\ &= -i\left[G, \rho_p\right] \ .\end{aligned} \tag{4.17}$$

Therefore, we can compute the value of the bracket in Eq. (4.13)

$$\begin{aligned}\langle i|\partial_\theta \rho_p(\theta)|j\rangle &= \langle i| - i\left[G, \rho_p\right]|j\rangle \\ &= -i(\langle i|G\rho_p|j\rangle - \langle i|\rho_p G|j\rangle) \\ &= -i(\lambda_i - \lambda_j)\langle i|G|j\rangle \, .\end{aligned} \tag{4.18}$$

The last equation indicates that the only non-vanishing elements are the off-diagonals terms. Finally, the QFI becomes

$$\begin{aligned}\frac{I(\rho_p;\theta)}{Nt^2} &= \sum_{i=2}^{d} \frac{4\left|\langle\psi|\partial_\theta\rho_p|\phi_i\rangle\right|^2}{\lambda_1 + \lambda_i} \\ &= \sum_{i=2}^{d} \frac{4\left|(1-p)\langle\psi|G|\phi_i\rangle\right|^2}{1-p+\frac{p}{d}+\frac{p}{d}} \\ &= \frac{4(1-p)^2}{1-p+\frac{2p}{d}} \sum_{i=2}^{d} |\langle\psi|G|\phi_i\rangle|^2 \\ &= \frac{4(1-p)^2}{1-p+\frac{2p}{d}} \mathrm{Var}[G, |\psi\rangle].\end{aligned} \tag{4.19}$$

The latter equation perfectly fits the results of the simulations shown in Fig. 4.4. Figure 4.6 presents Eq. (4.19) normalized by $\mathrm{Var}[G, |\psi\rangle]$, that is, the prefactor that depends only on p and d. Note that if the variance of a state with respect to G vanishes, the depolarizing channel will not have any effect on the QFI, since it is already zero. This is the case for the coherent spin state $|0, 0, 4\rangle$ with respect to $G = J_z$, as it is aligned along the z axis. As previously noted, the behaviour observed in Fig. 4.6 is sublinear for finite dimension, but nevertheless remains above that of a quadratic law. Interestingly, as the system dimension increases, the quantum Fisher information decreases at a slower rate. In the thermodynamic limit, *i.e.*, $d \to \infty$, we obtain a linear scaling with the depolarizing probability

$$\lim_{d\to\infty} \frac{I(\rho_p;\theta)}{Nt^2\mathrm{Var}[G;|\phi\rangle]} = 4(1-p) \ . \tag{4.20}$$

This result shows that, under depolarizing noise, it is advantageous to use large-scale systems for a probability of depolarization. However, caution is required, as such systems are generally harder to control and more susceptible to other decoherence effects, due to their higher number of degrees of freedom and stronger coupling to the external environment.

Clearly, when $p = 0$, the QFI depends solely on the variance of G with respect to the given state. As a result, two different states will generally have different initial QFI values. In contrast, when $p = 1$, the QFI vanishes regardless of the initial state. This is expected, since $p = 1$ corresponds to complete depolarization, transforming any state into the maximally mixed (and thus isotropic) state.

We also observe that for every rotation axis, the coherent state is the least efficient pure state for $\mathbf{n} = \hat{x}$ and $\mathbf{n} = \hat{y}$, and completely ineffective for $\mathbf{n} = \hat{z}$. This is expected, as the coherent state used is $|0, 0, 4\rangle$, which possesses rotational symmetry around the z axis.

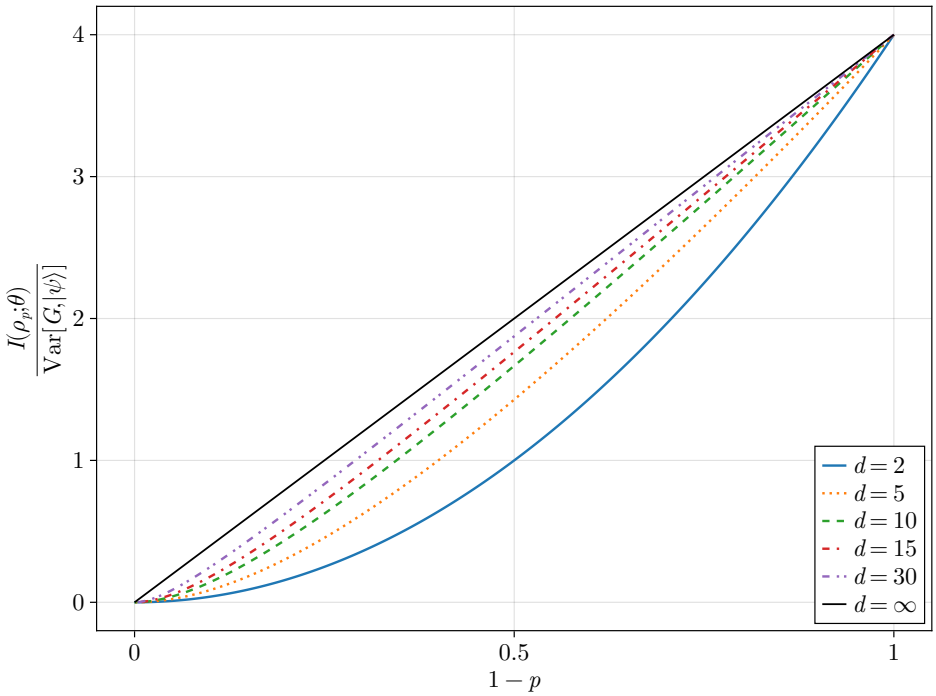

Figure 4.6: Normalized QFI versus $1-p$ with p the depolarization probability, as given by Eq. (4.19), for various system dimensions. We assume that $\mathrm{Var}[G,|\psi\rangle] \neq 0$.

Simulations also show that the GHZ state is the optimal state for estimation of rotations about the z axis. This result is well known and has been proved in [62]. Here, we have taken the z axis as the quantization axis, and thus as the preferred direction of the system. As a consequence, given our definition, the GHZ state also exhibits a preferred orientation along the z axis. Naturally, had we chosen a different axis as the quantization axis, the results would remained unchanged, up to a rotational symmetry. Furthermore, it seems that the tetrahedron state is the most suitable choice when the rotation axis is *a priori* unknown, as it has been observed and proved in the literature [63].

Now that we have a better understanding of the effects of the depolarizing channel on the QFI, we can present our results on how to mitigate the loss of QFI, *i.e.*, the impact of depolarization. To this end, we will consider the same three states as previously (see Fig. 4.4), namely the GHZ state, the 2-AC tetrahedron state, and the coherent state. The first two states are of particular interest, as they are known to offer the best performance in rotation angle estimation protocols. The latter is included primarily to provide a baseline for comparison with a classical, and thus less performant, state.

To compensate for the effects of depolarization, we introduce an ancillary qubit, whose state is described by a density matrix ρ_{A}. The state of the global system thus becomes $\rho = \rho_{\mathrm{P}} \otimes \rho_{\mathrm{A}}$. Initially, the qubit is in a pure state parametrized by α, such that

$$\rho_{\mathrm{A}}(\alpha) = |\varphi(\alpha)\rangle\langle\varphi(\alpha)| \quad \text{with} \quad |\varphi(\alpha)\rangle = \cos\frac{\alpha}{2}|\uparrow\rangle + \sin\frac{\alpha}{2}|\downarrow\rangle, \tag{4.21}$$

where $|\uparrow\rangle = \begin{pmatrix}1\\0\end{pmatrix} \equiv |0\rangle_{\mathrm{A}}$ and $|\downarrow\rangle = \begin{pmatrix}0\\1\end{pmatrix} \equiv |1\rangle_{\mathrm{A}}$. In the new ancilla-assisted protocol, we apply an entangling unitary gate on the probe-ancilla system before rotating the probe state. Figure 4.7 shows the circuit representation of the protocol. We can use any kind of unitary gate but we will here focus on the gate generated by the following ZZ Hamiltonian (setting

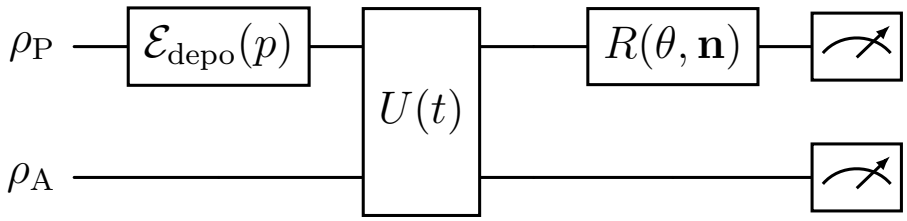

Figure 4.7: Phase estimation protocol using a unitary gate. ρ_{P} is the input probe state, and ρ_{A} is an ancillary qubit. First, the probe state undergoes depolarization via a depolarizing channel $\mathcal{E}(p)$, where p is the depolarization probability. A unitary gate $U(t)$ involving both the probe and the ancilla is then applied. The parameter θ is subsequently encoded onto the probe alone via a rotation around the axis $\mathbf{n}$. Finally, both systems can be measured.

$\hbar = 1$)

$$H = \omega_P J_z + \omega_A \sigma_z + g J_z \sigma_z \tag{4.22}$$

where ω_P and ω_A represent the energy splitting of the probe and the ancillary qubit, respectively, and g is the coupling strength between the two. This will be used as the generator of the following unitary gate parametrized by t

$$U(t) = e^{-itH}. \tag{4.23}$$

For quantum metrology purposes—specifically, maximizing the QFI—numerical simulations show that we must set $\alpha = \frac{\pi}{2}$ in Eq. (4.21) to achieve this maximum [64]. This corresponds to an eigenstate of σ_x with eigenvalue $+1$.

Greenberger–Horne–Zeilinger states

Considering the protocol defined by the circuit in Fig. 4.7, we performed numerical simulations to explore the effects of the gate U on the QFI. Figures 4.8a and 4.8b show the QFI as a function of the depolarizing probability p and gt. We only consider $G = J_x$ and $G = J_z$ since the rotation with $G = J_y$ has the same results as the one for J_x.

Let us elaborate on Fig. 4.8a, which shows the QFI for a rotation around the x-axis ($G = J_x$). At first glance, we notice that the QFI appears to be a periodic function with respect to the variable gt, with a period of π. To confirm this, we ran the simulations again over a larger interval of gt. Figure 4.9 clearly shows this periodicity, so we will restrict our analysis to $gt \in [0, \pi]$ without loss of generality. For a low probability of depolarization p, that is, $1 - p \approx 1$, the QFI appears to be unaffected by the application of the unitary. However, for strong depolarization, *i.e.*, $1 - p \approx 0$, we clearly observe that, for specific values of gt, the use of the unitary provides advantages in the estimation protocol. Surprisingly, the maximum QFI is achieved at $p = 1$ and $gt = \pi/2$, with a value of $I(\rho_\theta, \theta) = N^2/2$. We also observe that for $gt = 0$ and $gt = \pi$, the resulting QFI is not affected by the unitary. This is expected as $\exp(-i0H) = \exp(-i\pi H) = \mathbb{1}$. If the unitary gate is the identity operator, then the protocol is equivalent to the first protocol represented in Fig. 4.3. Interestingly, we observe that we are able to increase the sensitivity, *i.e.*, the QFI, of a probe via a well-suited coupling to an ancilla. However, Fig. 4.8b, which shows the QFI for a rotation around the z axis ($G = J_z$), shows no improvement or significant change in the QFI. We conclude that there is no advantage in using a ZZ coupling when the rotation is around the z axis.

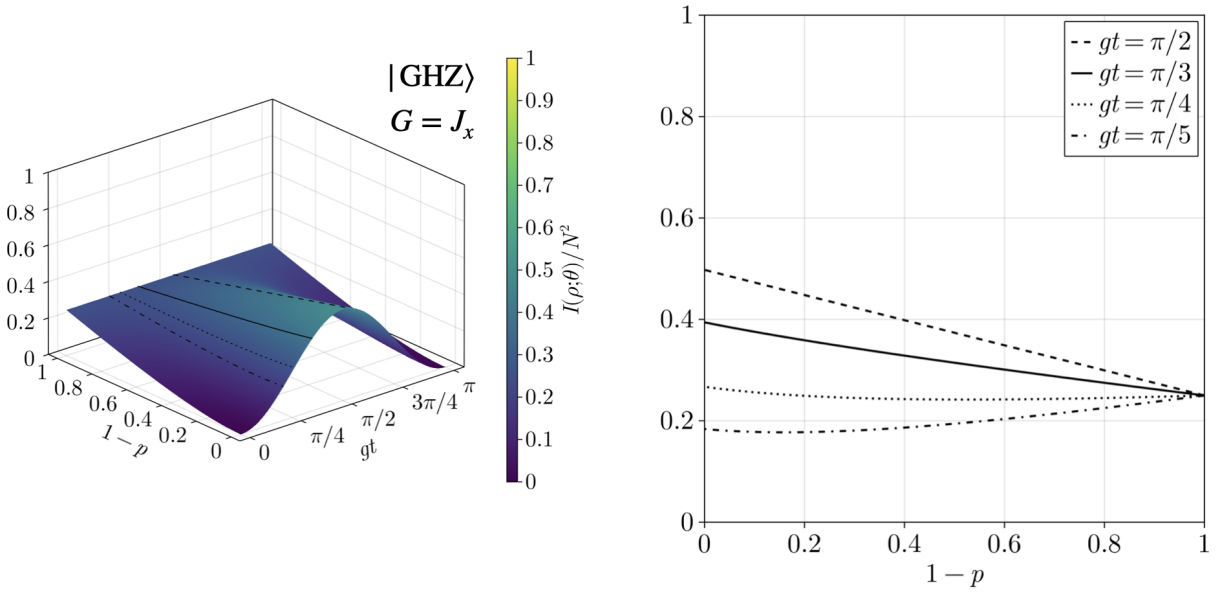

(a) QFI $I(\rho_\theta;\theta)$ for a rotation with $G = J_x$.

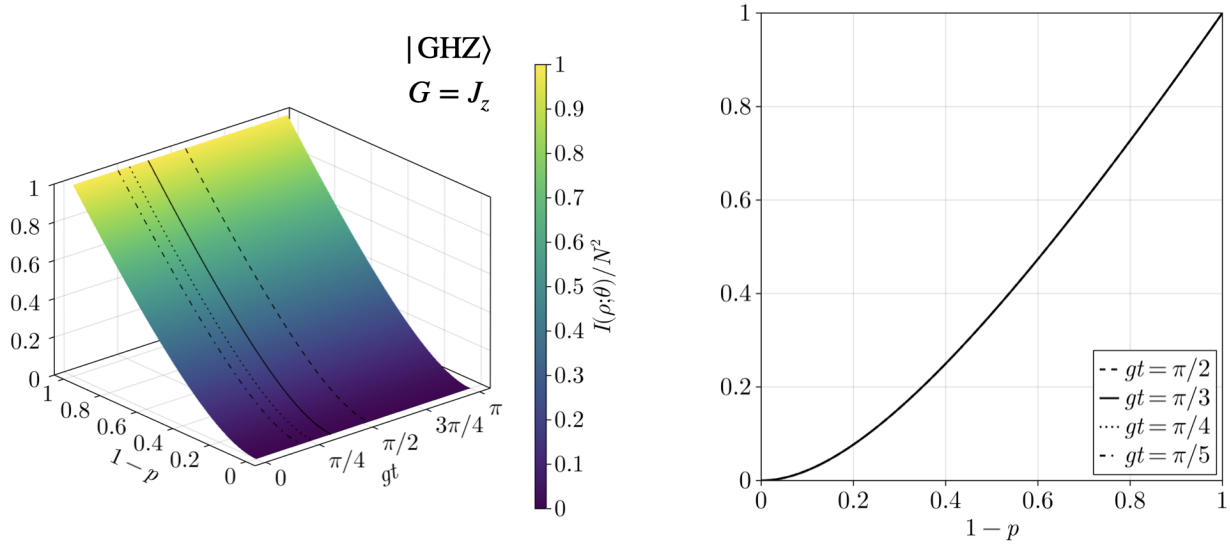

(b) QFI $I(\rho_\theta;\theta)$ for a rotation with $G = J_z$.

Figure 4.8: QFI of the 5-qubit GHZ state coupled with an ancilla as a function of the depolarization probability p and the application time gt of the unitary gate.

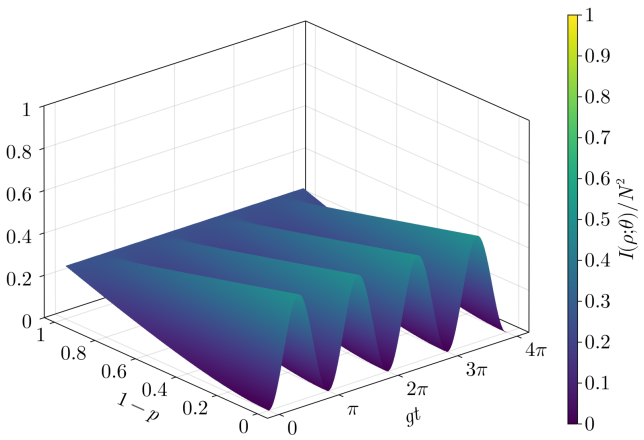

Figure 4.9: QFI $I(\rho_\theta, \theta)$ of a GHZ state coupled to an ancilla via the unitary $U(t) = e^{-igtJ_z\sigma_z}$ for $gt \in [0, 4\pi]$. The parameter is encoded via a rotation around the x-axis.

We now turn to an analytical approach. We start our calculation with the input probe state $|\mathrm{GHZ}\rangle$ and the input ancilla state $\rho_A(\alpha)$ with $\alpha = \pi/2$. The global state is thus

$$\rho(0) = |\mathrm{GHZ}\rangle\langle\mathrm{GHZ}| \otimes \left(\frac{|0\rangle_\mathrm{A} + |1\rangle_\mathrm{A}}{\sqrt{2}} \frac{\langle 0|_\mathrm{A} + \langle 1|_\mathrm{A}}{\sqrt{2}} \right) . \tag{4.24}$$

After applying the depolarizing channel to the probe state, we obtain the global state

$$\rho(0) = \left((1-p)\,|\mathrm{GHZ}\rangle\langle\mathrm{GHZ}| + \frac{p}{d}\mathbb{1} \right) \otimes |+\rangle\langle+| \,. \tag{4.25}$$

where we introduced the notation $|+\rangle = \frac{|0\rangle_\mathrm{A}+|1\rangle_\mathrm{A}}{\sqrt{2}}$ and $|-\rangle = \frac{|0\rangle_\mathrm{A}-|1\rangle_\mathrm{A}}{\sqrt{2}}$ to simplify expressions. We can rewrite the global input state in a more compact form as

$$\begin{aligned} \rho(0) &= \left((1-p)\,|\mathrm{GHZ}\rangle\langle\mathrm{GHZ}| + \frac{p}{d}\mathbb{1} \right) \otimes |+\rangle\langle+| \\ &= \underbrace{\left((1-p)\,|\mathrm{GHZ}\rangle\langle\mathrm{GHZ}| \otimes |+\rangle\langle+| \right)}_{\text{pure state}} + \underbrace{\left(\frac{p}{d}\mathbb{1} \otimes |+\rangle\langle+| \right)}_{\text{mixed state}} \end{aligned} \tag{4.26}$$

where we divided $\rho(0)$ into a mixture of a pure state and a mixed depolarized state. We now need to compute the state after applying the unitary gate $U(t)$. This amounts to computing the evolution of the pure and the mixed components separately. Let us first compute the pure component. Omitting the prefactor, we can rewrite the pure state as the ket vector $|\mathrm{GHZ}\rangle\otimes|+\rangle$. We then have

$$\begin{aligned} U(t)\,|\mathrm{GHZ}\rangle \otimes |+\rangle &= \exp\left(-itH\right) |\mathrm{GHZ}\rangle \otimes |+\rangle \\ &= \exp\big(-it(\omega_P J_z + \omega_A \sigma_z + g J_z \sigma_z) \big) \left(\frac{|0\rangle^{\otimes N} + |1\rangle^{\otimes N}}{\sqrt{2}} \otimes |+\rangle \right) . \end{aligned}$$

The unitary $U(t)$ acts trivially on $|0\rangle^{\otimes N}$ and $|1\rangle^{\otimes N}$ because they are eigenstates of J_z. Using $J_z\,|0\rangle^{\otimes N} = +\frac{N}{2}\,|0\rangle^{\otimes N}$ and $J_z\,|1\rangle^{\otimes N} = -\frac{N}{2}\,|1\rangle^{\otimes N}$, we have for $|0\rangle^{\otimes N} \otimes |+\rangle$

$$H\left(|0\rangle^{\otimes N} \otimes |+\rangle \right) = \left(\omega_P \frac{N}{2} + \omega_A \sigma_z + g \frac{N}{2} \sigma_z \right) |0\rangle^{\otimes N} \otimes |+\rangle \ . \tag{4.27}$$

Therefore the evolution of the probe is

$$U(t)\left(|0\rangle^{\otimes N}\otimes|+\rangle\right)=e^{-i\omega_P\frac{N}{2}t}\,|0\rangle^{\otimes N}\otimes e^{-i(\omega_A+g\frac{N}{2})\sigma_z t}\,|+\rangle\ . \tag{4.28}$$

We now have to compute the evolution of the ancilla's state. Using $|+\rangle=\frac{|0\rangle_{\mathrm{A}}+|1\rangle_{\mathrm{A}}}{\sqrt{2}}$, and the action of σ_z on its eigenvectors $|0\rangle_{\mathrm{A}}$ and $|1\rangle_{\mathrm{A}}$, we find

$$e^{-i(\omega_A+g\frac{N}{2})\sigma_z t}\left(\frac{|0\rangle_{\mathrm{A}}+|1\rangle_{\mathrm{A}}}{\sqrt{2}}\right)=\frac{e^{-i(\omega_A+g\frac{N}{2})t}\,|0\rangle_{\mathrm{A}}+e^{i(\omega_A+g\frac{N}{2})t}\,|1\rangle_{\mathrm{A}}}{\sqrt{2}}. \tag{4.29}$$

Setting $\alpha_+=\omega_A+g\frac{N}{2}$, we can use the relations $e^{\pm i\alpha_+ t}=\cos(\alpha_+ t)\pm i\sin(\alpha_+ t)$ to obtain

$$e^{-i\alpha_+\sigma_z t}\,|+\rangle=\cos(\alpha_+ t)\,|+\rangle-i\sin(\alpha_+ t)\,|-\rangle\ . \tag{4.30}$$

This allows us to express the full evolution of the state $|0\rangle^{\otimes N}\otimes|+\rangle$ as

$$U(t)\left(|0\rangle^{\otimes N}\otimes|+\rangle\right)=e^{-i\gamma(t)}\,|0\rangle^{\otimes N}\otimes(\cos(\alpha_+ t)\,|+\rangle-i\sin(\alpha_+ t)\,|-\rangle) \tag{4.31}$$

with $\gamma(t)=\omega_P\frac{N}{2}t$.

Using the same type of calculation, we easily find the evolution of $|0\rangle^{\otimes N}\otimes|+\rangle$ under $U(t)$. Similarly, we have that

$$U(t)\left(|1\rangle^{\otimes N}\otimes|+\rangle\right)=e^{i\gamma(t)}\,|1\rangle^{\otimes N}\otimes(\cos(\alpha_- t)\,|+\rangle-i\sin(\alpha_- t)\,|-\rangle) \tag{4.32}$$

with $\alpha_-=\omega_A-g\frac{N}{2}$. Finally, we can express the evolution of the pure state in Eq. (4.26) as

$$\begin{aligned}|\Psi(t)\rangle\equiv U(t)\Big(\,|\mathrm{GHZ}\rangle\otimes|+\rangle\,\Big)=\frac{1}{\sqrt{2}}\Big[e^{-i\gamma(t)}\,|0\rangle^{\otimes N}\otimes\Big(\cos(\alpha_+ t)\,|+\rangle-i\sin(\alpha_+ t)\,|-\rangle\Big)\\ +e^{i\gamma(t)}\,|1\rangle^{\otimes N}\otimes\Big(\cos(\alpha_- t)\,|+\rangle-i\sin(\alpha_- t)\,|-\rangle\Big)\Big]\ .\end{aligned} \tag{4.33}$$

Now we calculate the evolution of the mixed component of (4.26), $U(t)\left(\frac{\mathbb{1}}{d}\otimes|+\rangle\langle+|\right)U(t)^\dagger$, where we have deliberately omitted prefactors. We can decompose the identity operator in the eigenbasis of J_z, which gives us

$$\frac{\mathbb{1}}{d}=\sum_m\frac{|m\rangle\langle m|}{d} \tag{4.34}$$

$$\Rightarrow U(t)\left(\frac{\mathbb{1}}{d}\otimes|+\rangle\langle+|\right)U(t)^\dagger=U(t)\left(\sum_m\frac{|m\rangle\langle m|}{d}\otimes|+\rangle\langle+|\right)U(t)^\dagger\ , \tag{4.35}$$

with $|m\rangle$ the eigenstates of J_z and $m\in\{-N/2,\ldots,N/2\}$. We have to compute the evolution of the state $|m\rangle\otimes|+\rangle$ for each m,

$$\begin{aligned}U(t)\big(\,|m\rangle\otimes|+\rangle\,\big)&=e^{-it(\omega_P J_z+\omega_A\sigma_z+gJ_z\sigma_z)}\big(\,|m\rangle\otimes|+\rangle\,\big)\\&=|m\rangle\otimes e^{-i(\omega_P m+\omega_A\sigma_z+mg\sigma_z)}\,|+\rangle\ .\end{aligned} \tag{4.36}$$

This calculation is straightforward, as it is almost identical to that for the pure case. We thus obtain the final expression for the mixed component after the unitary

$$U(t)\left(\frac{\mathbb{1}}{d}\otimes|+\rangle\langle+|\right)U(t)^\dagger=\sum_m\frac{|m\rangle\langle m|}{d}\otimes|\psi_m(t)\rangle\langle\psi_m(t)|\ , \tag{4.37}$$

with

$$|\psi_m(t)\rangle = e^{-i\omega_P mt}\big(\cos(\theta_m t)\,|+\rangle - i\sin(\theta_m t)\,|-\rangle\big)\,, \tag{4.38}$$

and $\theta_m(t) = \omega_A + gm$. Using Eq. (4.33) and Eq. (4.37), we obtain the full state after the unitary

$$\rho(t) = (1-p)\Big(|\Psi(t)\rangle\langle\Psi(t)|\Big) + \frac{p}{d}\left(\sum_m |m\rangle\langle m| \otimes |\psi_m(t)\rangle\langle\psi_m(t)|\right)\,. \tag{4.39}$$

The states $|0\rangle^{\otimes N} = |m = \frac{N}{2}\rangle$ and $|1\rangle^{\otimes N} = |m = -\frac{N}{2}\rangle$ are the only elements in common between the terms of Eq. (4.39) with $\theta_{\pm N/2}(t) = \alpha_\pm t = \omega_A \pm g\frac{N}{2}$. Thus, we can rewrite $|\Psi(t)\rangle$ using the same notation inside the sum, $|\Psi(t)\rangle = \frac{1}{\sqrt{2}}\big[\,|\frac{N}{2}\rangle \otimes |\psi_{N/2}(t)\rangle + |-\frac{N}{2}\rangle \otimes |\psi_{-N/2}(t)\rangle\,\big]$. Using the new expression for $|\Psi(t)\rangle$, we can extract the terms in the sum corresponding to $m = \frac{N}{2}$ and $m = -\frac{N}{2}$, and rewrite $\rho(t)$ as

$$\rho(t) = \frac{p}{d}\sum_{m=-\frac{N}{2}+1}^{\frac{N}{2}-1} |m\rangle\langle m| \otimes |\psi_m(t)\rangle\langle\psi_m(t)| + \mathbf{v}\begin{pmatrix} \frac{1-p}{2} + \frac{p}{d} & \frac{1-p}{2} \\ \frac{1-p}{2} & \frac{1-p}{2} + \frac{p}{d} \end{pmatrix}\mathbf{v}^\dagger, \tag{4.40}$$

with $\mathbf{v} = \Big(\,|\frac{N}{2}\rangle\,|\psi_{N/2}(t)\rangle\,,\,|-\frac{N}{2}\rangle\,|\psi_{-N/2}(t)\rangle\,\Big)$ and $\mathbf{v}^\dagger$ the respective dual vectors (*bra*) written as a 1-column. The eigenvectors of $\rho(t)$ are $\frac{d}{p}\left(|m\rangle \otimes |\psi_m(t)\rangle\right)$ (for $m \in \{-\frac{N}{2}+, \cdots, \frac{N}{2}-1\}$), $|\Psi(t)\rangle$ and $|\Psi'(t)\rangle = \frac{1}{\sqrt{2}}\big[\,|\frac{N}{2}\rangle \otimes |\psi_{N/2}(t)\rangle - |-\frac{N}{2}\rangle \otimes |\psi_{-N/2}(t)\rangle\,\big]$.

Now that we have access to the eigenvectors and eigenvalues of the final state, we can readily calculate the QFI. Rather than continuing with analytical calculations, we now move on to numerical computations of the QFI.

Tetrahedron state

The computed QFI for the tetrahedron state is presented in Fig. 4.10. The same interpretation applies as for the GHZ state. We see in Fig. 4.10a that the QFI for small depolarization appears to remain constant with respect to gt for $G = J_z$ and $G = J_x$. For $G = J_z$, it reaches a maximum at $gt = \pi/2$, but in contrast to the GHZ state, this maximum is not restricted to $p = 1$. Again for $G = J_z$, the QFI corresponding to $gt = \pi/2$ is independent of p and attains its maximum value. In contrast, the GHZ state reaches its maximum QFI only when $p = 1$. However, Fig. 4.10b shows the same results as for the GHZ case.

Unitary before depolarization

We can now consider the same protocol as represented in Fig. 4.7 where we inverted the order of the unitary gate and the depolarizing channel. The circuit of interest is represented in Fig. 4.11. Let us derive the corresponding QFI. Assuming the probe input state is an N-qubit GHZ state (4.11) and the ancilla is the $|+\rangle$ state, the global input state is

$$\begin{aligned}
|\Psi(0)\rangle &= |\mathrm{GHZ}\rangle \otimes |+\rangle \\
&= \frac{1}{\sqrt{2}}\left(|0\rangle^{\otimes N} + |1\rangle^{\otimes N}\right) \otimes \frac{1}{\sqrt{2}}\left(|0\rangle_{\mathrm{A}} + |1\rangle_{\mathrm{A}}\right) \\
&= \frac{1}{2}\left(|0\rangle^{\otimes N}|0\rangle_{\mathrm{A}} + |0\rangle^{\otimes N}|1\rangle_{\mathrm{A}} + |1\rangle^{\otimes N}|0\rangle_{\mathrm{A}} + |1\rangle^{\otimes N}|1\rangle_{\mathrm{A}}\right) \\
&= \frac{1}{2}\left(|\phi_{00}\rangle + |\phi_{01}\rangle + |\phi_{10}\rangle + |\phi_{11}\rangle\right)\,.
\end{aligned} \tag{4.41}$$

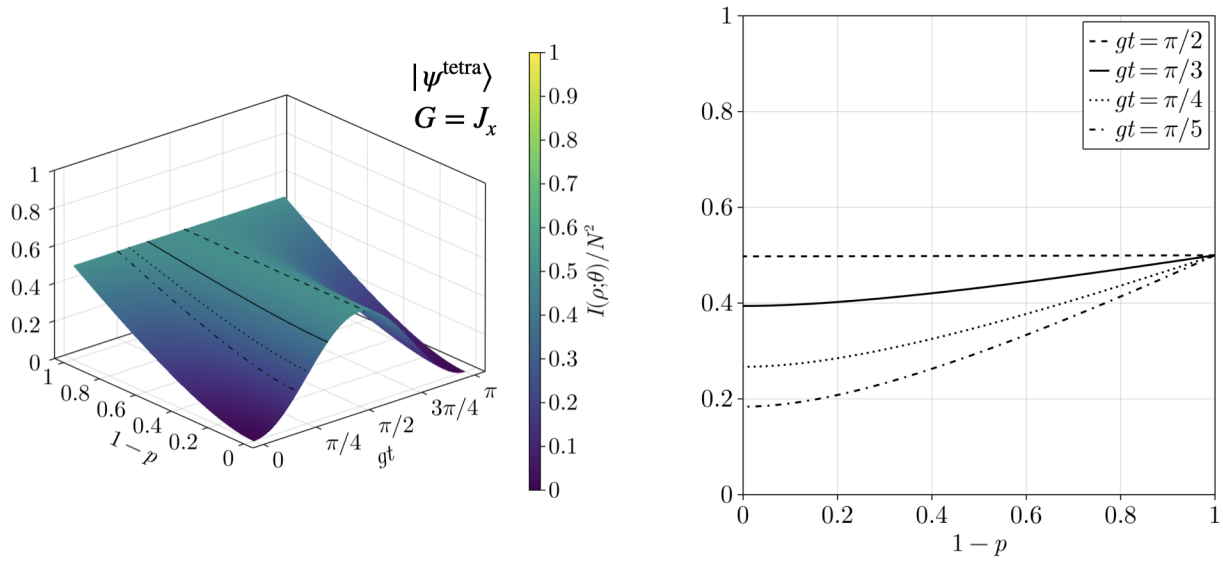

(a) QFI $I(\rho_\theta;\theta)$ for a rotation with $G = J_x$.

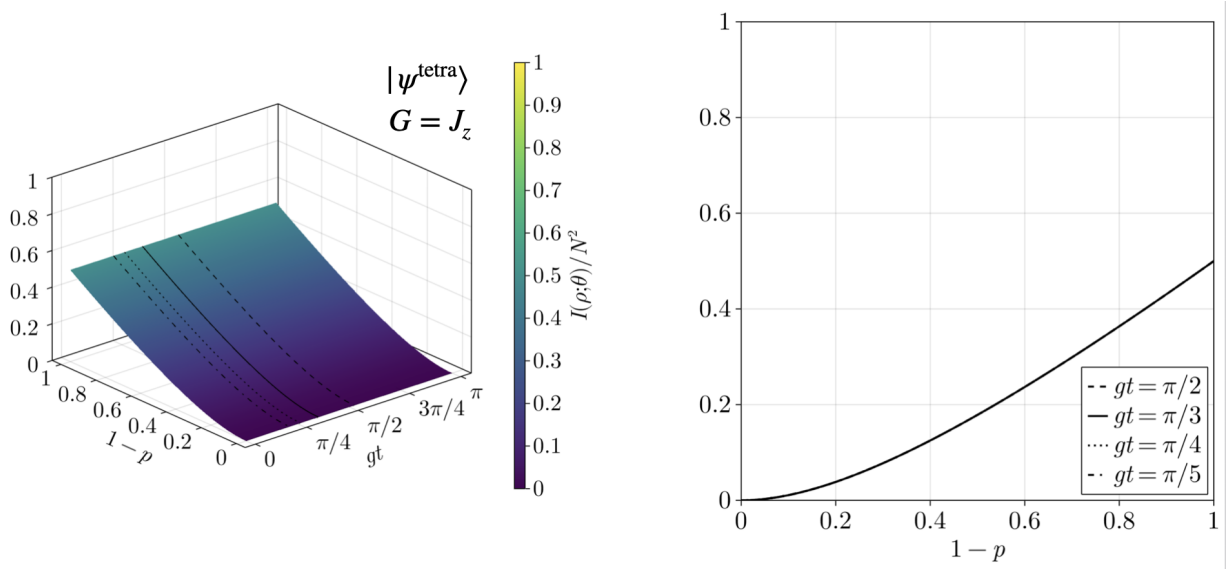

(b) QFI $I(\rho_\theta;\theta)$ for a rotation with $G = J_z$.

Figure 4.10: QFI of the tetrahedron state coupled to an ancilla as a function of the depolarization probability p and the application time gt of the unitary gate. The system's dimension is $d = 5$.

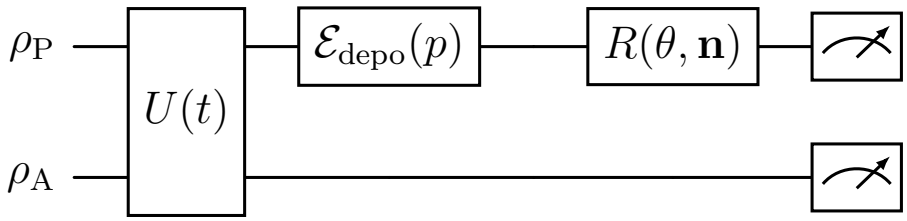

Figure 4.11: Phase estimation protocol using a unitary gate. ρ_{P} is the input probe state, and ρ_{A} is an ancillary qubit. A unitary gate $U(t)$ involving both states is applied. The probe state then undergoes depolarization via the depolarizing channel $\mathcal{E}_{\mathrm{depo}}$. The parameter θ is subsequently encoded onto the probe. Finally, both states can be measured.

where $|\phi_{ij}\rangle = |i\rangle^{\otimes N} |j\rangle_{\mathrm{A}}$ with $i, j = 0, 1$. $|\Psi(0)\rangle$ is a pure state, as both the GHZ state and the ancilla are individually pure. $|0\rangle^{\otimes N}$ and $|1\rangle^{\otimes N}$ are both eigenstates of J_z, with eigenvalues $+\frac{N}{2}$ and $-\frac{N}{2}$, respectively. Similarly, $|0\rangle_{\mathrm{A}}$ and $|1\rangle_{\mathrm{A}}$ are eigenstates of σ_z with eigenvalues $+1$ and -1, respectively. Thus we know that the Hamiltonian will be diagonal in the computational basis with 4 eigenstates and eigenvalues

$$\begin{aligned}
H|\phi_{00}\rangle = H|0\rangle^{\otimes N}|0\rangle_A &= \left(\omega_P \frac{N}{2} + \omega_A + g\frac{N}{2}\right)|0\rangle^{\otimes N}|0\rangle_A, \\
E_{00} &= \frac{N}{2}(\omega_P + g) + \omega_A, \\
H|\phi_{01}\rangle = H|0\rangle^{\otimes N}|1\rangle_A &= \left(\omega_P \frac{N}{2} - \omega_A - g\frac{N}{2}\right)|0\rangle^{\otimes N}|1\rangle_A, \\
E_{01} &= \frac{N}{2}(\omega_P - g) - \omega_A, \\
H|\phi_{10}\rangle = H|1\rangle^{\otimes N}|0\rangle_A &= \left(-\omega_P \frac{N}{2} + \omega_A - g\frac{N}{2}\right)|1\rangle^{\otimes N}|0\rangle_A, \\
E_{10} &= -\frac{N}{2}(\omega_P + g) + \omega_A, \\
H|\phi_{11}\rangle = H|1\rangle^{\otimes N}|1\rangle_A &= \left(-\omega_P \frac{N}{2} - \omega_A + g\frac{N}{2}\right)|1\rangle^{\otimes N}|1\rangle_A, \\
E_{11} &= -\frac{N}{2}(\omega_P - g) - \omega_A.
\end{aligned}$$

The unitary evolution applies phase factors to each eigenstate

$$U(t)|\phi_{ij}\rangle = e^{-itE_{ij}}|\phi_{ij}\rangle \quad \text{for } i, j = 0, 1\ . \tag{4.42}$$

Therefore, after the unitary, the state will become

$$\begin{aligned}
|\Psi(t)\rangle = U(t)|\Psi(0)\rangle = \frac{1}{2}\Big(&e^{-it\left(\frac{N}{2}(\omega_P+g)+\omega_A\right)}|0\rangle^{\otimes N}|0\rangle_{\mathrm{A}} + e^{-it\left(\frac{N}{2}(\omega_P-g)-\omega_A\right)}|0\rangle^{\otimes N}|1\rangle_{\mathrm{A}} \\
&+e^{-it\left(-\frac{N}{2}(\omega_P+g)+\omega_A\right)}|1\rangle^{\otimes N}|0\rangle_{\mathrm{A}} + e^{-it\left(\frac{N}{2}(\omega_P-g)+\omega_A\right)}|1\rangle^{\otimes N}|1\rangle_{\mathrm{A}}\Big)\ .
\end{aligned} \tag{4.43}$$

Since $|\Psi(t)\rangle$ is a pure state, we can follow the same developments as for the protocol shown in Fig. 4.3, considering that the input state is $|\Psi(t)\rangle$. This gives us the following QFI

$$I(\rho_\theta, \theta) = \frac{4(1-p)^2}{1-p+\frac{2p}{d}} \mathrm{Var}[G, |\Psi(t)\rangle] \, . \tag{4.44}$$

Numerical computations show that $\mathrm{Var}[G, |\Psi(t)\rangle]$ is exactly the same as for the GHZ state $\mathrm{Var}[G, |\mathrm{GHZ}\rangle]$. Similar results are obtained when using the tetrahedron state as the input state; however, we will not carry out the corresponding calculations in this paper. Therefore, we conclude that applying a unitary before the depolarization step does not provide any advantage in a parameter estimation protocol.

4.3 Axis misspecification channel

Sometimes, in an estimation procedure, when we want to estimate a rotation angle, the axis is either partially known (in the sense that we know a solid angle Ω in which it lies) or sometimes completely unknown. This scenario can be simulated by what we will call an *axis misspecification (AM) channel* $\mathcal{E}_{\mathrm{AM}}(\rho)$.

The goal is to simulate uncertainty on the rotation axis by averaging on multiple unit vectors $\mathbf{n}_k$, each randomly sampled from a solid angle Ω centered around the original axis $\mathbf{n}$. For each sampled direction $\mathbf{n}_k$, a unitary rotation operator $U(\theta) = e^{-i\theta \mathbf{n}_k \cdot \mathbf{J}}$ is constructed, where $\mathbf{J} = (J_x, J_y, J_z)$ and J_x, J_y, J_z are the collective spin operators for an N-particle system. The channel then applies each unitary rotation to the input state ρ and outputs the mixture over all such rotated states. The QFI is then computed using the Bures distance formula between the input state ρ and the mixed state $\mathcal{E}_{\mathrm{AM}}(p)$. Since this procedure involves randomness, the channel must be computed multiple times and the results averaged. We will denote the average QFI as $\overline{I(|\psi\rangle\,;\theta)}^{\Omega}$, with the solid angle Ω. Numerically, the averaging is done as $\overline{I(|\psi\rangle\,;\theta)}^{\Omega} = \frac{1}{n_{\mathrm{rep}}} \sum_{n_{\mathrm{rep}}} 4 \frac{D_B^2(\rho, \mathcal{E}_{\mathrm{AM}}(\rho))}{\mathrm{d}\theta^2}$, with n_{rep} the number of repetitions.

4.3.1 Preliminary analysis

We will begin our analysis with an example of how the channel is used. To do so, we will analyse the evolution of the average QFI of a GHZ state as a function of the solid angle Ω. Figure 4.13 shows the numerical simulations for the three directions $\hat{x}$, $\hat{y}$, and $\hat{z}$ ($\hat{i}$ is the direction of the i-axis), for a large number of random vectors and repetitions ($10,000$ random vectors and $1,000$ repetitions). In these data, the standard deviations all converge to zero, provided that the number of random vectors and repetitions is sufficiently high. Our computations show that the results for $\mathbf{n} = \hat{x}$ and $\mathbf{n} = \hat{y}$ are identical. Next, it is easily observed that the curves appear to be quadratic. A fit with a second-order polynomial confirms this intuition. In fact, in the following, we will present a calculation that yields a general quadratic expression valid beyond this particular case. We have the following limiting cases: $\Omega = 0$ corresponds to the case where the rotation axis is known. It is therefore natural that $\overline{I(|\psi\rangle\,;\theta)}^{\Omega} = I(|\psi\rangle\,;\theta)$. Similarly, when $\Omega = 4\pi$, the initially considered axis no longer has any influence; then we are in the case where we do not have information about the rotation direction. Therefore, it is clear that for the same state, $\overline{I(|\psi\rangle;\theta)}^{\Omega}$ remains the same regardless of the initial axis. Surprisingly, we observe that the QFI is independent of the chosen axis for $\Omega = 2\pi$, which corresponds to a solid angle covering half of the sphere.

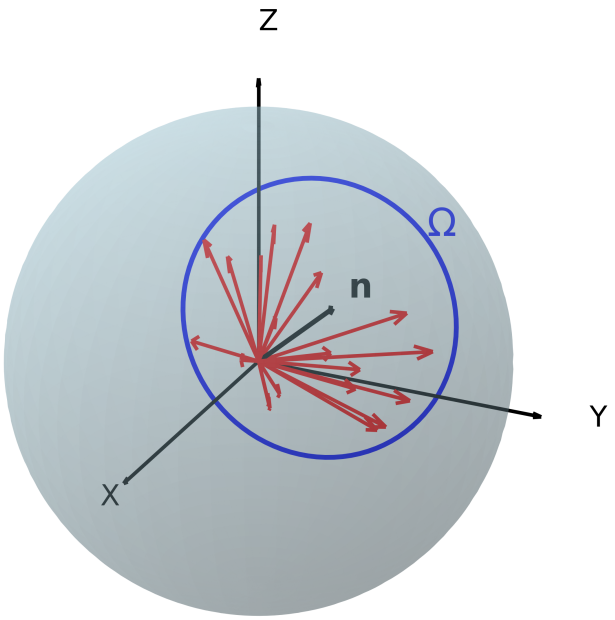

Figure 4.12: Visual representation of an axis misspecification (AM) with $\mathbf{n} = (\hat{x} + \hat{y} + \hat{z})/\sqrt{3}$ (black arrow), $\Omega = 1.0$ (blue circle) and 20 random vectors (red arrows).

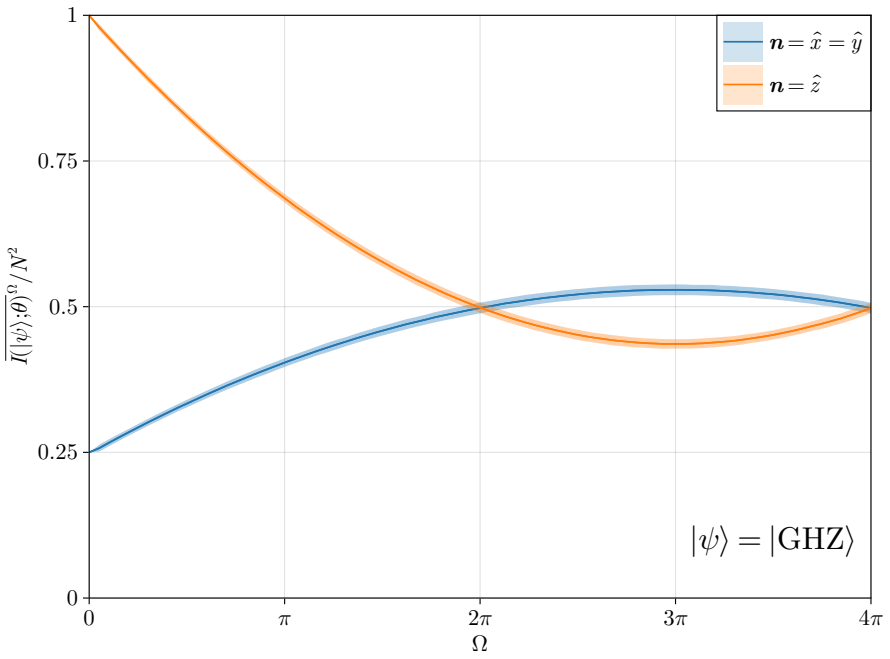

Figure 4.13: Evolution of the normalized average QFI, $\overline{I(|\psi\rangle;\theta)}^{\Omega}/N^2$, of a GHZ state as a function of the solid angle. Ω is chosen along the axis $\mathbf{n} = \hat{x}$ or $\mathbf{n} = \hat{y}$ (blue solid line) and $\mathbf{n} = \hat{z}$ (orange solid line). The average is computed over 1,000 repetitions, each consisting of 10,000 random vectors. We also plot uncertainty bars with a width of three times the standard deviation.

4.3.2 Analytical solution

In order to verify the validity of our simulations, we can try to derive an analytical expression for the QFI.

Pure case

The QFI for pure states with respect to a rotation along the axis $\mathbf{n}$ reads

$$\frac{I\big(\,|\psi\rangle\,;\theta\big)}{4Nt^2} = \mathrm{Var}[\mathbf{n}\cdot\mathbf{J},|\psi\rangle] = \ \langle\psi|\,(\mathbf{n}\cdot\mathbf{J})^2\,|\psi\rangle - \langle\psi|\,\mathbf{n}\cdot\mathbf{J}\,|\psi\rangle^2\,. \tag{4.45}$$

Let us assume that the axis of rotation is parallel to the z axis with a misspecification that we have modeled using a disc on the sphere centered on the z axis with a solid angle $\Omega = 2\pi(1-\cos\omega)$, where ω is the maximum polar angle. We can now calculate the average QFI with respect to this solid angle. The set of unit vectors associated to this solid angle can be parametrized by

$$\mathbf{n} = R(\hat{z},\phi)R(\hat{y},\vartheta)\hat{z}\ , \tag{4.46}$$

with $\phi\in[0,2\pi]$, $\vartheta\in[0,\omega]$ and R are the 3×3 rotation matrices

$$R(\hat{y},\vartheta) = \begin{pmatrix} \cos\vartheta & 0 & -\sin\vartheta \\ 0 & 1 & 0 \\ \sin\vartheta & 0 & \cos\vartheta \end{pmatrix}, \qquad R(\hat{z},\phi) = \begin{pmatrix} \cos\phi & \sin\phi & 0 \\ -\sin\phi & \cos\phi & 0 \\ 0 & 0 & 1 \end{pmatrix}\ . \tag{4.47}$$

We omit for now the factor $4Nt^2$ From the QFI (4.45), and we formally define

$$\overline{I\big(\,|\psi\rangle\,;\theta\big)}^{\Omega} \overset{\text{def}}{=} \frac{1}{\Omega}\int_0^{2\pi}\mathrm{d}\phi\int_0^{\omega}\sin\vartheta\ \mathrm{d}\vartheta\ \mathrm{Var}[\mathbf{n}\cdot\mathbf{J},|\psi\rangle]\ . \tag{4.48}$$

If we expand the variance, we observe that the latter equation is equal to

$$\sum_{a,b=1}^{3} n_a n_b\Big(\,\langle\psi|\,J_aJ_b\,|\psi\rangle - \langle\psi|\,J_a\,|\psi\rangle\,\langle\psi|\,J_b\,|\psi\rangle\,\Big), \tag{4.49}$$

where the integral will affect only the term n_an_b. By doing the integral, we obtain that

$$\frac{1}{\Omega}\int_0^{2\pi}\mathrm{d}\phi\int_0^{\omega}\sin\theta n_an_b = \delta_{ab}\times\begin{cases} \frac{1-g(\omega)}{2} & \text{if } a=1 \text{ or } 2 \\ g(\omega) & \text{if } a=3 \end{cases}\ , \tag{4.50}$$

and therefore

$$\overline{I\big(\,|\psi\rangle\,;\theta\big)}^{\Omega} = \frac{1}{2}\Big[2g(\omega)\mathrm{Var}[J_z,|\psi\rangle] + \big(1-g(\omega)\big)\big(\mathrm{Var}[J_x,|\psi\rangle] + \mathrm{Var}[J_y,|\psi\rangle]\big)\Big]\ , \tag{4.51}$$

with

$$g(\omega) = \frac{1+\cos\omega+\cos^2\omega}{3}\ . \tag{4.52}$$

In particular, $2g(\omega)\geq 1-g(\omega)$ for $\omega\in[0,\pi/2]$. Using $\omega = \arccos\left(1-\frac{\Omega}{2\pi}\right)$, we easily obtain

$$g(\Omega) = 1 - \frac{\Omega}{2\pi} + \frac{(\frac{\Omega}{2\pi})^2}{3}\ . \tag{4.53}$$

Let $A = \mathrm{Var}[J_z, |\psi\rangle]$ and $B = \mathrm{Var}[J_x, |\psi\rangle] + \mathrm{Var}[J_y, |\psi\rangle]$. Inserting Eq. (4.53) into Eq. (4.51) and using A and B, we express $\overline{I\big(|\psi\rangle\,;\theta\big)}^{\Omega}$ as a quadratic function of Ω

$$\overline{I\big(|\psi\rangle\,;\theta\big)}^{\Omega} = A + \frac{1}{4\pi}(-2A+B)\,\Omega + \frac{1}{8\pi^2}\left(\frac{2}{3}A - \frac{1}{3}B\right)\Omega^2\,. \tag{4.54}$$

The discriminant of Eq. (4.54) is

$$\Delta = \left(\frac{-2A+B}{4\pi}\right)^2 - 4A\cdot\left[\frac{1}{8\pi^2}\left(\frac{2}{3}A - \frac{1}{3}B\right)\right] \tag{4.55}$$

After expanding and simplifying, we find

$$\Delta = \frac{(-2A+B)^2}{16\pi^2} - \frac{A}{2\pi^2}\left(\frac{2}{3}A - \frac{1}{3}B\right) = \frac{-\frac{4}{3}A^2 - \frac{4}{3}AB + B^2}{16\pi^2}\,. \tag{4.56}$$

Mixed case

Similarly, if the initial state is a mixed state we have

$$I(\rho\,;\theta) = 2\sum_{l,m=1}^{r}\lambda_{lm}|\,\langle\psi_l|\,\mathbf{n}\cdot\mathbf{J}\,|\psi_m\rangle\,|^2 = 2\sum_{l,m=1}^{r}\lambda_{lm}\sum_{a,b=1}^{3} n_a n_b\,\langle\psi_l|\,J_a\,|\psi_m\rangle\,\langle\psi_m|\,J_b\,|\psi_l\rangle \tag{4.57}$$

with

$$\lambda_{lm} = \begin{cases} 0 & \text{if } p_m = p_l = 0 \\ \frac{(p_m - p_l)^2}{p_m + p_l} & \text{otherwise} \end{cases}\,. \tag{4.58}$$

For the average over the AM error, we can do the same calculation, and we obtain

$$\overline{I(\rho\,;\theta)}^{\Omega} = \sum_{l,m=1}^{r}\lambda_{lm}\Big[2g(\omega)|\,\langle\psi_l|\,J_z\,|\psi_m\rangle\,|^2 + \big(1-g(\omega)\big)\big(|\,\langle\psi_l|\,J_x\,|\psi_m\rangle\,|^2 + |\,\langle\psi_l|\,J_y\,|\psi_m\rangle\,|^2\big)\Big]. \tag{4.59}$$

4.3.3 Optimal states

We can now try to answer the following question: What is the optimal probe state to estimate a rotation angle in a protocol where the rotation axis is either partially known (*i.e.*, the value of Ω is known and $0 < \Omega < 4\pi$), or completely unknown (*i.e.*, $\Omega = 4\pi$)?

To this end, we consider a non-exhaustive list of states that reach the Heisenberg limit in the case where the rotation axis is known, in order to see whether they retain this property in our scenario. In addition, we also consider classical states to clearly highlight their inefficiency compared to entangled states. We will therefore consider the GHZ state, the tetrahedron state, the coherent state, and the maximally mixed state. Figure 4.14 shows the average QFI for the considered states.

To begin with, the GHZ state shows the highest performance, $\overline{I\big(|\psi\rangle\,;\theta\big)}^{\Omega} = N^2$, when the initial axis is aligned with the z-axis. It also remains the most useful state for $\Omega \in [0, 2\pi[$. However, it exhibits a strong dependence on Ω (see Figure 4.14). We also see that it becomes less performant than the tetrahedron state for $\Omega \in]2\pi, 4\pi[$. Additionally, the tetrahedron state maintains a constant average QFI around 0.5 regardless of Ω or the axis, highlighting their

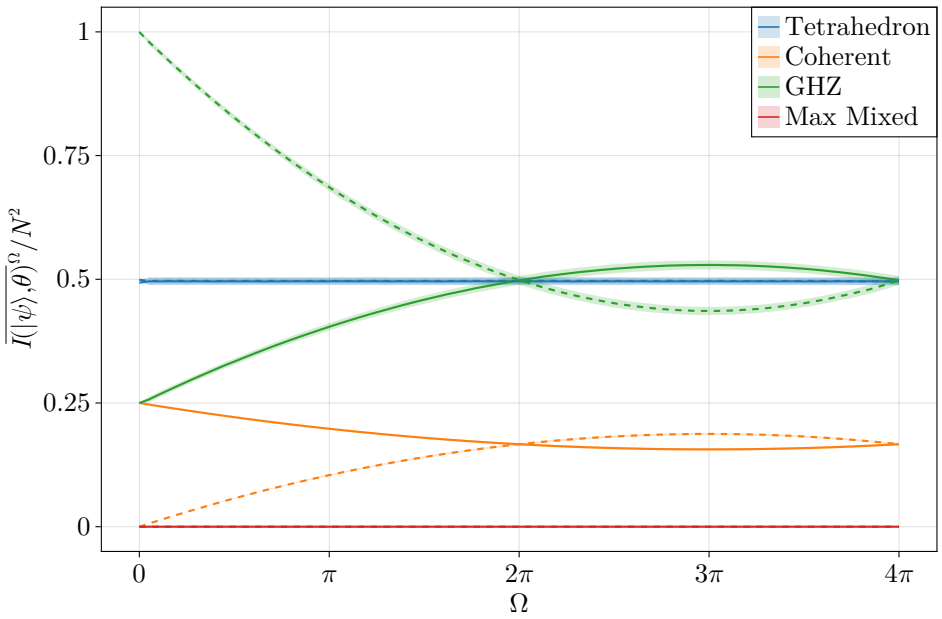

Figure 4.14: Average QFI, $\overline{I\left(|\psi\rangle;\theta\right)}^{\Omega}$, as a function of the solid angle Ω for different states. The initial axes considered are oriented with respect to $\mathbf{n} = \hat{x}$ (solid line) and $\mathbf{n} = \hat{z}$ (dashed line), respectively. We also plot uncertainty bars with a width of 3 standard deviations.

State	**Sensitivity**	**Robustness under AM**	**Axis Dependence**	**Practical Use**
GHZ	High w.r.t to $\hat{z}$ but low for $\hat{x}$	Low	High	Optimal under precise control
Tetrahedron	Moderate and indep of $\mathbf{n}$	High	Low	Best for unknown/noisy settings
Coherent	Low w.r.t to $\hat{x}$ and vanishing for $\hat{z}$	Moderate	Moderate	Baseline (classical) performance
Max. Mixed	None	N/A	None	Not useful

Table 4.2: Comparison of quantum states from a metrological perspective.

directional isotropy and robustness. These properties make them particularly well-suited for metrological tasks where the parameter's encoding direction is unknown or subject to noise. Coherent states, being separable product states, display low QFI values and moderate axis dependence, thus offering limited metrological advantage over classical strategies. Finally, the maximally mixed state yields a vanishing QFI, reflecting its complete lack of information about the parameter and confirming its unsuitability for precision measurements. The full analysis is summarized in Table 4.2.

Lastly, let us now focus on the specific case $\Omega = 4\pi$. Figure 4.15 shows the average QFI for $\Omega = 4\pi$ for GHZ, anticoherent, and coherent states for various system sizes N. Two clearly different trends can be easily observed. First, the coherent states follow a trend proportional to $\frac{2}{3}N$. Moreover, the anticoherent and GHZ states follow a trend proportional to $\frac{2}{3}N(N+2)$. This result is in agreement with that of G. Tóth *et al.* in [65]. They prove that the average QFI of a separable state is bounded by

$$\overline{I\left(|\psi\rangle;\theta\right)}^{\Omega} \leq \frac{2}{3}N\ . \tag{4.60}$$

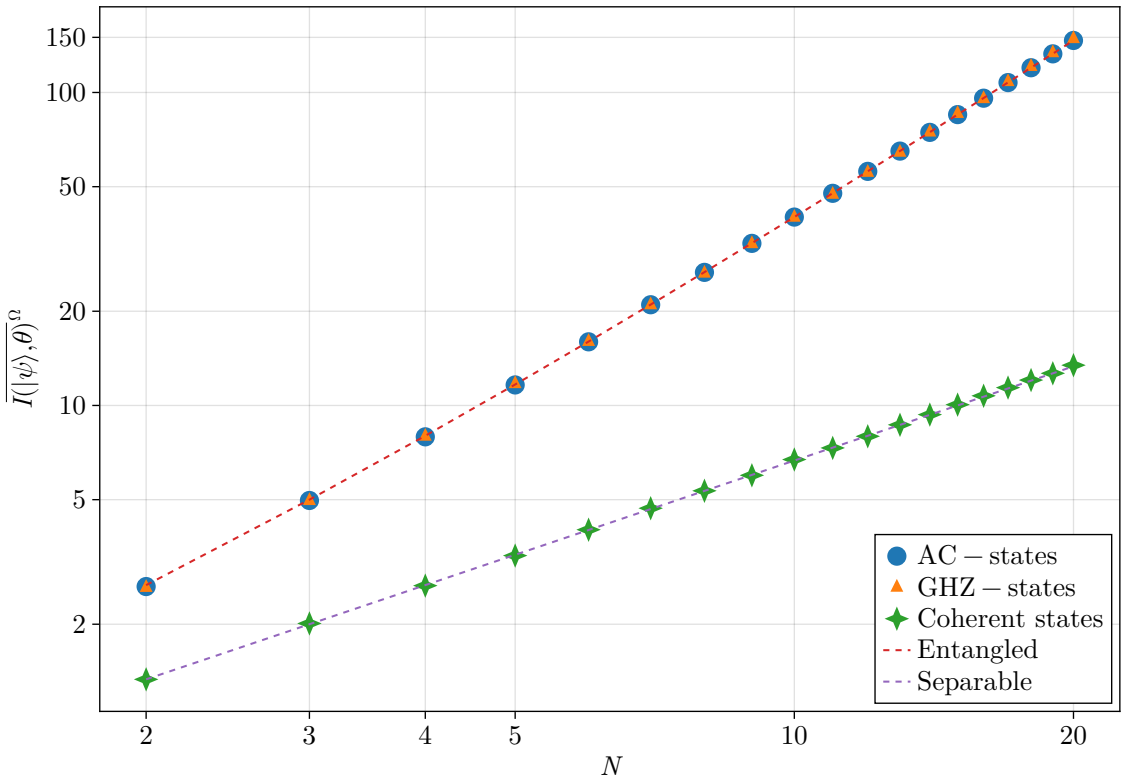

Figure 4.15: Average QFI for $\Omega = 4\pi$ for anticoherent (blue circles), GHZ (orange triangles), and coherent (green stars) states, plotted as a function of the number of particles N in the system. We also show the upper bound of the average QFI provided in [65]. The upper bounds for entangled states (red dashed line) and separable states (purple dashed line) are given by $\overline{I\big(\,|\psi\rangle\,;\theta\big)}^{\Omega} = \frac{2}{3}N(N+2)$ and $\overline{I\big(\,|\psi\rangle\,;\theta\big)}^{\Omega} = \frac{2}{3}N$, respectively. Anticoherent states are provided by J. Martin in [66].

In the same idea, they prove that for an entangled state, the average QFI is bounded by

$$\overline{I\big(\,|\psi\rangle\,;\theta\big)}^{\Omega} \leq \frac{2}{3}N(N+2)\,. \tag{4.61}$$

Figure 4.15 shows that the states saturate their corresponding inequality. However, each average QFI is smaller than the bound for a given direction.

Conclusion

In this master's thesis, we explore the theoretical foundations and practical implications of quantum parameter estimation theory, with a particular focus on quantum metrology under noisy conditions.

We began in Chapter 1 by introducing the classical problem of parameter estimation. We formally defined the concept of an estimator and derived the Cramér-Rao Theorem, in which Fisher information $\mathrm{J}(\mu_\theta;\theta)$ naturally appears as a measure of information about a parameter contained in a probability distribution.

Then, in Chapter 2, we extended the classical theory of parameter estimation to the quantum domain. There, we presented the quantum version of the Cramér-Rao theorem, in which the Quantum Fisher Information $I(\rho_\theta\,;\,\theta)$ appears, which is the quantum analogue of the classical Fisher information. Just as the Fisher information quantifies the amount of information extractable from a probability distribution, the Quantum Fisher Information quantifies the usefulness of a quantum state, understood as its ability to maximize the achievable precision in a measurement protocol. We also developed several methods to compute the QFI, some of which are more practical than others depending on the context.

Chapter 3 allowed us to introduce the notions of the Standard Quantum Limit (SQL) and Heisenberg Limit (HL). We explained the distinction between scenarios that allow one to reach the HL (Quantum-Classical and Quantum-Quantum) and those in which one cannot surpass the SQL (Classical-Classical and Classical-Quantum). We also showed that in a Mach-Zehnder interferometer, the NOON state achieves the HL, unlike the coherent state, which only reaches the SQL. Furthermore, we presented the role of spin squeezing in the estimation of a rotation angle. To conclude this chapter, we discussed the case of magnetic field estimation and showed that, through an anti-evolution strategy, it is possible to reach the maximum precision in the simultaneous estimation of the three rotation parameters: the field strength B and the two angles θ and ϕ that define its direction.

Finally, Chapter 4 forms the main part of our personal contribution. The objective was to analyze the influence of noise on certain measurement protocols through the lens of the QFI. To this end, we began by formally defining noise mechanisms using quantum channels. We then focused on the depolarizing channel and studied the behavior of the QFI in a simple protocol subject to this channel. We succeeded in finding the analytical expression of the QFI in the most simple protocol (see Eq. (4.19).

From there, we developed a more sophisticated protocol that involves additional coupling, through a ZZ interaction, between the probe state and an ancillary qubit. This protocol allowed us to mitigate the loss of information induced by depolarization. We also examined

and analyzed the case of estimating a rotation angle around a partially known or completely unknown axis. In this context, we derived an analytical expression for the QFI that depends on the information available on the axis quantified by a solid angle Ω (see Eq. (4.54)). We also performed a comparative analysis of the performance of several quantum states commonly used in estimation protocols.

Although the models studied in this work provide valuable insight, several limitations remain. The analysis assumes pure initial states and/or focuses primarily on depolarization noise and axis misspecification. In practice, other decoherence mechanisms, mixed input states, and realistic constraints on measurements should ideally be taken into account. Furthermore, our approach considers static measurement strategies and does not incorporate feedback or adaptive protocols, which could further improve the precision of the estimation.

The original research carried out in Chapter 4 serves as a basis to study more general noise models, such as those found in correlated or non-Markovian environments. In order to facilitate the experimental validation of the theoretical predictions presented in this work, on platforms such as trapped ions, cold atoms, or superconducting qubits used for quantum metrology, it would also be necessary to study the optimal measurement protocols arising from our QFI analyses and associated with the identified optimal states.

Ultimately, this master's thesis further highlights the subtle interplay between noise, entanglement and measurement strategy in quantum metrology. Our results thus contribute to the broader effort to design quantum-enhanced protocols and technologies for precision sensing.

Bibliography

[1] R. S. Shankland, *Michelson-Morley Experiment*, American Journal of Physics **32**, 16 (1964).

[2] R. Schnabel, N. Mavalvala, D. E. McClelland, and P. K. Lam, *Quantum metrology for gravitational wave astronomy*, Nature Communications **1**, 121 (2010), Publisher: Nature Publishing Group.

[3] F. Biraben et al., Precision Spectroscopy of Atomic Hydrogen, in *The Hydrogen Atom*, edited by R. Beig et al., volume 570, pages 17–41, Springer Berlin Heidelberg, Berlin, Heidelberg, 2001, Series Title: Lecture Notes in Physics.

[4] S. G. Karshenboim, *Precision physics of simple atoms: QED tests, nuclear structure and fundamental constants*, Physics Reports **422**, 1 (2005).

[5] A. Bernatskyi and V. Khaskin, *The history of the creation of lasers and analysis of the impact of their application in the material processing on the development of certain industries*, History of science and technology **11**, 125 (2021).

[6] J. Aasi and et al (LIGO Scientific Collaboration), *Enhanced sensitivity of the LIGO gravitational wave detector by using squeezed states of light*, Nature Photonics **7**, 613 (2013).

[7] C. Degen, *Quantum sensing*, Reviews of Modern Physics **89** (2017).

[8] M. Tsang, *Fundamental Quantum Limit to Waveform Estimation*, Physical Review Letters **106** (2011).

[9] H. Katori, *Optical lattice clocks and quantum metrology*, Nature Photonics **5**, 203 (2011).

[10] J. Brask, R. Chaves, and J. Kołodyński, *Improved Quantum Magnetometry beyond the Standard Quantum Limit*, Physical Review X **5**, 031010 (2015).

[11] N. Aslam et al., *Quantum sensors for biomedical applications*, Nature Reviews Physics **5**, 157 (2023).

[12] P. H. Cutler and A. A. Lucas, *Quantum Metrology and Fundamental Physical Constants*, Number 98 in NATO Advanced Science Institutes Series, Series B: Physics, Springer US, Boston, MA s.l, 1983.

[13] S. Xiao et al., *Orbital angular momentum-enhanced measurement of rotation vibration using a Sagnac interferometer*, Optics Express **26**, 1997 (2018).

[14] M. Bhattacharya, *Rotational cavity optomechanics*, Journal of the Optical Society of America B **32**, B55 (2015).

[15] E. Oh et al., *Perspective on Quantum Sensors from Basic Research to Commercial Applications*, AIAA Journal **62**, 4029 (2024).

[16] L. Pezzè, A. Smerzi, M. K. Oberthaler, R. Schmied, and P. Treutlein, *Quantum metrology with nonclassical states of atomic ensembles*, Reviews of Modern Physics **90**, 035005 (2018), Publisher: American Physical Society.

[17] D. J. Wineland, J. J. Bollinger, W. M. Itano, F. L. Moore, and D. J. Heinzen, *Spin squeezing and reduced quantum noise in spectroscopy*, Physical Review A **46**, R6797 (1992).

[18] D. J. Wineland, J. J. Bollinger, W. M. Itano, and D. J. Heinzen, *Squeezed atomic states and projection noise in spectroscopy*, Physical Review A **50**, 67 (1994).

[19] Y. A. Yang et al., *Minute-scale Schrödinger-cat state of spin-5/2 atoms*, Nature Photonics **19**, 89 (2025).

[20] K. Liu et al., *Squeezing-enhanced rotating-angle measurement beyond the quantum limit*, Applied Physics Letters **113**, 261103 (2018).

[21] A. Kolmogorov, A. Bharucha-Reid, and N. Morrison, *Foundations of the Theory of Probability: Second English Edition*, Dover Books on Mathematics, Dover Publications, 2018.

[22] G. Casella and R. Berger, *Statistical Inference*, Duxbury Resource Center, 2001.

[23] J. O. Berger, *Statistical Decision Theory and Bayesian Analysis*, Springer Series in Statistics, Springer, New York, NY, 1985.

[24] J. M. E. Fraisse, *New concepts in quantum-metrology: From coherent averaging to Hamiltonian extensions*, PhD thesis, Universität Tübingen, 2018.

[25] C. W. Helstrom, *Quantum detection and estimation theory*, Journal of Statistical Physics **1**, 231 (1969).

[26] H. Cramér, *Mathematical Methods of Statistics*, Princeton University Press, Princeton, NJ, reprint edition edition, 1999.

[27] S. Nicolay, *Analyse mathématique: fonctions définies sur une partie de la droite réelle cours avec exercices corrigés et exercices d'approfondissement*, Références sciences, Ellipses, Paris, 2018.

[28] M. Szczykulska, T. Baumgratz, and A. Datta, *Multi-parameter Quantum Metrology*, Advances in Physics: X **1** (2016).

[29] S. L. Braunstein and C. M. Caves, *Statistical distance and the geometry of quantum states*, Physical Review Letters **72**, 3439 (1994), Publisher: American Physical Society.

[30] M. G. A. Paris, *QUANTUM ESTIMATION FOR QUANTUM TECHNOLOGY*, International Journal of Quantum Information **07**, 125 (2009).

[31] J. Liu, X.-X. Jing, W. Zhong, and X.-G. Wang, *Quantum Fisher Information for Density Matrices with Arbitrary Ranks*, Communications in Theoretical Physics **61**, 45 (2014).

[32] E. Serrano-Ensástiga, C. Chryssomalakos, and J. Martin, *Quantum metrology of rotations with mixed spin states*, Physical Review A **111**, 022435 (2025).

[33] U. Marzolino and T. Prosen, *Quantum metrology with nonequilibrium steady states of quantum spin chains*, Physical Review A **90**, 062130 (2014), Publisher: American Physical Society.

[34] J. Liu, J. Chen, X.-X. Jing, and X. Wang, *Quantum Fisher information and symmetric logarithmic derivative via anti-commutators*, Journal of Physics A: Mathematical and Theoretical **49**, 275302 (2016), arXiv:1501.04290 [quant-ph].

[35] B. N. Datta, NUMERICAL SOLUTIONS AND CONDITIONING OF LYAPUNOV AND SYLVESTER EQUATIONS, in *Numerical Methods for Linear Control Systems*, pages 245–303, Elsevier, 2004.

[36] J. Liu, H.-N. Xiong, F. Song, and X. Wang, *Fidelity susceptibility and quantum Fisher information for density operators with arbitrary ranks*, Physica A: Statistical Mechanics and its Applications **410**, 167 (2014).

[37] Z. Ji, G. Wang, R. Duan, Y. Feng, and M. Ying, *Parameter Estimation of Quantum Channels*, IEEE Transactions on Information Theory **54**, 5172 (2008).

[38] A. Fujiwara, *Quantum channel identification problem*, Physical Review A **63**, 042304 (2001).

[39] I. Bengtsson and K. Zyczkowski, *Geometry of Quantum States: An Introduction to Quantum Entanglement*, Cambridge University Press, Cambridge, 2006.

[40] S. J. Akhtarshenas, *An explicit computation of the Bures metric over the space of N - dimensional density matrices*, Journal of Physics A: Mathematical and Theoretical **40**, 11333 (2007).

[41] R. Jozsa, *Fidelity for Mixed Quantum States*, Journal of Modern Optics **41**, 2315 (1994).

[42] L. J. Fiderer, T. Tufarelli, S. Piano, and G. Adesso, *General Expressions for the Quantum Fisher Information Matrix with Applications to Discrete Quantum Imaging*, PRX Quantum **2**, 020308 (2021).

[43] V. Giovannetti, S. Lloyd, and L. Maccone, *Quantum Metrology*, Physical Review Letters **96**, 010401 (2006), Publisher: American Physical Society.

[44] T. Popoviciu, *Sur les équations algébriques ayant toutes leurs racines réelles*, Mathematica **9**, 20 (1935).

[45] C. M. Caves, *Quantum-mechanical noise in an interferometer*, Phys. Rev. D **23**, 1693 (1981).

[46] V. Giovannetti, S. Lloyd, and L. Maccone, *Advances in quantum metrology*, Nature Photonics **5**, 222 (2011), Publisher: Nature Publishing Group.

[47] J. P. Dowling and K. P. Seshadreesan, *Quantum Optical Technologies for Metrology, Sensing, and Imaging*, Journal of Lightwave Technology **33**, 2359 (2015), Conference Name: Journal of Lightwave Technology.

[48] J. C. Matthews et al., *Towards practical quantum metrology with photon counting*, npj Quantum Information **2**, 1 (2016), Publisher: Nature Publishing Group.

[49] S. Sadugol and L. Kaplan, *Quantum metrology in a lossless Mach–Zehnder interferometer using entangled photon inputs for a sequence of non-adaptive and adaptive measurements*, AVS Quantum Science **5**, 014407 (2023).

[50] F. T. Arecchi, *Atomic Coherent States in Quantum Optics*, Physical Review A **6**, 2211 (1972).

[51] A. S. Sørensen and K. Mølmer, *Entanglement and Extreme Spin Squeezing*, Physical Review Letters **86**, 4431 (2001).

[52] L. Rondin et al., *Magnetometry with nitrogen-vacancy defects in diamond*, Reports on Progress in Physics **77**, 056503 (2014).

[53] J. M. Schloss, J. F. Barry, M. J. Turner, and R. L. Walsworth, *Simultaneous Broadband Vector Magnetometry Using Solid-State Spins*, Physical Review Applied **10**, 034044 (2018).

[54] B.-B. Li et al., *Quantum enhanced optomechanical magnetometry*, Optica **5**, 850 (2018).

[55] D. Sheng, S. Li, N. Dural, and M. V. Romalis, *Subfemtotesla Scalar Atomic Magnetometry Using Multipass Cells*, Physical Review Letters **110**, 160802 (2013).

[56] J. Liu, H. Yuan, X.-M. Lu, and X. Wang, *Quantum Fisher information matrix and multiparameter estimation*, Journal of Physics A: Mathematical and Theoretical **53**, 023001 (2020).

[57] Z. Hou et al., *Control-Enhanced Sequential Scheme for General Quantum Parameter Estimation at the Heisenberg Limit*, Physical Review Letters **123**, 040501 (2019).

[58] H. Yuan, *Sequential Feedback Scheme Outperforms the Parallel Scheme for Hamiltonian Parameter Estimation*, Physical Review Letters **117**, 160801 (2016).

[59] V. Jagadish and F. Petruccione, *An Invitation to Quantum Channels*, Quanta **7**, 54 (2018).

[60] H.-P. Breuer and F. Petruccione, *The Theory of Open Quantum Systems*, Oxford University PressOxford, 1 edition, 2007.

[61] J. Martin, S. Weigert, and O. Giraud, *Optimal Detection of Rotations about Unknown Axes by Coherent and Anticoherent States*, Quantum **4**, 285 (2020), Publisher: Verein zur Förderung des Open Access Publizierens in den Quantenwissenschaften.

[62] Y. Mafi, P. Kazemikhah, A. Kookani, H. Aghababa, and M. Kolahdouz, *Generalized GHZ entanglement states for optimal rotation detection of quantum spin systems using majorana representation*, Physica Scripta **99**, 035206 (2024).

[63] A. Z. Goldberg and D. F. V. James, *Quantum-limited Euler angle measurements using anticoherent states*, Phys. Rev. A **98**, 032113 (2018).

[64] P. Chen and J. Jing, *Qubit-assisted quantum metrology under a time-reversal strategy*, Physical Review A **110**, 062425 (2024).

[65] G. Tóth and I. Apellaniz, *Quantum metrology from a quantum information science perspective*, Journal of Physics A: Mathematical and Theoretical **47**, 424006 (2014), Publisher: IOP Publishing.

[66] J. Martin, Library of spin anticoherent states, 2025, http://www.oq.ulg.ac.be/libspinACstates.html[Accessed: 2/06/2025].

[67] S. M. Barnett and S. Croke, *Quantum state discrimination*, Advances in Optics and Photonics **1**, 238 (2009).

[68] O. E. Barndorff-Nielsen and R. D. Gill, *Fisher information in quantum statistics*, Journal of Physics A: Mathematical and General **33**, 4481 (2000).

[69] M. Hübner, *Explicit computation of the Bures distance for density matrices*, Physics Letters A **163**, 239 (1992).

Appendix A

Brief explanation of POVMs

Definition.
A *Positive Operator-Valued Measure (POVM)* is a generalization of projective (von Neumann) measurements in quantum mechanics. A POVM is defined by a set of positive semi-definite operators $\{M_\xi\}$ acting on a Hilbert space $\mathcal{H}$, satisfying the completeness relation

$$\sum_\xi M_\xi = \mathbb{1} \ . \tag{A.1}$$

Each operator M_ξ corresponds to a measurement outcome ξ, and the probability of obtaining outcome ξ when measuring a quantum state ρ is given by

$$p(\xi) = \mathrm{Tr}(M_\xi \rho) \ . \tag{A.2}$$

In contrast to projective measurements, the operators M_ξ in a POVM do *not* need to be orthogonal projectors or even mutually orthogonal.

Projective measurements are limited in their ability to optimally distinguish non-orthogonal quantum states. For instance, consider the task of distinguishing the following two non-orthogonal pure states of a qubit

$$|\psi_1\rangle = |0\rangle \, , \quad |\psi_2\rangle = \cos\theta \ |0\rangle + \sin\theta \ |1\rangle \quad \text{with } 0 < \theta < \frac{\pi}{2} \ . \tag{A.3}$$

Using only projective measurements (e.g., measuring in the computational basis), the best strategy does not minimize the error probability when identifying the state. However, by employing a *POVM with two or three elements*, one can perform *minimum-error state discrimination*, or even *unambiguous state discrimination* in some cases — tasks that are impossible with projective measurements alone. For instance, to optimally distinguish $|\psi_1\rangle$ and $|\psi_2\rangle$ with equal prior probabilities, the Helstrom measurement — a two-element POVM — achieves the minimum probability of error [67]. The POVM elements are constructed from the eigenvectors of $\rho_1 - \rho_2$, and do not correspond to projectors onto the original state vectors.

Appendix B

Saturation of the Quantum Cramér-Rao bound

Here we prove that Eq. (2.16) can be saturated. The proof is largely inspired by the work of Barndorff-Nielsen and Gill in [68]. First, let's do a spectral decomposition of the SLD, L_{ρ_θ}, in its own eigenbasis $\{|l_{\theta,i}\rangle\}$, thus we obtain

$$L_{\rho_\theta} = \sum_{i=1}^{l} \lambda_i \left|l_{\theta,i}\right\rangle \left\langle l_{\theta,i}\right| \ , \tag{B.1}$$

where, if the rank of ρ_θ is r, the rank of the SLD is l such that $r \leq l \leq d$, with d the dimension of the Hilbert space. Since the rank of ρ_θ is less or equal than the rank of the SLD, we can decompose the eigenvectors of ρ_θ in the eigenbasis of L_{ρ_θ}. We thus get

$$|\psi_i\rangle = \sum_{a=1}^{l} \psi_{i,a} \left|l_{\theta,a}\right\rangle \ , \tag{B.2}$$

where we used the closure relation and $\psi_{i,a} = \langle l_{\theta,a}|\psi_i\rangle$. With this relation, we write ρ_θ and $\rho_\theta^{1/2}$ in the new basis as

$$\rho_\theta = \sum_{i}^{r} \sum_{a,b}^{l} p_i \psi_{i,a} \psi_{i,b}^* \left|l_{\theta,a}\right\rangle \left\langle l_{\theta,b}\right| \ , \tag{B.3}$$

$$\rho_\theta^{1/2} = \sum_{i}^{r} \sum_{a,b}^{l} \sqrt{p_i} \psi_{i,a} \psi_{i,b}^* \left|l_{\theta,a}\right\rangle \left\langle l_{\theta,b}\right| \ . \tag{B.4}$$

From Eq. (2.10), we can impose the strict equality between these two terms. This is only possible if the imaginary part of the right terms vanishes. This condition can be expressed as

$$\sum_{i,j,k}^{l} \Im \left[L_{\theta,ij} \rho_{\theta,jk} M_{\xi,ki}\right] = 0 \quad \forall 1 \leq i,j \leq l \ . \tag{B.5}$$

The Eq. (2.13) can also be saturated if

$$M_\xi^{1/2} \rho_\theta^{1/2} = \alpha_\xi M_\xi^{1/2} L_{\rho_\theta} \rho_\theta^{1/2} \ , \tag{B.6}$$

with $\alpha_\xi \in \mathbb{C}$. The term $\sqrt{\mathrm{Tr}\left[\rho_\theta M_\xi\right]}$ can be absorbed in α_ξ. The condition (B.6) can be written as

$$\sum_k^l M_{\xi,ik}^{1/2} \rho_{\theta,kj}^{1/2} = \sum_{k,n}^l \alpha_\xi M_{\xi,ik}^{1/2} L_{\theta,kn} \rho_{\theta,nj}^{1/2} \quad \forall 1 \leq i,j \leq l \ . \tag{B.7}$$

Using the spectral decomposition of the SLD, Eq. (B.1), we obtain

$$\sum_k^l M_{\xi,ik}^{1/2} \rho_{\theta,kj}^{1/2} = \sum_k^l \alpha_\xi M_{\xi,ik}^{1/2} \lambda_k \rho_{\theta,kj}^{1/2} \ . \tag{B.8}$$

In order to fulfil the condition in Eq. (B.7), we could think that $\alpha_\xi = \lambda_k^{-1}$. However, it is not valid since α_ξ must be a constant depending only on ξ. The right solution to satisfy this condition is by incorporating $\delta_{\xi k}$ directly into the POVM element. We should take

$$M_{\xi,ij} = m_\xi^2 \delta_{\xi i} \delta_{\xi j} \ , \tag{B.9}$$

which brings Eq. (B.6) to

$$m_\xi \delta_{\xi i} \rho_{\theta,\xi j}^{1/2} = m_\xi \delta_{\xi i} \alpha_\xi \lambda_\xi \rho_{\theta,\xi j}^{1/2} \ . \tag{B.10}$$

It is clear that the previous equation is satisfied when $\alpha_\xi = 1/\lambda_\xi$. We must check whether this choice fulfills the other condition, Eq. (B.5). Let's insert the POVM into the trace

$$\begin{aligned} \mathrm{Tr}\left[L_{\rho_\theta} \rho_\theta M_\xi\right] &= \sum_{i,j,k}^l L_{\rho_\theta,ij} \rho_{\theta,ik} M_{\xi,ki} \\ &= \sum_{i,k}^l \lambda_i \rho_{\theta,ik} \delta_{\xi k} \delta_{\xi i} m_\xi^2 \\ &= \lambda_\xi \rho_{\theta,\xi\xi} m_\xi^2 \\ &= \lambda_\xi m_\xi^2 \sum_i^r p_i \left|\psi_{i,\xi}\right|^2 \ , \end{aligned} \tag{B.11}$$

which is a real number and, consequently, satisfies the condition. Thus, we have a sufficient condition on the POVM elements in order to saturate the CR bound, which can be written as

$$\{M_{\theta,\xi}\} = \left\{\left|l_{\theta,\xi}\right\rangle \left\langle l_{\theta,\xi}\right|\right\}_{1 \leq \xi \leq l} \ . \tag{B.12}$$

Therefore, there always exists a POVM saturating the inequality $I(\rho_\theta\,;\,\theta) \geq J(\mathrm{Tr}\left[\rho_\theta M_\xi\right]\,;\,\theta)$, which shows the validity of Theorem 2.1.

Appendix C

Closed form of the Bures metric

The derivation of the closed form of the Bures metric was done by M. Hübner in 1992 in [69]. The following proof is largely inspired by his work and the work of J. Fraisse in [24].

We consider a system whose state is represented by a density matrix ρ. The Bures metric is $D_B^2(\rho, \rho + \mathrm{d}\rho)$. For subsequent developments, we introduce the operator

$$A(t) = (\rho^{1/2}(\rho + t\mathrm{d}\rho)\rho^{1/2})^{1/2}.$$

Our aim is to evaluate $D_B^2(\rho, \rho + t\mathrm{d}\rho)$ up to second order in t. We have

$$D_B^2(\rho, \rho + t\mathrm{d}\rho) = 2 - 2\,\mathrm{Tr}\left[A(t)\right] \ . \tag{C.1}$$

The previous equation reduces to the Bures metric if $t = 1$ and is then equal to $2 - 2\,\mathrm{Tr}\left[A(1)\right]$. Let us make the following ansatz

$$D_B^2(\rho, \rho + t\mathrm{d}\rho) = t^2 g_{ij}(\rho)\mathrm{d}\rho^i \mathrm{d}\rho^j \ , \tag{C.2}$$

with ρ^i represent the coordinates on the manifold of density matrices. Taking the time derivative two times of Eq. (C.1) and Eq. (C.2), we get

$$g_{ij}(\rho)\mathrm{d}\rho^i \mathrm{d}\rho^j = -\frac{\mathrm{d}^2}{\mathrm{d}t^2}\,\mathrm{Tr}\left[A(t)\right] \ . \tag{C.3}$$

As the left-hand side is independent of time, we can put $t = 0$ in the last equation. In order to find an expression of the second derivative of $A(t)$, let us differentiate two times $A(t)^2$

$$\left.\frac{\mathrm{d}A(t)^2}{\mathrm{d}t}\right|_{t=0} = \dot{A}(0)A(0) + A(0)\dot{A}(0) = \rho^{1/2}\mathrm{d}\rho\rho^{1/2} \ , \tag{C.4}$$

$$\left.\frac{\mathrm{d}^2A(t)^2}{\mathrm{d}t^2}\right|_{t=0} = \ddot{A}(0)A(0) + A(0)\ddot{A}(0) + 2\dot{A}(0)\dot{A}(0) = 0 \ . \tag{C.5}$$

where for the first equality we used $A(t)^2 = \rho^2 + t\rho^{1/2}\mathrm{d}\rho\rho^{1/2}$. Here we will assume that ρ is invertible. If it is not the case, ρ has some zero eigenvalues and therefore is not diagonalisable. Thus we should restrain the analysis to the support of ρ. Then we can write

$$\ddot{A}(0) + A(0)\ddot{A}(0)A^{-1}(0) = -2\dot{A}(0)\dot{A}A^{-1}(0). \tag{C.6}$$

We can now take the trace and use a cyclic permutation to obtain

$$\mathrm{Tr}\left[\ddot{A}(0)\right] = -\,\mathrm{Tr}\left[\dot{A}(0)\dot{A}(0)A^{-1}(0)\right] \ . \tag{C.7}$$

We use the eigenbasis decomposition of $\rho = \sum_{i=1}^{r} p_i \left|\psi_i\right\rangle \left\langle\psi_i\right|$. We take the matrix elements of both sides of Eq. (C.5) and obtain for $\dot{A}(0)$

$$\dot{A}_{ij}(0) = \frac{\sqrt{p_i}\sqrt{p_j}}{(p_i + p_j)} \mathrm{d}\rho_{ij} \ , \tag{C.8}$$

with $\dot{A}_{ij}(0) = \langle\psi_i|\dot{A}(0)|\psi_j\rangle$ and $\mathrm{d}\rho_{ij} = \langle\psi_i|\mathrm{d}\rho|\psi_j\rangle$. Using Eq. (C.6) and Eq. (C.7), we find

$$g_{ij}\mathrm{d}\rho^i\mathrm{d}\rho^j = \mathrm{Tr}\left[\dot{A}(0)\dot{A}(0)A^{-1}\right] \tag{C.9}$$

$$= \sum_{i,j,k} (\rho^{-1})_{ij}\dot{A}_{jk}(0)\dot{A}_{ki}(0) \tag{C.10}$$

$$= \sum_{i,k} \frac{1}{p_i}\dot{A}_{ik}(0) \tag{C.11}$$

$$= \sum_{i,k} \frac{p_k}{(p_i + p_k)^2}|\mathrm{d}\rho_{ik}|^2 \ . \tag{C.12}$$

The last quantity can be expanded as

$$\sum_{i,k} \frac{p_k}{(p_i + p_k)^2}|\mathrm{d}\rho_{ik}|^2 = \sum_i \frac{1}{4p_i}|\mathrm{d}\rho_{ii}|^2 + \sum_{i\neq k} \frac{p_k}{(p_i + p_k)^2}|\mathrm{d}\rho_{ik}|^2 \tag{C.13}$$

$$= \sum_i \frac{1}{4p_i}|\mathrm{d}\rho_{ii}|^2 + \frac{1}{2}\left(\sum_{i\neq k} \frac{p_k}{(p_i + p_k)^2}|\mathrm{d}\rho_{ik}|^2 + \sum_{i\neq k} \frac{p_i}{(p_i + p_k)^2}|\mathrm{d}\rho_{ik}|^2\right) \tag{C.14}$$

$$= \frac{1}{2}\left(\sum_i \frac{1}{2p_i}|\mathrm{d}\rho_{ii}|^2 + \sum_{i\neq k} \frac{1}{p_i + p_k}|\mathrm{d}\rho_{ik}|^2\right) \tag{C.15}$$

$$= \frac{1}{2}\sum_{i,k} \frac{|\mathrm{d}\rho_{ik}|^2}{p_i + p_k}. \tag{C.16}$$

And finally, putting $t = 1$ in Eq. (C.2), we obtain

$$D_B^2(\rho, \rho + \mathrm{d}\rho) = \frac{1}{2}\sum_{i,k} \frac{|\mathrm{d}\rho_{ik}|^2}{p_i + p_k} \ . \tag{C.17}$$

Appendix D

Local generator $\mathscr{H}$

We consider the phase-shift Hamiltonian $H(\theta) = \theta G$ and its associated evolution operator $U_H = e^{-iH(\theta)}$, where G is the generator of the phase shift. This Hamiltonian commutes with its own derivative, $\partial_\theta H(\theta)$.

We restrict our analysis to pure initial states $|\psi_0\rangle$. The state after the unitary evolution is given by

$$|\psi_\theta\rangle = U_H |\psi_0\rangle \ . \tag{D.1}$$

To calculate the quantum Fisher information (QFI), we need to compute the derivative of the state

$$\partial_\theta |\psi_\theta\rangle = \partial_\theta U_H |\psi_0\rangle . \tag{D.2}$$

Assuming that the Hamiltonian $H(\theta)$ commutes with its derivative, i.e.,

$$[H(\theta), \partial_\theta H(\theta)] = 0, \tag{D.3}$$

we can express the derivative of the unitary evolution operator as $\partial_\theta U_H = -i(\partial_\theta H(\theta))U_H$.

Using this relation, the derivative of the state becomes

$$\partial_\theta |\psi_\theta\rangle = -i\partial_\theta H(\theta) |\psi_\theta\rangle \ . \tag{D.4}$$

Since the state is pure, we can use the expression for the QFI involving the derivative of the Hamiltonian, as given in Table 2.1 and obtain

$$I(|\psi_\theta\rangle ; \theta) = 4\mathrm{Var}\left[\partial_\theta H(\theta) |\psi_0\rangle\right] \ . \tag{D.5}$$

If the Hamiltonian is arbitrary, i.e., it does not commute with its derivative, we cannot use the same expression for the QFI. In this case, we define the Hermitian operator

$$\mathscr{H} = iU_H^\dagger \partial_\theta U_H \ , \tag{D.6}$$

which is referred to as the local generator. Giovannetti *et al.* proved that the QFI can then be written as [43]

$$I(|\psi_\theta\rangle ; \theta) = 4\mathrm{Var}\left[\mathscr{H}, |\psi_0\rangle\right] \ . \tag{D.7}$$